Doctoral Dissertation

Numerical Study on the Stability of Residual Stresses Induced by HFMI into a Welded Joint under Cyclic Loading

(高周波ピーニングで導入された圧縮残留応力の繰返し荷重下における安定性に関する数値解析）

Héctor Olmedo Ruíz Valdes

July 2019

Graduate School of Engineering,

Osaka University

Abstract

Many factors are known to influence the fatigue life of materials and welded structures, such as residual stress, material hardening/softening and surface roughness. The advantages of removing the potential threats of unwanted tensile residual stresses and exploiting the beneficial compressive residual stresses created by mechanical post-weld treatments are already known in welding communities.

Weld improvement methods have been investigated in many test programs and have in most cases been found to give substantial increases in fatigue strength. However, there are large variations in the actual improvements achieved, and the results obtained by various methods are not always ranked in a consistent manner. One explanation for the observed variations is the lack of standardization of the optimum method of application, but variations in the material, type of loading and type of test specimens may also have influenced the results. The effectiveness of the treatment also depends heavily on the skill of the operator.

A mechanical post-weld treatment such as HFMI has been found to exhibit a significant fatigue life enhancement of welded joints. The effectiveness of this mechanical impact treatment is mainly based on the combination of three effects: improvement of the local work hardening, introduction of compressive residual stress and closing of notches at the weld toe. However, there is a concern that the introduced compressive residual stress might deteriorate due to residual stress relaxation under cyclic loading, and the HFMI treatment might lose its

effectiveness. There is a need to develop a practical method to investigate the cyclic loading relaxation, as well as, several aspects of this treatment.

This study focuses on establishing a practical simulation method of welding, followed by HFMI. Then, the stability of residual stress under cyclic loading is investigated. Optimum HFMI simulation conditions are proposed and the validity of the computed results is demonstrated by comparison with experimental measurements available in the literature.

Acknowledgments

First, I wish to express my deepest appreciation and gratitude to my supervisor, Professor Naoki Osawa, for giving me the opportunity to join the laboratory of Ocean Material Engineering of the Department of Naval Architecture and Ocean Engineering of Osaka University, also for all the experience and knowledge he offered me during my research.

I would like to express my most sincere gratitude to Professor Hidekazu Murakawa, for giving to me the opportunity to come to Japan and accept me as research student at Joining and Welding Research Institute of Osaka University, also for his valuable comments and support during my studies and daily life in Japan.

I also want to express my gratitude to Professor Sherif Rashed, for his valuable comments, his patience, constructive discussions and his encouragement to keep working hard on this research, as well as checking all of my manuscripts, including this one.

I would like to express my sincere gratitude to Professor Ninshu Ma, Professor Masahiko Fujikubo and Professor Tsutsumi for participating as members of the dissertation committee and providing corrections and valuable suggestions to improve the quality of this work.

My gratitude also goes to the ISSC’18 Committee V.3 members for their contributions and valuable constructive discussions to improve the quality of this research.

I would also like to acknowledge the Panamanian Government for providing me with financial support that enabled me to study in Japan. Also to my supervisor at Technological University of Panama, Dr. Adan Vega Saenz who trusted in me and gave me useful advices while being in Japan.

Finally, and most importantly, I would like acknowledge the encouragement of my family and friends without whom this thesis would never have been completed.

Contents

Chapter 1 Introduction

1.1 Fatigue Failure of Welded Joints

Fatigue is a major cause of failure, particularly in welded structures, reflecting the inherently poor fatigue performance of many welded joint. [1-3]. Fatigue may be defined as the process of cycle accumulation of damage under fluctuating stresses and strains. An important feature is that the load is not large enough to cause immediate failure but instead failure occurs after the accumulated damage has reached a critical level. It has been estimated that fatigue contributes to approximately 90% of all mechanical service failures [4].

Fatigue is a problem that can affect any part or component that is subjected to fluctuating stress. Automobiles, airplanes, ships, nuclear reactors, among others are all subject to fatigue failures. Ship structures experience cyclic stress variations caused by seaway motions, wave loading, dynamic effects such as hull girder whipping, springing, machinery and hull vibration, and by changes in cargo distributions. These cyclic stresses can cause fatigue cracking in structural members and details of the ship structure if they are inadequately designed, constructed or maintained, see Fig. 1.1.

The fatigue strength of a structural component may be represented in terms of the S-N curve which plots the number of cycles to failure versus the cyclic stress range. The presence of a weld in a member can drastically reduce its fatigue strength as shown in Fig. 1.2 which compares the SN curves of welded connections with those of notched and un-notched steel plate. The arrows over some test points mean that the experimental predictions give slightly longer fatigue lives compared with the mean of the experiment data.

(a)

(b)

Fig. 1.1 Fatigue crack on a double hull tanker. **(a)** Fatigue crack in the side longitudinal. **(b)** Fatigue crack at the base of the strut. [5]

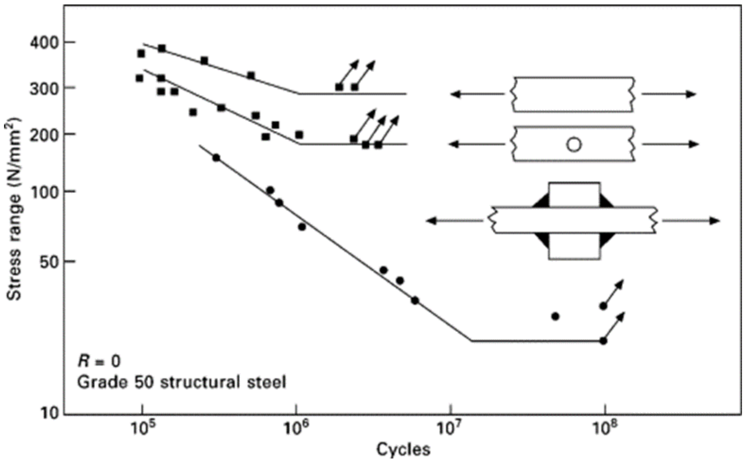

Fig. 1.2 Fatigue strengths of different plates. [6]

1.1.1 Effect of Weld Defects on Fatigue Strength

Welding process is one of the most popular assembly methods used by many industries such as ships and bridges. However, welding always produces many unavoidable problems such as deformation and residual stress especially for thin plate structures. The mechanism of production of stress and deformation and their influences upon the performance of welded structures are matters of keen concern for engineers. Thermal elastic-plastic analysis [7-10] by the finite element method (FEM) has become popular and has been applied to simulate the mechanical behavior of components during welding. According to results obtained from thermal elastic-plastic FE simulation and measurements done in experiments, it has been concluded in [11, 12] that inherent strain ε^* is responsible for the welding distortion and residual stress of welded structures. Many factors influence the magnitude of inherent strain such as heat input, material properties, type of welded joint, dimensions of joint components, etc. The total strain ε produced during welding or line heating process can be decomposed into five components as shown in Eq. 1.1

$$\varepsilon = \varepsilon^T + \varepsilon^p + \varepsilon^c + \varepsilon^t + \varepsilon^e \tag{1.1}$$

Where, ε^T is the thermal strain, ε^p is the plastic strain, ε^c is the creep strain, ε^t is the phase transformation strain and ε^e is the elastic strain.

Noting that Eq. 1.1 can be reorganized into Eq. 1.2. This equation symbolically means that distortion and residual stress are produced by the inherent strain ε^* which consists of thermal, plastic, creep strains and the phase transformation strain.

$$\varepsilon^* = \varepsilon - \varepsilon^e = \varepsilon^T + \varepsilon^p + \varepsilon^c + \varepsilon^t \tag{1.2}$$

Figure 1.3 shows the basic patterns of welding deformation. They can be separated into the longitudinal shrinkage, transverse shrinkage, transverse bending and longitudinal bending. Fig. 1.4 shows the typical patterns of residual stress distributions in a butt-welded joint. The maximum magnitude of longitudinal tensile stress is approximately equal to the yield stress. Unless the combination of base and filler metals and the welding condition are chosen properly, weld cracks which appear at the weld toe may deteriorate the strength of the welded structure and lower its reliability, by inducing brittle fracture, fatigue, buckling, and stress corrosion [13].

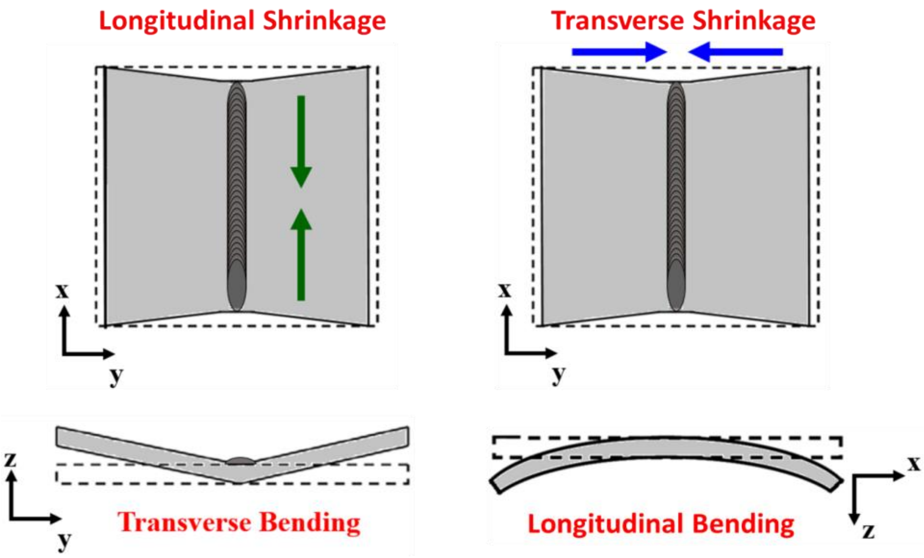

Fig. 1.3 Four components of welding distortion. [14]

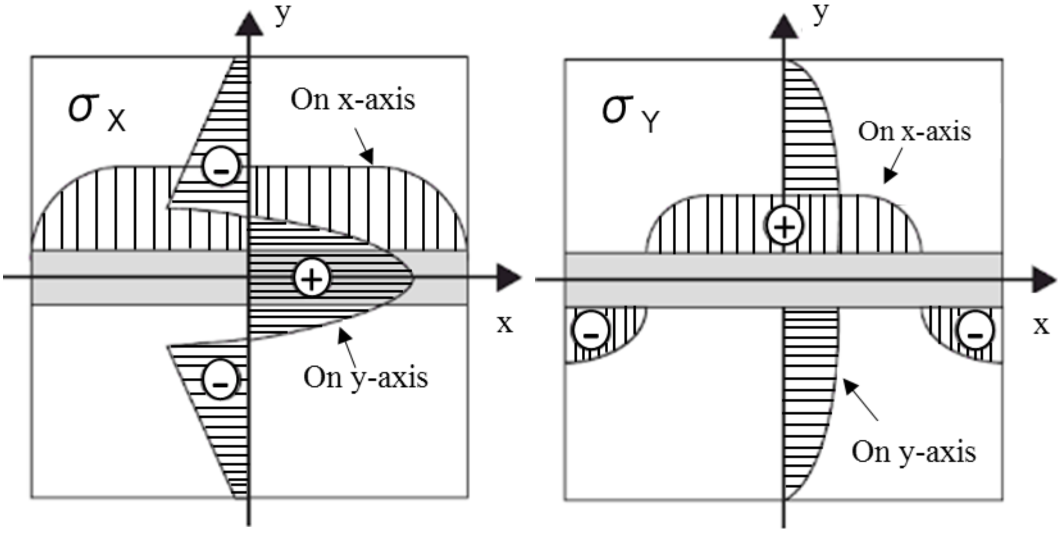

(a) Longitudinal stresses (S_{XX}) **(b)** Transverse stresses (S_{YY})

Fig. 1.4 Typical distribution patterns of welding residual stresses in a butt-welded joint. [13]

1.2 Overview of Fatigue Strength Improvement

Weld improvement methods have been investigated in many test programs and have in most cases been found to give substantial increases in fatigue strength. However, there are large variations in the actual improvements achieved, and the results obtained by various methods are not always ranked in a consistent manner. One explanation for the observed variations is the lack of standardization of the optimum method of application of fatigue improvement methods. Variations in the material, type of loading and type of test specimens may also have influenced the results. The effectiveness of the method also depends heavily on the skill of the operator.

In general, the weld fatigue improvement methods may be divided into two groups; residual stress methods and weld geometry improvement methods. Some benefits of residual stress methods are introduction of high local compressive residual stress, improvement of material work hardening, surface quality is improved, closing of notches at the weld toe. Geometry modification methods have been found to exhibit a significant fatigue life enhancement by improving the surface quality, reduction of local stress peaks, etc.

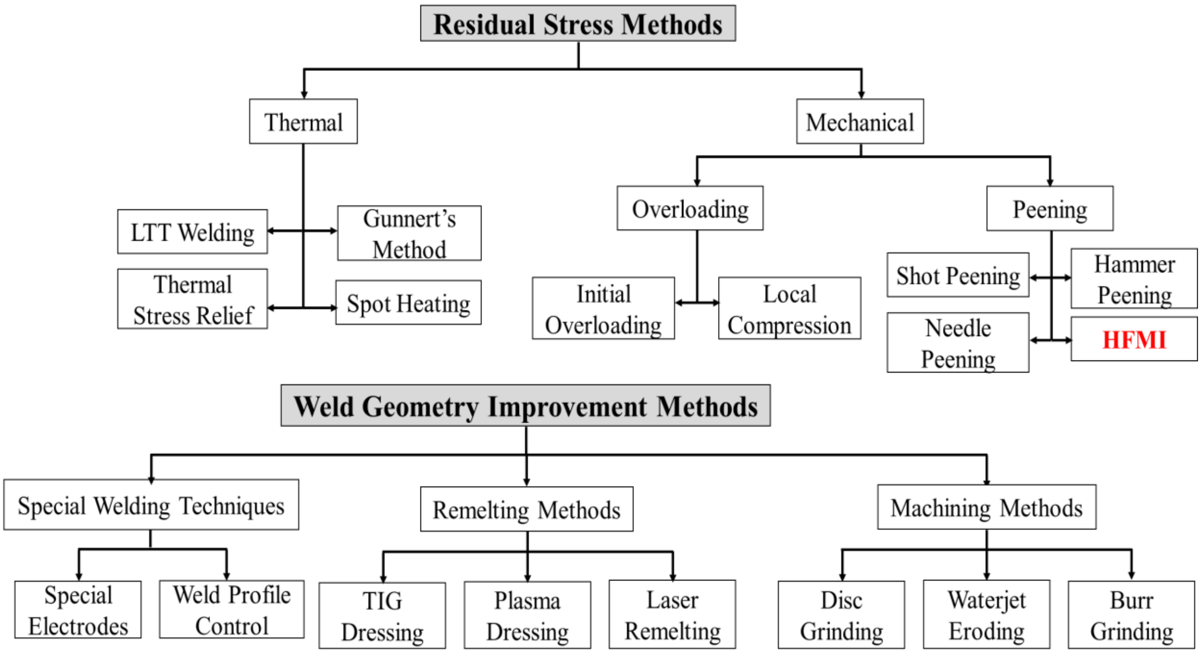

Fig. 1.5 Classification of some weld improvement methods.

This research is focused on the residuals stress methods especially on the post-weld peening method referred to as high-frequency mechanical impact (HFMI) which has demonstrated a significant fatigue life enhancement of welded joints. Fig. 1.5 shows a diagram of some weld improvement methods.

1.3 High-Frequency Mechanical Impact

The advantage of removing potential threats of unwanted tensile residual stresses and exploiting the beneficial compressive stresses by mechanical treatments are already know in the welding communities. The innovation of locally modifying the residual stress state in welded components by the use of an ultrasonic hammering technology is widely attributed to Statnikov [15].

Since 2002, 46th IIW Commission XIII on Fatigue of Welded Components and Structures has published documents reporting on High Frequency Mechanical Impact (HFMI) technology development and experimental studies involving HFMI. In 2007 IIW Commission XIII approved a best practice guideline of post weld treatment methods for steel and aluminum structures [16]. This guideline covers four commonly applied post weld treatment methods: burr grinding, TIG re-melting (or TIG dressing), hammer peening and needle peening, see Fig. 1.6. Hammer peening and needle peening were classified as residual stress modification methods which reduces high tensile residual stress at the weld toe and induce compressive residual stresses in its places, increasing the fatigue life of welded joints, [17-21]. The effectiveness of mechanical impact treatment is primarily based on the combination of three effects: improvement of the local work hardening, introduction of compressive residual stress and closing of notches at the weld toe, increasing the fatigue life of welded joints [18-41].

(a) Needle peening gun **(b)** Pneumatic impact treatment gun (PIT)

Fig. 1.6 Typical peening guns.

Finally, in 2010 IIW Commission XIII coined the term High Frequency Mechanical Impact (HFMI) as a generic term to describe several related technologies for improving the fatigue strength of welded structures by locally modifying the residual stress using ultrasonic, pneumatic or other impact technologies. HFMI makes use of cylindrical indenters which impact a component or structure with high frequency (> about 90 Hz). Hence, compressive residual stresses are induced by mechanical plastic deformation of the weld toe region. Residual stresses arise as a result of the constraint imposed by the surrounding elastic material. Fig. 1.7 shows a typical weld toe before and after post-weld treatment.

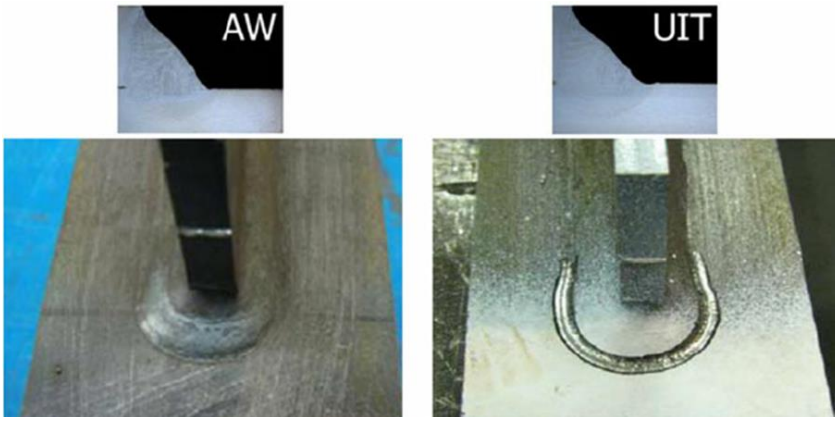

Fig. 1.7 Comparison of weld and after HFMI. [42]

An important practical limitation on the use of improvement techniques that rely on the presence of compressive residual stresses is that their fatigue life is strongly dependent on the applied mean stress. In particular, the benefit decreases as the maximum applied stress approaches the yield stress, disappearing altogether at stresses above yield. Thus, in general, the techniques are not suitable for structures operating at applied stress ratios (min. stress/ max. stress) of more than 0.5 or maximum applied stresses above around 80% yield. Another limitation is the types of joints suitable for improvement, see Fig. 1.8.

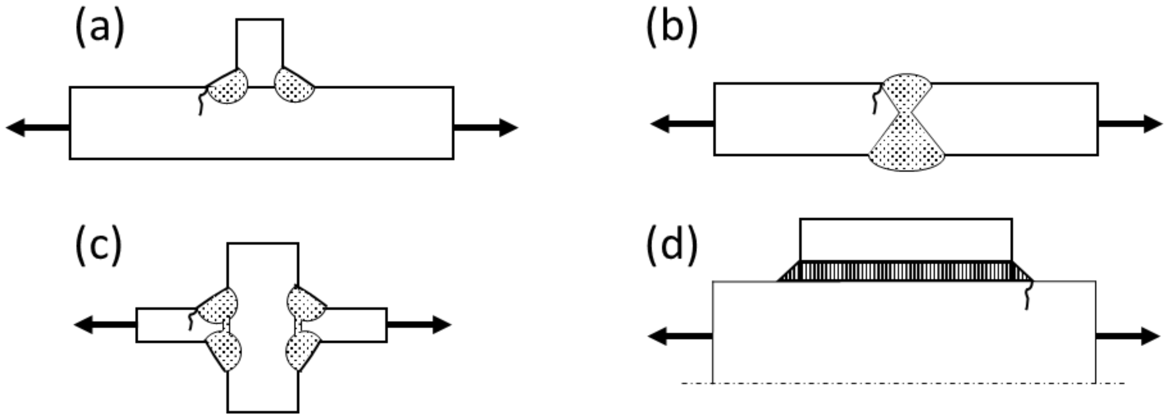

Fig. 1.8 Examples of joints suitable for improvement.

1.4 Review of Literature on HFMI

HFMI has shown significant fatigue life enhancement of welded joints. However, several aspects of this treatment as well as compressive residual stress relaxation under cyclic loading need to be clarified or further investigated. This is the main reason why fatigue strength improvement by means of HFMI has been an active topic of research during the last 20 years. In this section a review of some studies done on HFMI will be covered.

1.4.1 Mechanism of fatigue strength enhancement by HFMI

To understand the mechanism of fatigue strength enhancement by HFMI, it is absolutely necessary that numerical analysis accurately describes the induced residual stress field. Therefore, numerical simulation of HFMI-process has recently been investigated [43-55].

Many researchers have examined the influence of different analysis parameters (e.g., Finite Element (FE) mesh size, boundary conditions, damping, etc.). Also, various HFMI parameters (e.g., friction coefficient, tool indentations, pitch, etc.) on residual stress distribution. Explicit elastic-plastic finite element

(EPFE) codes (e.g., Abaqus Explicit) were utilized in order to take dynamic effects into account. [34,42-48, 52, 56, 57]. Stoschka [57] concluded that HFMI can be considered sufficient if a minimum indentation depth of about 0.1 mm is achieved. However, other parameters have not been completely quantified.

Material behavior is another important issue in HFMI simulation. Effects of HFMI treatment have been investigated on base materials plates [43, 46-48, 51, 52] or welded joints [44-46, 53, 54]. S355 steel grades or similar has been investigated by [43, 44, 46, 48, 49] assuming isotropic [43, 46, 52], kinematic [44] or combined isotropic-kinematic [43, 46, 48, 49, 52] hardening law. Combined isotropic-kinematic hardening laws from [43, 48, 49, 52] are based on Chaboche [58] or Johnson-Cook [59] models.

Foehrenbach [48] carried out numerical and experimental study to describe the condition in the surface layer under HFMI on a stress-free S355 steel plate. They revealed that material hardening model has a large influence on the simulated residual stresses, and that the simulation with combined isotropic-kinematic strain rate dependent hardening behavior can reproduce the behavior.

Based on [48], Ernould [56] found that no significant difference could be observed when secondary impacts are considered. Furthermore, Ernould obtained a better agreement over the complete residual stress profile in the depth (plate thickness direction) with the modified Chaboche model [58].

HFMI can be simulated in two different ways. Displacement controlled simulation and force-controlled simulation. [10, 11] demonstrated that displacement-controlled simulation can recreate the phenomenon and gives accurate results.

1.4.2 Stability of induced compressive stresses

A major concern regarding the relaxation of the residual stress induced by HFMI techniques have become an important topic in welding community. Measurements by Tai [60] indicate that the compressive residual stress is reduced just after the first load-cycle. This has been confirmed by Miyashita [61] on laser peening treatment.

These findings are of special interest in case of variable amplitude loading, which commonly occurs in real life applications. Yildirim [62] used high strength steel longitudinal stiffeners in as-welded and HFMI treated conditions under constant and variable amplitude loading to exhibit that the increase factor by the post-treatment is reduced in case of the variable load scenario.

A study on fatigue strength improvement for ship structures by ultrasonic peening by Hara [63] showed considerable residual stress relaxation due to peak loads. This is confirmed by measurements in Okawa [64] showing that the compressive residual stress at the hot spot in HFMI-treated joints decrease by about 45%.

A finite element study in [65] concluded that the benefit from compressive residual stresses decreased with increasing stress range, stress ratio (min. stress/max. stress) and peak load magnitude. However, this study is based on a simplified procedure considering the residual stress state by mapping an experimental residual stress field in the numerical model.

Leitner [66] carried out an experiment on a S355 out of plane gusset joint and compared with numerical simulation procedure incorporating welding, HFMI and cyclic loading and showed the residual stress relaxation in low and high-cyclic fatigue regions.

1.5 Problem Statement

Despite the fact that during the last 20 years valuable investigations of fatigue strength improvement of welded joints by HFMI have been presented and many studies on the relaxation of compressive stresses produced by HFMI under cyclic loadings, the state of the art of fatigue strength improvement by HFMI is still far from being satisfactory. The main reason is that the mechanism of fatigue strength improvement by HFMI is highly complex and does not easily submit to analyze with simple analytical models. This difficulty comes from material and geometrical changes during the treatment, and the complex local stress field produced by HFMI.

Several studies have been carried out to understand the mechanics of fatigue strength enhancement by HFMI. Some of these studies focused on the influence of the mesh sizes, choice of friction model, indentation depth, boundary conditions and material hardening models on the numerical simulation. However, no practical methods have been developed yet.

Furthermore, concerns about residual stress relaxation induced by HFMI has become an important topic on welding community. In recent years, important findings about the effect of the applied maximum nominal stress on treated joints, contribution of constant and variable cyclic loadings, effect of peak loads on compressive residual stresses has been reported. However, recommendations on cyclic loading conditions did not consider such variable amplitude loading and cyclic loading with peak loads. Furthermore, only a few studies by means of FE simulation have been carried out considering the residual stress state induced in welding, followed by HFMI and cyclic loading.

This research can be divided into two main objectives besides helping to expand the existing knowledge on HFMI. First, is to propose optimum HFMI simulation conditions. Second, following the optimum simulation conditions, a practical numerical simulation method is proposed to evaluate compressive residual stress development during welding followed by HFMI, and then relaxation of this stress under cyclic loading.

1.6 Framework of Thesis

This thesis is divided into seven chapters. The background of HFMI as well as the main objectives of this thesis have already been presented in this chapter.

A description of the tools and theories are presented in chapter 2. First, welding simulation by thermal elastic plastic FEM is outlined. Then, an introduction of the dynamic simulation and the explicit commercial code used in this study to perform the HFMI and cyclic loading simulation are presented. Finally, the material hardening model used during HFMI and cyclic loading is presented.

Review of experimental and numerical studies which are used as target through this study are presented in chapter 3. First, numerical and experimental studies on flat stress-free plates to investigate the effect of HFMI in the surface layer is presented. Next, a study on the stability of residual stresses induced in welding followed by HFMI under cyclic loading on an out-of-plane gusset welded joint is shown.

In chapter 4, numerical simulations of HFMI on a flat stress-free plate are carried out. This chapter can be divided into three parts. First, recommendation on FE meshing is proposed. Second, using the recommended FE mesh size, comparison with experimental measurements and numerical data presented in chapter 3 is carried out. Third, in order to propose optimum HFMI simulation conditions, the influence of HFMI conditions such as impact pitch, HFMI indentation depth, yield stress, etc., are analyzed.

In chapter 5, the proposed optimum HFMI simulation conditions are used to carry out HFMI simulation on an out-of-plane gusset welded joint. A practical simulation of welding, followed by HFMI is examined. The target is the same gusset welded joint presented in chapter 3. The first half of this chapter studies the welding simulation by means of thermal-elastic-plastic FE code JWRIAN. The second half considers HFMI simulation by means of dynamic simulation using the explicit commercial code MSC.Dytran. To demonstrate the reliability of the computed results. The computed residual stresses by welding and HFMI are compared with results obtained by Pusan National University (PNU) performing the same simulation using another explicit commercial code

(Abaqus), and with the trend by experimental measurements from the literature shown in chapter 3.

In chapter 6, the stability of the compressive stress field induced by HFMI under cyclic loading is investigated. First, a study of the effect of frequency on cyclic loading response is considered. Then, effect of cyclic loading under constant amplitude loadings and cyclic loadings with a peak load followed by constant amplitude loading is analyzed.

An overall summary of the thesis is given in chapter 7. Conclusions drawn from the computational study are stated, and recommendations for futures studies regarding the fatigue strength improvement by HFMI are presented.

Chapter 2 Methods of Analysis

2.1 Introduction

Numerical simulations have proven to be an effective tool in the research of fatigue strength improvement. In order to avoid costly and time-consuming experiments, numerical simulation is utilized in this research.

A description of the software, material conditions and theories employed in this study are presented in this chapter. At first, an explanation of thermal elastic plastic finite element analysis (FEA) code which is used to accurately simulate welding processes, is given. Then, an explanation of dynamic analysis and the commercial code used to investigate the mechanical behavior of welded joints subjected to HFMI, followed by cyclic loading. Finally, the implemented material hardening model during HFMI and cyclic loading simulation is introduced.

2.2 Thermal Elastic Plastic Analysis

In this research the thermal-mechanical behavior of a welded gusset joint is investigated using uncoupled thermal/mechanical formulation proposed by UEDA and Yamakawa [67]. This uncoupled formulation considers the contribution of the transient temperature field to strains and stresses developed through thermal expansion, and temperature-dependent physical and mechanical properties.

The solution procedure consists of two stages. First, transient temperature distribution history is computed using FE heat transfer simulation. Then, the transient temperature distribution obtained from the heat transfer simulation is employed as a thermal load in the subsequent thermal elastic plastic analysis. Displacements, stresses and strains are computed. These algorithms are well verified against test results [68, 69], and are all integrated in the in-house code JWRIAN (Joining and Welding Research Institute Analysis) program. The basic procedure followed in the simulation is outlined in the schematic diagram shown in Fig. 2.1.

JWRIAN is developed by The Joining and Welding Research Institute (JWRI) of Osaka University. In JWRIAN, the Iterative Substructure Method (ISM) developed by Murakawa [70] is used to perform ultra-high speed implicit thermal elastic plastic finite element (TEPFE) analysis.

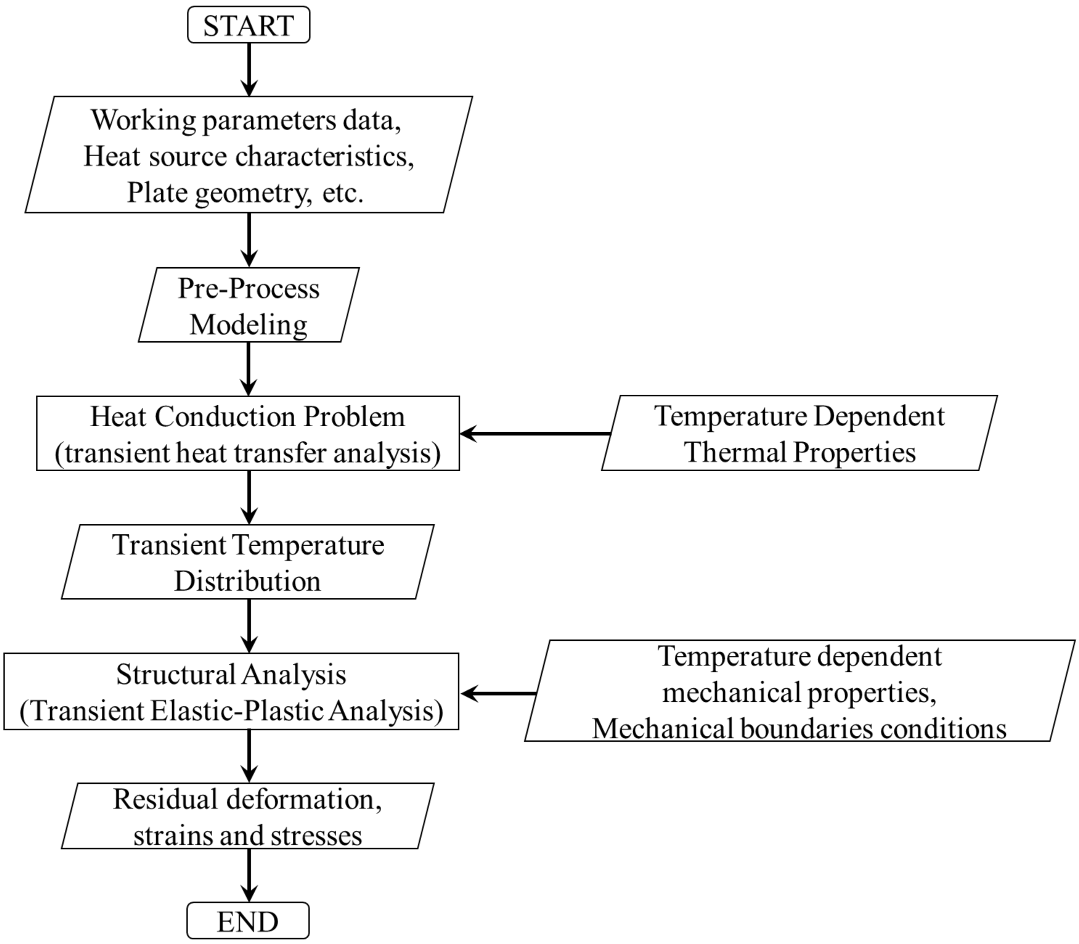

Fig. 2.1 Schematic diagram of Thermal Elastic-Plastic analysis.

2.3 Dynamic Analysis

In this study, dynamic analysis is utilized to model the HFMI process on a flat plate, and on an out-of-plane gusset welded joint to investigate the HFMI response. Furthermore, dynamic analysis is used to investigate the stability of the compressive stresses introduced by HFMI when cyclic loading is applied on the out-of-plane gusset welded joint.

HFMI process and cyclic loading are analyzed using the commercial code MSC.Dytran [71]. Dytran is an explicit finite element analysis code intended for simulating fast dynamic events such as impact and crash, and to analyze the complex nonlinear behavior that structures undergo during these events.

Explicit dynamic analysis is suitable for large models exhibiting complex highly non-linear behavior lasting for a short time. In the Explicit method, the equation of motion, is transformed as shown in Eqn 2.1.

$$MX'' + CX' + KX = F_{EX}$$

$$MX'' = F_{EX} - F_{INT} \tag{2.1}$$

And $$F_{INT} = CX' + KX$$

Where, M is a mass matrix, C is the damping coefficient matrix, K is stiffness matrix, F_{EX} and F_{INT} are the external and internal force matrix respectively, X'' is the acceleration matrix, X' is velocity matrix, and X is the displacement matrix.

Lumped mass is used to render the mass matrix M into a diagonal matrix. Now the current acceleration of each lumped mass (nodal point) can be individually calculated without the need for a matrix solution. However, for numerical stability, time increment should be kept smaller than the smallest h/c of each element, where h is the element characteristic length (in 3-D elements, element volume divided by the area of the biggest face) and c is the speed of sound in the element material.

A schematic diagram of the explicit method is shown in Fig. 2.2.

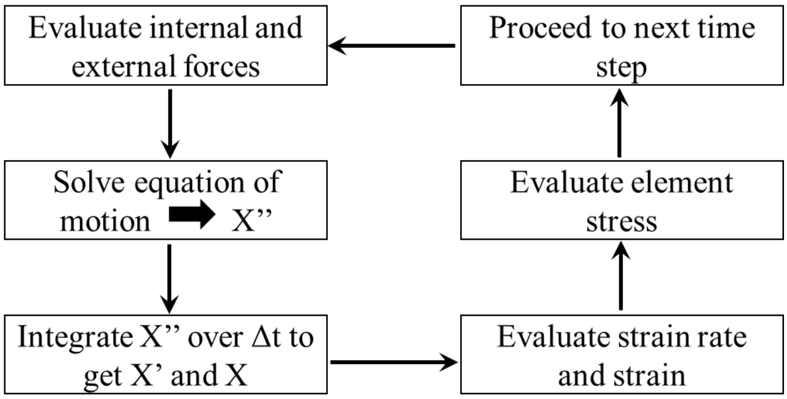

Fig. 2.2 Schematic diagram of the explicit method.

2.4 Material Hardening

To evaluate the residual stress after HFMI and cyclic loading, it is thought that a yield model that correctly represents material behavior, including material hardening is indispensable.

Yield Condition

A yield condition that accounts for mixed hardening and strain rate effect may be expressed by Eqs (2.2). The model is an extension of Chaboche’s kinematic hardening model [58].

$$J_2\,(\sigma - \alpha) = J_2\,(s - \alpha') = \sigma_o f\,(\dot{\varepsilon}_p)\,g\,(\varepsilon_p) \tag{2.2}$$

That is

$$J_2\ (\mathbf{s} - \boldsymbol{\alpha}') = \sqrt{\frac{3}{2}(\mathbf{s} - \boldsymbol{\alpha}'):(\mathbf{s} - \boldsymbol{\alpha}')} = \boldsymbol{\sigma}_y \tag{2.3}$$

Where,

J_2 is the stress second invariant

$\boldsymbol{\sigma}$ is the acting stress tensor

$\boldsymbol{\alpha}$ is the back stress tensor as given in 2 below

$\boldsymbol{s}$ is the acting deviatoric stress tensor

$\boldsymbol{\alpha'}$ is the deviatoric back stress tensor

σ_o is the yield stress (scaler)

$$\sigma_y = \sigma_o\, f\,(\dot{\varepsilon}_p)\; g\,(\varepsilon_p) \tag{2.4}$$

$f\,(\dot{\varepsilon}_p)$ is a function of the plastic strain rate

$g\,(\varepsilon_p)$ is a function of the plastic strain

Functions f and g may take any convenient analytical or numerical (tabular) form that is suitable to the material at hand. In this work, Cowper-Symonds strain rate hardening rule is adopted for the function f.

$$f\ (\dot{\varepsilon}_p) = 1 + (\dot{\varepsilon}_p / H)^{1/p} \tag{2.5}$$

Where H and p are Cowper-Symonds strain rate hardening parameters. The isotropic hardening part of Jonson-Cook Yield function is adopted for the function g.

$$g\ (\varepsilon_p) = 1 + a(\varepsilon_p)^b \tag{2.6}$$

Where a and b are isotropic strain hardening parameters.

Kinematic hardening is included in Eqns (2.2) and (2.3) through the back stress tensor $\boldsymbol{\alpha}$ or its deviatoric tensor $\boldsymbol{\alpha}$'. Isotropic hardening and strain rate effect are included in the yield stress σ_y in Eqn (2.4).

Back Stress Tensor

The back stress tensor $\boldsymbol{\alpha}$ in Eqn (2.1) may be expressed as follows

$$\alpha = \Sigma \alpha_k \qquad \text{k=1,m} \tag{2.7}$$

This summation allows a better evaluation of $\boldsymbol{\alpha}$ such that the predicted kinematic hardening accurately matches the actual material kinematic hardening.

In the plastic range, at any step n of the simulation, the deformation increment from step n-1 to step n causes an increment of the effective plastic strain $\Delta\varepsilon_p$ (scaler), which in turn causes increments $\Delta\boldsymbol{\alpha}_k$ of the back stress tensor components $\boldsymbol{\alpha}_k$

$$\boldsymbol{\alpha}_{kn} = \boldsymbol{\alpha}_{kn-1} + \Delta\boldsymbol{\alpha}_k \tag{2.8}$$

$$\Delta\boldsymbol{\alpha}_k = C_k \Delta\varepsilon_p \frac{1}{\sigma_y}(\boldsymbol{\sigma} - \boldsymbol{\alpha}) - \gamma_k \boldsymbol{\alpha}_k \Delta\varepsilon_p \tag{2.9}$$

Where C_k and γ_k are kinematic hardening parameters, and, σ_y, $\boldsymbol{\sigma}$, $\boldsymbol{\alpha}$ and $\boldsymbol{\alpha}_k$ are those at step $n-1$.

Options to evaluate $\Delta\,\boldsymbol{\alpha}_k$ of Eqn (2.9)

Three options are available for σ_y and $\boldsymbol{\sigma}$ in these equations as follows.

1) Include the isotropic hardening and strain rate effect in both σ_y and $\boldsymbol{\sigma}$.

$$\boldsymbol{\sigma} = \boldsymbol{s}_{n-1} + p_{n-1} \tag{2.10}$$

Where, p_{n-1} is the average normal stress (hydrostatic pressure) at step $n-1$.

$$\sigma_y = \sigma_o \left[1 + a\,(\varepsilon_{pn-1})^{b}\right]\left[1 + (\dot{\varepsilon}_{pn-1}/D)^{1/p}\right] \tag{2.11}$$

2) Include the isotropic hardening only in both σ_y and $\boldsymbol{\sigma}$

$$\boldsymbol{\sigma} = (\boldsymbol{s}_{n-1} + p_{n-1}) \,/\, \left[1 + (\dot{\varepsilon}_{pn-1}/D)^{1/p}\right] \tag{2.12}$$

$$\sigma_y = \sigma_o \left[1 + a\,(\varepsilon_{pn-1})^{b}\right] \tag{2.13}$$

3) Use the base static values of both σ_y and $\boldsymbol{\sigma}$

$$\boldsymbol{\sigma} = \left[(\boldsymbol{s}_{n-1} + p_{n-1}) \,/\, (1 + a\varepsilon_{pn-1}^{\;b})\right] / \left[1 + (\dot{\varepsilon}_{pn-1}/D)^{1/p}\right] \tag{2.14}$$

$$\sigma_y = \sigma_o \tag{2.15}$$

This material yield model is incorporated in the used code, MSC-Dytran, by a user subroutine. Numerical calculations with a single hexahedron element has shown that the three options give very close results. However, selection should be based on matching the numerical results with actual behavior of the material at hand. Fig. 2.3 (a) shows the computed stress/strain behavior with MSC-Dytran using option (3), similar stress-strain relationship as the experimental one presented by Foehrenbach et al. [49] is observed.

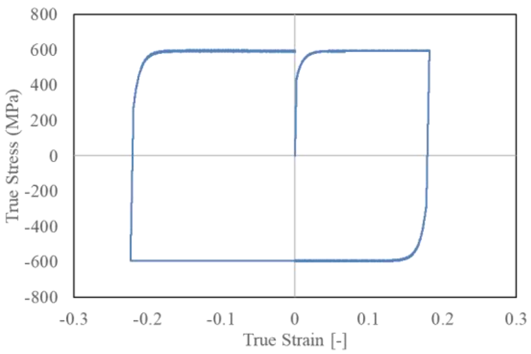

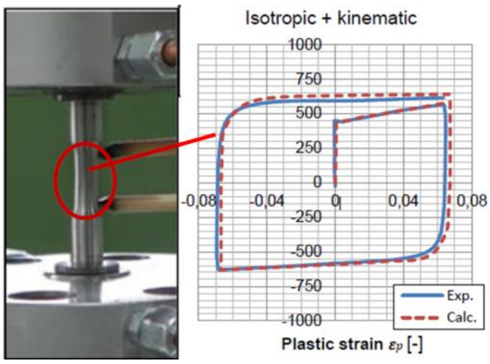

(a) **(b)**

Fig. 2.3 Stress-strain response of the hardening model. **(a)** numerical result with Dytran. **(b)** experiment and calculation S355J2H (Foehrenbach et al. [49]).

Chapter 3 Review of Experimental Studies

3.1 Introduction

This chapter presents a review of experimental and numerical studies carried out by Foehrenbach et al. [48], Ernould et al. [56] and Letiner et al. [66], and used as a reference in this research. First, a review of a study of the effect of HFMI on a flat stress-free plate is presented. In that study, Foehrenbach et al. [48] compared measurement results with the computed ones, considering the effect of different material models and HFMI simulations methods. Ernould et al. [56] reused the FE model developed in [48] and carried out the numerical simulation using different assumptions. Improved agreement with the measurements in [48] was obtained.

Finally, an experimental study on the stability of compressive residual stress induced by HFMI is presented, Leitner et al. [66]. However, only welding and HFMI treatment are taken into account for this research.

3.2 Review of HFMI on a flat stress-free plate

3.2.1 Determination of simulation parameters

The objective in Foehrenbach et al. [48] was to develop a computationally efficient approach for predicting residual stresses induced by the HFMI process on steel specimens. First, an investigation of simulation parameters such as HFMI indentation depth, frequency, material hardening behavior was conducted. For the determination of the impact velocity during HFMI, a high-speed-camera with a frame rate of 3000 fps was used. Via measurement of the picture size before the shot the scale of the picture could be determined. An initial picture of the untreated surface acts as reference for the subsequent transient indentation position measurements. The measurement of the contact force during HFMI was performed with strain gauges that have been glued on the pin tool, see Fig. 3.1. The evaluated impact forces are similar to previous results reported in [46]. Only the maximum forces of the primary impacts (Fc) were used for the subsequent simulation of the contact force. Impact angle for all measurement was 90°. The specimen is made out of a 10-mm thick sheet metal with the material grade S355J2H. The highest impact forces are obtained at an operating frequency of about 90 Hz for this hammering device and treated steel grade. According to the high speed camera and strain gauge measurements, the time of contact between pin and specimen is around 0.3 ms and seems relatively stable. Regarding this, the strain rate in the process could be estimated as 200 1/s to 400 1/s.

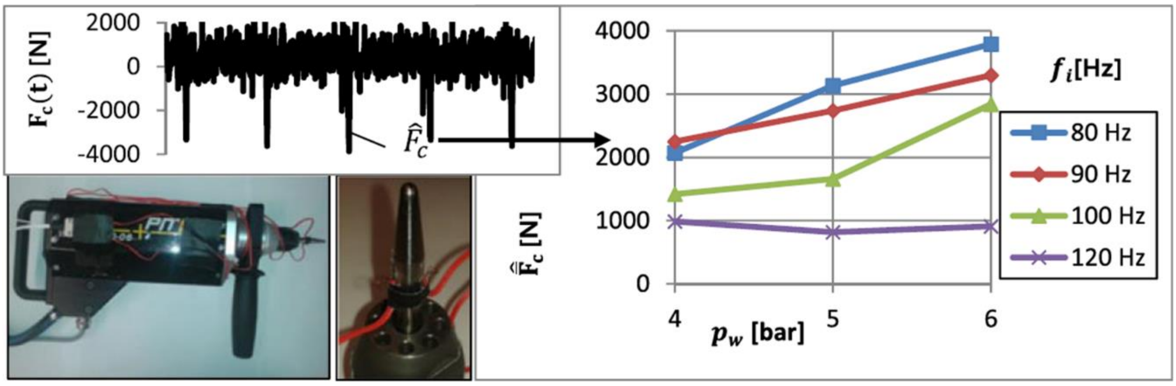

Fig. 3.1 Pneumatic impact treatment device [48,72].

For the measurement of the indentation depth u, the surface of the specimen shown in Fig. 3.2 has been scanned with a 3D Laser scanner. Similar techniques and surface preparations as described in Refs. [73, 74] were used. Specimens were treated with the feed rate of 12 cm/min, which is recommended by the device manufacturer and other with the feed rate of 24 cm/min. Each specimen was treated on three predefined paths, see Fig. 3.2. The first path was treated one time, the second path two times and the third path was treated three times using the same HFMI tool. Table 3.1 shows the measured indentation depth by a laser scanner and averaged at five positions for each path.

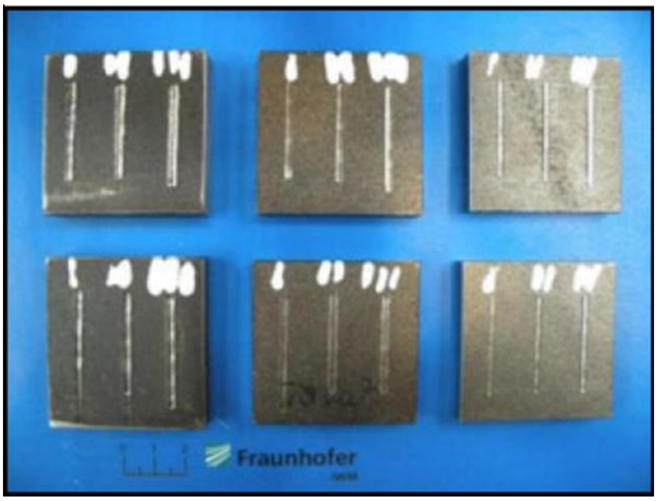

Fig. 3.2 Treated specimens “treated paths” [48].

Table 3.1 Measured indentation depths of treated paths for S355J2H [48]

Speed (cm/min)	12	24
1 path	0.173 mm	0.143 mm
2 paths	0.196 mm	0.193 mm
3 paths	0.241 mm	0.223 mm

Due to high plastic deformation of the surface layer during the process, the authors decided to implement a material model that correctly represents the material behavior. Therefore, the combined isotropic kinematic hardening model “Chaboche-model” was considered [75 - 79].

The calibration of the combined material model in Abaqus [80] was compared with the test data by a single-element calculation under uniaxial load. The number of kinematic hardening components was default and achieves a good match result shown in Fig. 3.3 (a). Fig. 3 (b) shows the extension of the isotropic part of the material hardening model considering the strain rate dependency using the literature data of HSLA 590 steel provided from the American Iron and Steel Institute [81] used for crash simulations in the automobile industry. The steel HSLA 590 has similar mechanical properties and chemical composition as S355J2H, see Table 3.2. Where E is the Young Modulus, ν is the Poisson's Ratio, σ_o is the yield stress, C_1, C_2, γ_1 and γ_2 are parameters of the back stress tensors.

Table 3.2 Material parameter in Abaqus for 355J2H (kinematic hardening) [80]

E [GPa]	ν	σ_o [MPa]	C_1 [MPa]	γ_1	C_2 [MPa]	γ_2
210	0.3	435	8971.8	218.65	12654.88	106.98

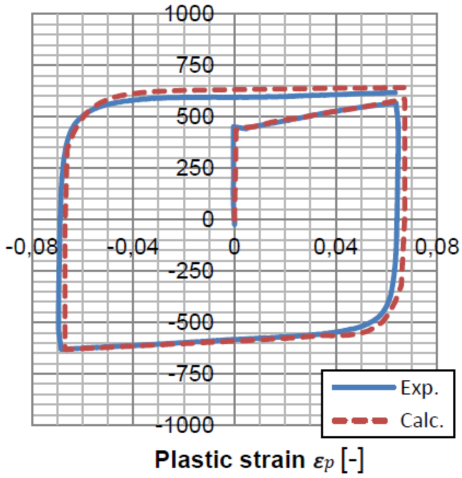

Fig. 3.3 Uniaxial one-element calculation for the calibration of hardening model in Abaqus. [49]

3.2.2 Measurement of experimental results

For the validation of the calculated residual stress fields, extensive non-destructive experiments by means of X-ray diffraction method were performed at an indentation of 5µm at Fraunhofer IWM Freiburg, as shown in Fig. 3.4 (a) and by neutron diffraction method, Fig. 3.4 (b), performed at the Forschungs-Neutronenquelle Heinz Maier-Leibnitz (FRM II). Residual stress measurements at the surface and at a depth of 0.7 mm to 4 mm were carried out. The volume of the gauge of 1 mm × 1 mm × 1 mm for longitudinal stress and 1 mm × 0.5 mm × 1 mm for transverse and through-thickness stress were used and this was kept as far away as possible from the surface in case of potential surface effects.

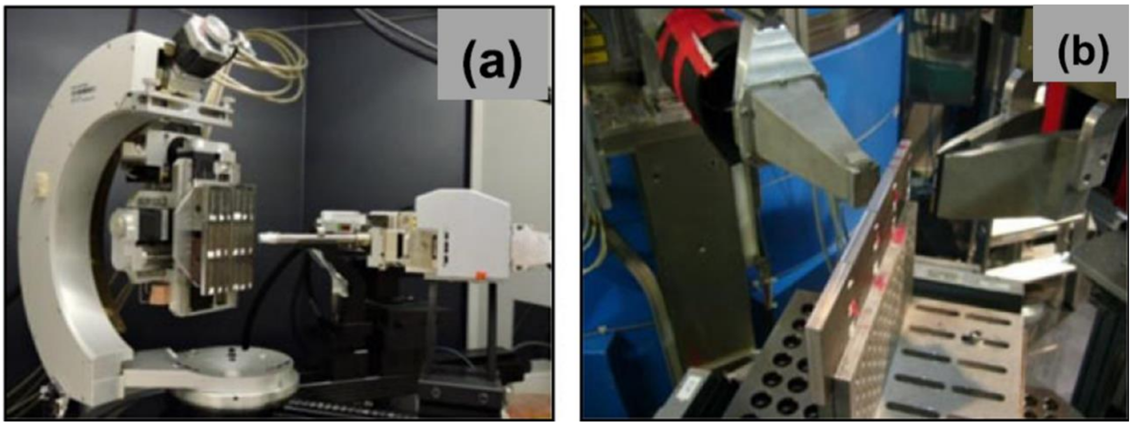

Fig. 3.4 Residual stress measurement. **(a)** X-ray. **(b)** neutron diffraction [48].

3.2.3 Numerical simulations

The authors carried out numerical simulation through a fully dynamic model (Abaqus explicit code). The simulation model for the numerical studies consisted of steel plate specimens of dimensions L=20 mm× B=10 mm× T=10 mm and a HFMI tool with a diameter of 4 mm at the tip, see Fig. 3.5. Hexahedral elements with reduced integration points were used to mesh the part, at which an element size in the treated region of 0.125 mm x 0.5 mm x 0.5mm was applied at the top up to a depth of 4 mm. A contact pair was defined between the tool (master surface) and the specimen (slave surface) with a friction coefficient of $\mu = 0.15$.

Force controlled and displacement controlled simulation of the HFMI process. The developed and calibrated material models by Foehrenbach [48], and secondary impacts were implemented by means of Abaqus user subroutines, see Fig. 3.6. Influence of the pin motion and the material model calibration were investigated.

In Ernould et al. [56], pin motion was implemented in Abaqus by means of a VUAMP subroutine (vectorized user amplitude) which specifies the amplitude of a force applied on the top of the pin, Fig. 3.6. This force accelerates the pin to the prescribed impact velocity as shown in Fig. 3.7. After each impact, the pin is maintained at its initial position awaiting for the next impact, see Fig. 3.6. To avoid instabilities and to reduce computational effort, pin is modeled as rigid body.

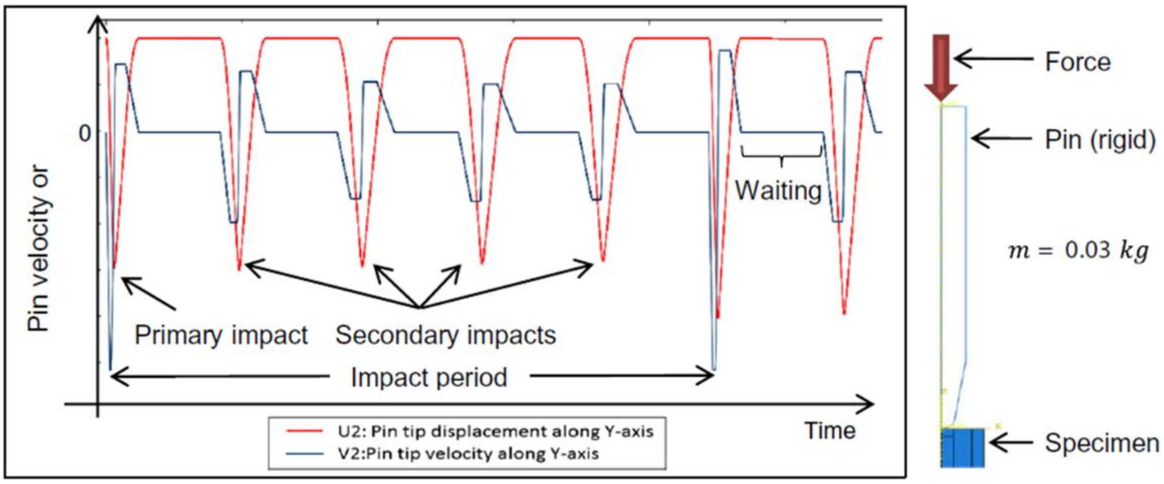

Fig. 3.6 Pin displacement and velocity along the normal direction (Y-dir.) [56].

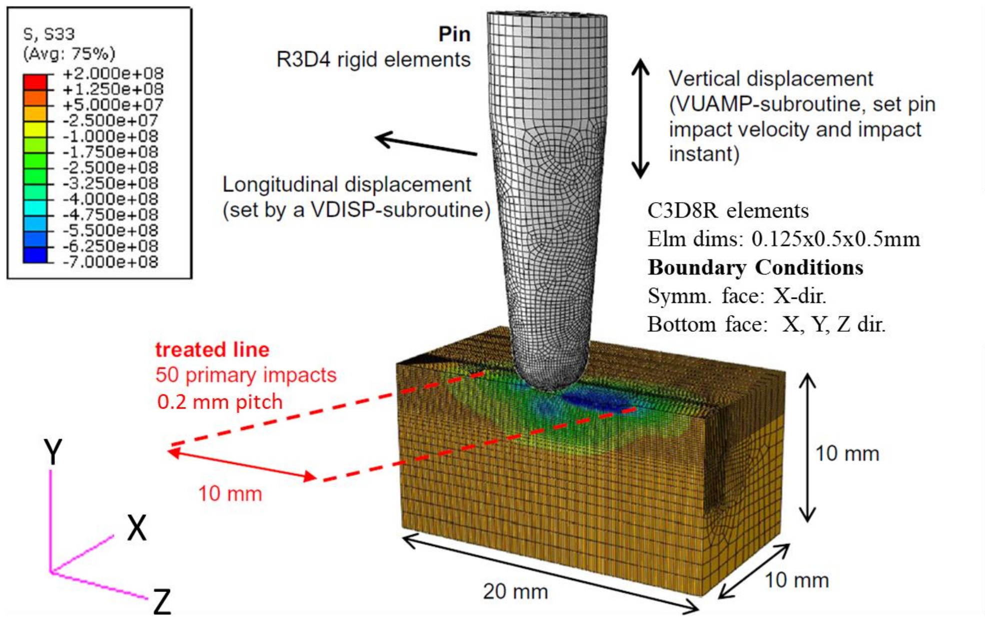

Fig. 3.7 3D finite-element model [56].

To simulate the HFMI process, 50 primary impacts were modeled and a feed rate of 0.2 mm/hit was chosen (0.04 mm/hit when considering the primary impacts and its four secondary impacts). To avoid mesh distortion, displacement of the pin along the treatment line was driven by a VDISP subroutine, Fig. 3.7. It prescribes translational boundary conditions and moves the pin only when its tip is not in contact with the specimen. The pin has a mass of 0.03 kg. In order to see the influence of secondary impacts, three different pin motion schemes were investigated, see Table 3.3. “50SP” corresponds to the typical impact period with four secondary impacts. “50HS V2745” does only simulation of primary impacts with Vi=2.745 m/s and 50HS V3229 with Vi=3.229 m/s. This value was chosen so that the kinetic energy of the pin before impacts equals that of (50SP) over an impact period. It is worth noticing that primary impact accounts for 72% of the total kinetic energy.

In that numerical simulation, two combined kinematic-isotropic hardening materials with strain-dependency were implemented. One is based on Chaboche model [58]. It was calibrated by Foehrenbach [48]. The second one was based on Ramaswamy-Stouffer model [82].

Table 3.3 Simulated schemes pin kinetic [56]

Pin kinetic scheme		50SP	50HS V2475	50HS V3229
Impact velocity *Vi* (m/s)	Primary impact	2.745	2.745	3.229
	Secondary impact n°1	1.037	–	–
	Secondary impact n°2	0.762	–	–
	Secondary impact n°3	0.793	–	–
	Secondary impact n°4	0.776	–	–
Total kinetic energy (J)		0.156	0.113	0.156

Figure 3.8 shows the computed residual stress fields when applying the 50SP showed that secondary impacts have no significant influence on the residual field in both components (longitudinal and transversal) for the applied simulation approach. Fig. 3.9 shows a comparison between the calculated residual stress and effective plastic strain and the stress and plastic strain measured by neutron diffraction. A better agreement can be observed with displacement controlled simulation than with force controlled simulation.

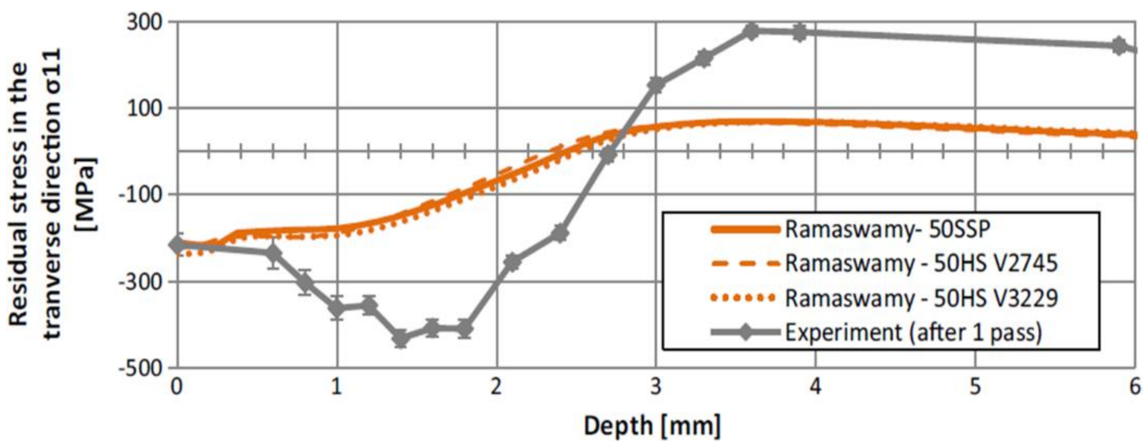

Fig. 3.8 Residual stresses in the transverse direction determine by neutron diffraction with travel speed of 12 cm/min [56].

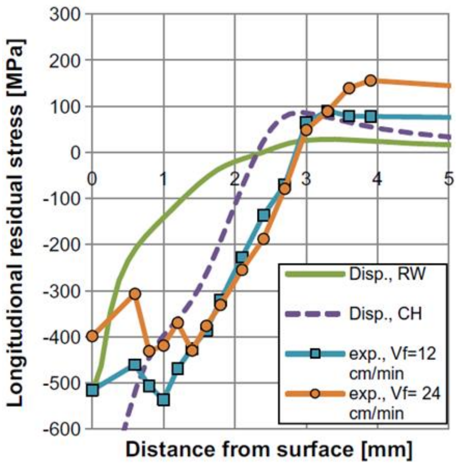

(a) longitudinal stress

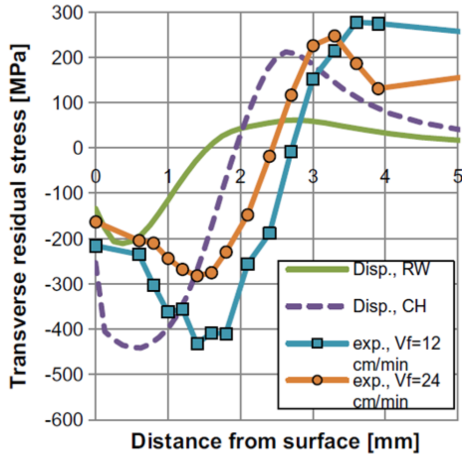

(b) transversal stress

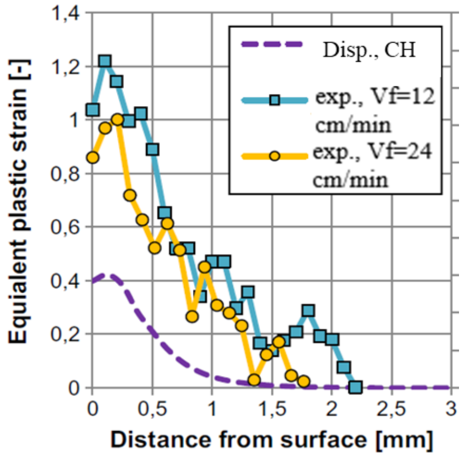

(c) effective plastic strain

Fig. 3.9 Comparison of numerical and experimental results [56].

3.3 Review of experimental study on out-of-plane gusset welded joint

Letiner et al. [66] investigated the effect of cyclic loading on the stability of compressive residual stress fields induced by HFMI post-weld treatment. The target is a single-sided non-load carrying longitudinal stiffener specimen. The authors considered specimens with different base material a mild steel S355 and a high-strength steel S960. The mild steel S355 specimen is taken as reference for this research. The size and shape of the specimen is shown in Fig. 3.10.

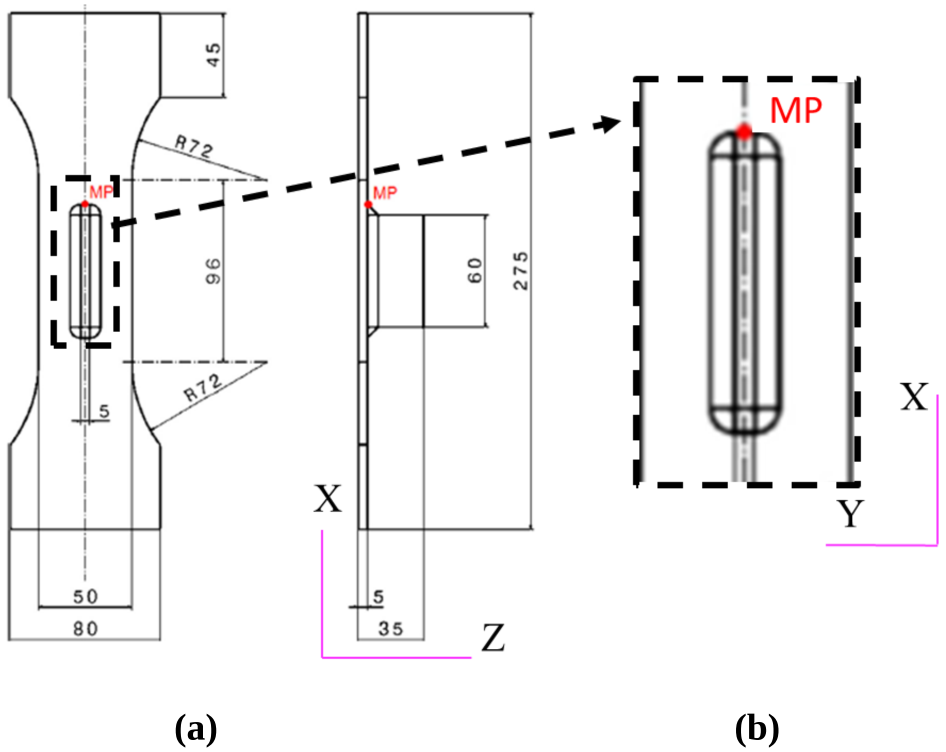

Fig. 3.10 (a) geometry of target out-of-plane gusset welded joint, dimensions in mm. **(b)** target location 'MP' [66].

Table 3.4 Nominal mechanical properties of steel S355 [66]

Type	Yield strength [MPa]	Ultimate tensile strength [MPa]	Elongation [%]
Base material	355	575	22
Filler material	440	530	30

The specimen was automatically gas metal arc welded by the aid of a welding robot. An industrially well-established filler material G3Si1, in combination with a M21 shielding gas (82% Ar, 18% CO_2), was used. Nominal mechanical properties of the investigated base material (according to EN 10025) and filler material (according to EN ISO 16834) are given in Table 3.4 for the mild steel S355 specimen.

Welding process parameters for the longitudinal weld areas were a welding speed vweld of 10 mm/s, wire feed rate, vwire, of 150 mm/s, nominal welding current I of 240 A, and a nominal welding voltage U of 25 V. In case of the end-of-seam areas the same welding speed were applied, but to minimize heat-input and ensure proper welding conditions, a reduced vwire of 100 mm/s with a nominal welding current I of 160 A, and a nominal welding voltage V of 21 V was operated.

Figure 3.11 (a) shows the welding equipment utilized in the automated welding process. During the welding process, the specimen was fixed by two clamps at the end of the base plate. Due to an optimized calibration of the weld process in the course of previous studies [83,84], a minimized angular distortion in the range of one-tenth degrees was finally observed, which also resulted in the course of a subsequently executed numerical simulation. In case of an increased angular distortion, the effect due to the clamping process on the residual stress at the weld toe during testing can be fundamental and needs to be incorporated as was shown in [85]. Fig. 3.11 (b) shows the application of the HFMI-treatment and a comparison of the resulting weld toe condition before and after HFMI.

All the HFMI process was executed with the pneumatic impact treatment (PIT) device [72]. Nominal pin radius, actuator frequency, and pneumatic pressure are defined as most relevant process parameters during the experiment [72]. A detailed representation of the local weld toe shape improvement utilizing laser-confocal microscopy and macrographs of the cross-section is depicted in Fig. 3.12. The macrographs in the subfigures clearly show the three typical microstructural regions of a welded joint, the filler material (FM), heat affected-zone (HAZ), and unaffected base material (BM). Furthermore, these revealed a smoothening of the notch shape up to a weld toe radius of about R = 2 mm in accordance to the applied pin radius in the course of the HFMI process.

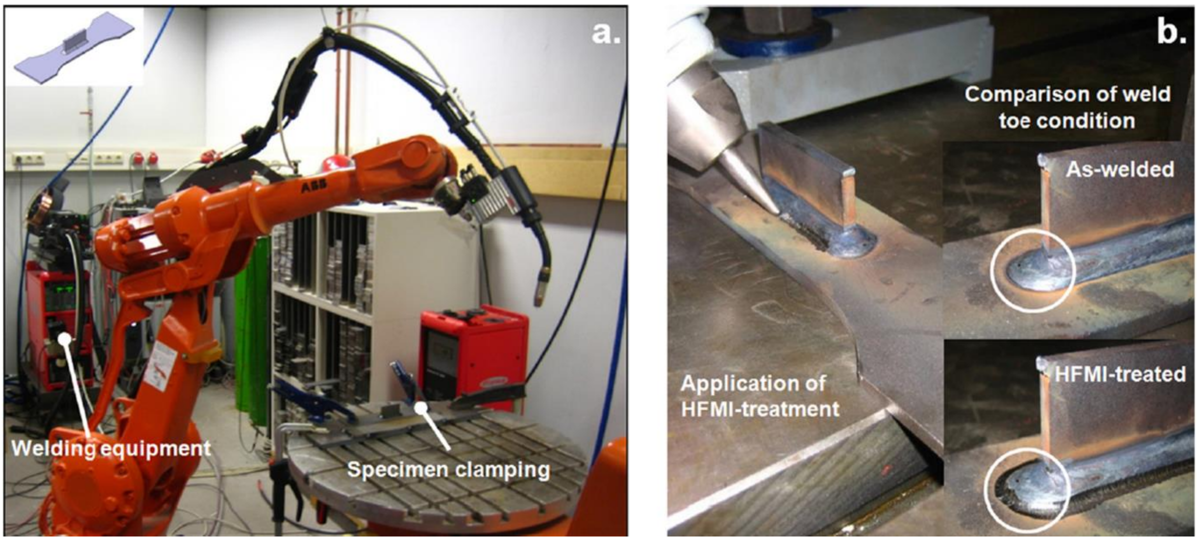

Fig. 3.11 (a) automated welding process. **(b)** HFMI treatment [66].

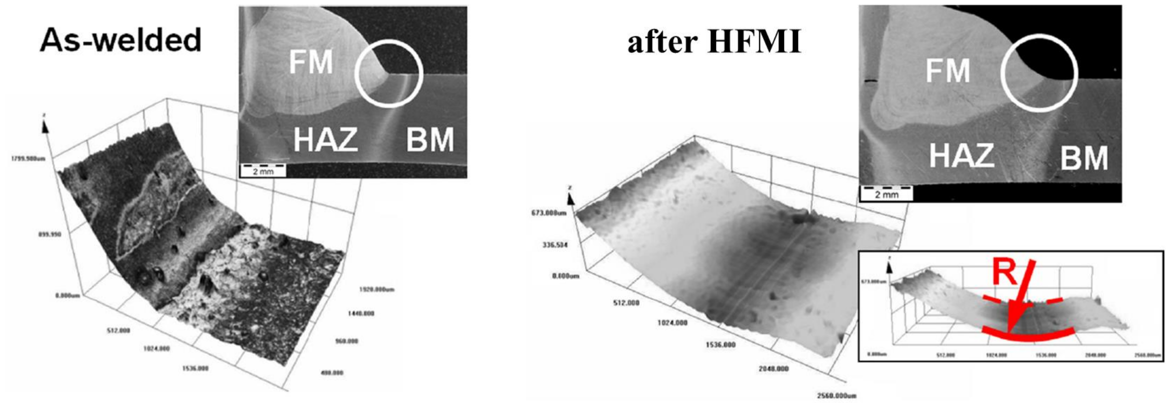

Fig. 3.12 Improvement of weld toe shape by HFMI [86].

3.3.1 Residual stress measurements

The residual stress field was measured by means of X-ray evaluation based on CrKa radiation using the d($\sin^2\Psi$) cross-correlation method with a collimator size of 1 mm, a duration of exposure of 20 sec, and a Young's modulus of 210 GPa. The as-welded and after HFMI residual stress were collected at the target location, "MP" in Fig. 3.10, of the investigated specimen.

The resulting residual stresses in welding transverse direction, X in Fig. 3.10, which is the loading direction during cyclic loading is shown in Fig. 3.13. The resulting residual stress conditions revealed a distinctive difference between the as-welded and after HFMI conditions, whereby a significant reduction of residual stress by HFMI was achieved up to a depth of 1.5 mm. Herein, the treated specimen exhibited a compressive residual stress in the first 50 µm of about -335 MPa almost equaling the nominal yield stress of the used base material. The authors concluded that after welding and HFMI, HFMI leads to a beneficial reduction of the residual stress in loading direction up to a depth of at least 1 mm at the weld toe. In fact, for mild steel S355, compressive stresses were measured up to a depth of 1.8 mm.

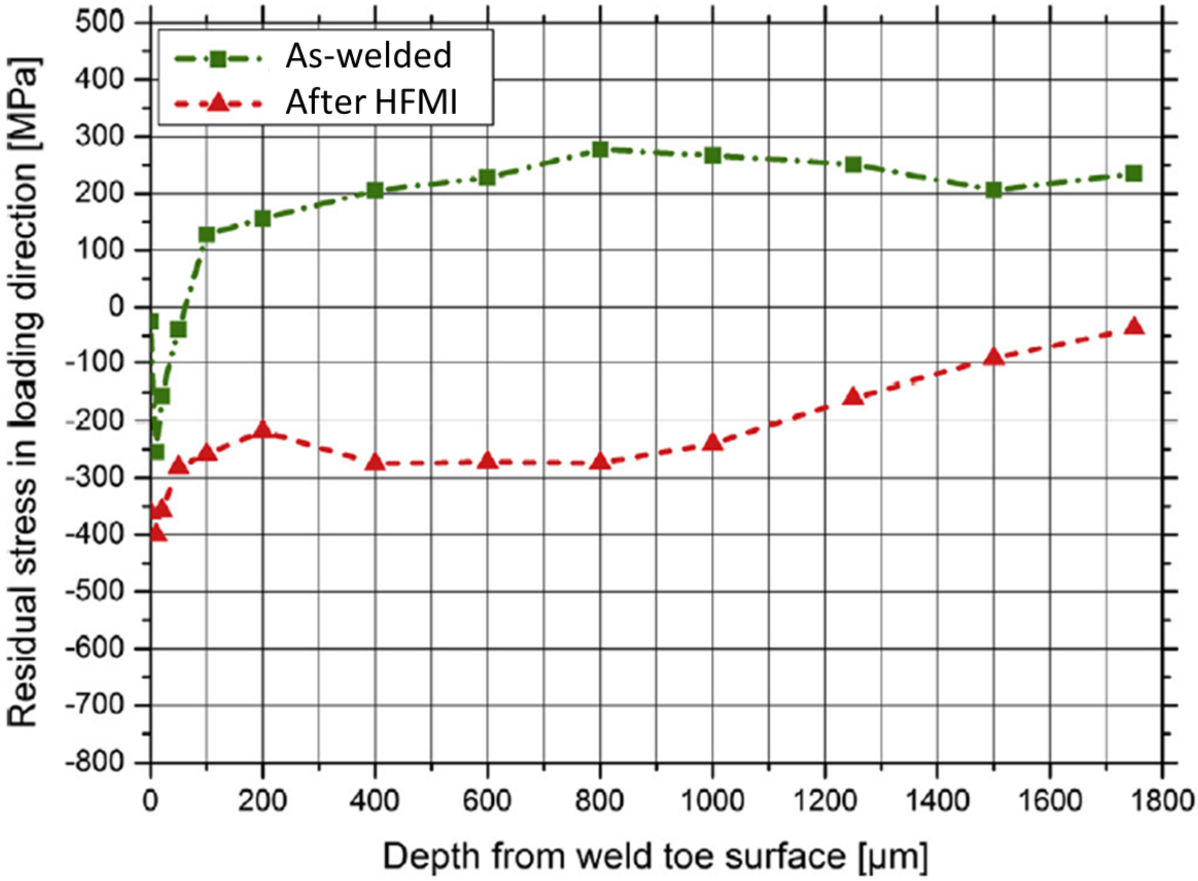

Fig. 3.13 Experimental longitudinal (S_{XX}) residual stresses [66].

Chapter 4 HFMI on a Flat Stress-Free Plate

4.1 Introduction

In this chapter, for a better understanding of the effect of different conditions on HFMI response, FE meshing and choice of HFMI conditions on a flat stress-free plate is investigated. Dynamic analysis using the explicit commercial code MSC. Dytran [71] is carried out and recommendations on simulation conditions are proposed.

In order to recommend a suitable FE mesh size in the peened region, a mesh sensitivity study using a flat stress-free plate is conducted. Then, using the recommended FE mesh size and kinematic hardening model introduced in section 2.3.1, comparisons of numerical simulation results is carried out with experimental measurements and with numerical data available in the literature [48, 56].

Next, the influence of HFMI conditions on the HFMI-induced residual stress is investigated. Selection of HFMI conditions such as impact pitch, impact frequency, indentation depth, yield stress, strain rate, etc., are considered. Comparison of the induced residual stress due to each HFMI condition with a reference case is carried out. Part of this study was included in the International Ship and Offshore Structures Congress (ISSC) ISSC'18 Committee V.3 benchmark.

4.2 Finite Element Mesh Sensitivity Simulation

4.2.1 Finite Element Model

Mesh sensitivity is studied by using the FE model shown in Fig. 4.1 referred to as ‘intermediate mesh’ against a ‘fine mesh’ and a ‘coarse mesh’ with smaller and larger element size respectively. The simulation target is a flat plate of S355J2H steel of 10 mm thickness studied by Foehrenbach et al. [48] and Ernould et al. [56]. The model and process are symmetric about the center plane. Therefore, only one half of the plate is modeled. Finite Element model is built of hexahedron brick elements as shown in Fig. 4.1.

The fine mesh (n_e, l_{min}) = 122459, 0.1x 0.1 x 0.1 mm. The intermediate mesh (n_e, l_{min}) = 105000, 0.2 x 0.2 x 0.2 mm. The coarse mesh (n_e, l_{min}) = 3938, 0.5 x 0.5 x 0.5 mm. Where n_e is the number of elements and l_{min} is the smallest element’s sizes in x, y, z directions in the treated region.

HFMI tool is composed of a conical pin and a guide. Pin nose radius is 2 mm same as in references [48], [56] and [66]. Rigid shell elements are used to model this tool. The tool is positioned, as shown in Fig. 4.1.

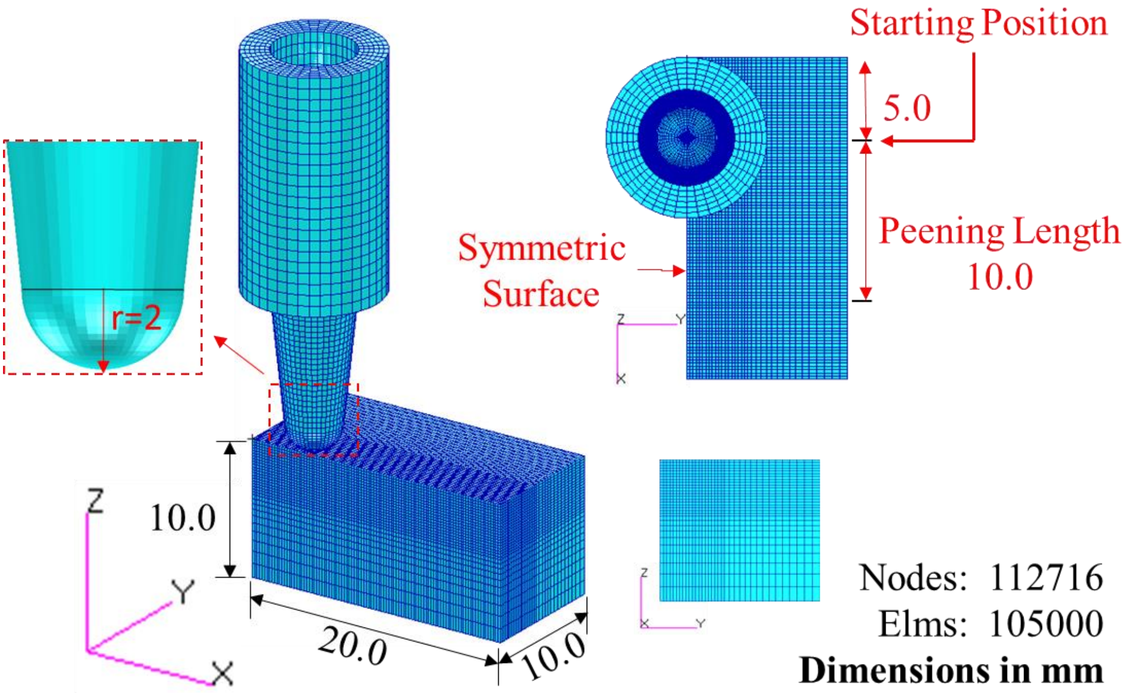

Fig. 4.1 FE mesh of the flat plate and HFMI tool ('intermediate mesh').

4.2.2 Boundary and HFMI Conditions

All nodes of the workpiece lower surface are prevented from motion, and nodes of the symmetric surface are prevented from transverse motion (Y-direction in Fig. 4.1).

HFMI analyses are either displacement-controlled simulations or force-controlled simulations. Pin's impact velocity or applied force has to be prescribed in force-controlled simulations. These are difficult to define such that indentations of depth similar to the measured indentation depth be produced. Therefore, displacement controlled simulation is chosen in this study. The peening pin is given an enforced oscillating motion along its axis with constant amplitude and frequency, such that the pin impacts the center of the plate (at the symmetry plane) and indents the plate surface with the required depth in each impact. The guide is given an enforced linear motion in X-direction with a velocity which depends on pin frequency such that every two successive impacts are spaced by the required pitch. Contact is defined between the pin and guide, and between the pin and workpiece. To reduce computational time, treatment is carried out only at the middle of the flat plate, see Fig. 4.1. HFMI parameters are shown in Table 4.1. Material hardening is not considered in this simulation, therefore, Von Mises yield criterion is used with the yield stress σ_o= 435MPa. Friction coefficient between the plate and the pin is μ = 0.3.

Table 4.1 HFMI Parameters

HFMI Length [mm]	Pitch [mm]	Indentation [mm]	Frequency [Hz]
10	0.4	0.2	100

4.2.3 Numerical Results

Simulation is carried out with each model to investigate the effect of element size on HFMI response. The average of the stresses in each line of elements in the center of the plate over 5 mm in the longitudinal direction at the same depth, from the surface and until 2mm depth, is obtained in order to minimize numerical noise, see Fig. 4.2. A comparison of longitudinal (S_{XX}) and transversal (S_{YY}) residual stresses distribution along the thickness direction from the surface is shown in Fig. 4.3 (a) and (b) respectively. Fig. 4.3 (c) shows the effective plastic strain.

Figure 4.3 (a) and (b) show that the stress distribution along the thickness direction has similar trend and magnitude with the fine and intermediate meshes. Even though at depth from 0.5 mm to 0.8 mm, the longitudinal S_{XX} residual stresses are different by about 19 % (-299 MPa to -247 MPa), at the most critical part at the top surface shows a difference of around 9% (-499 MPa to -415 MPa). On the other hand, the coarse mesh shows a different trends and magnitudes. Fig. 4.3 (c) shows that the effective plastic strains obtained by different mesh sizes have similar trends. However, the coarse mesh cannot represent the plastic strain behavior near the top surface as with the fine and intermediate mesh.

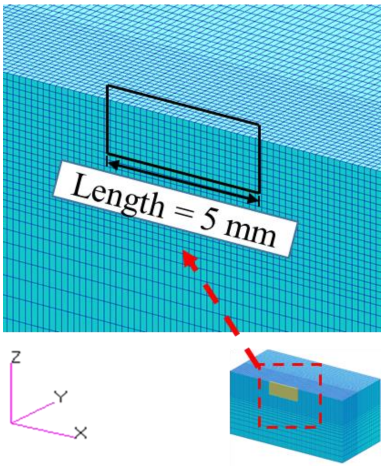

Fig. 4.2 Position of elements where results are chosen.

These results show that the element size in the treated region has a significant effect on results. From these results, it may be seen that the ratio of element size in the treated region/pin tip radius, should be equal or less than 0.1 in order to obtain reliable results. However, the computational time is an important factor to be considered. The simulation with the intermediate mesh is about 4 times faster than fine mesh. Therefore, in this study an element size of 0.2x0.2x0.2 mm (intermediate mesh) is used for further analyses.

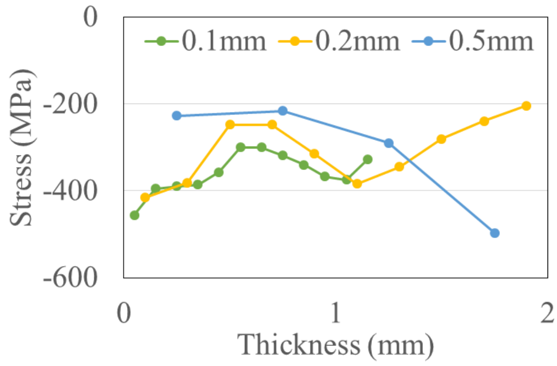

(a) longitudinal (S_{XX}) stress

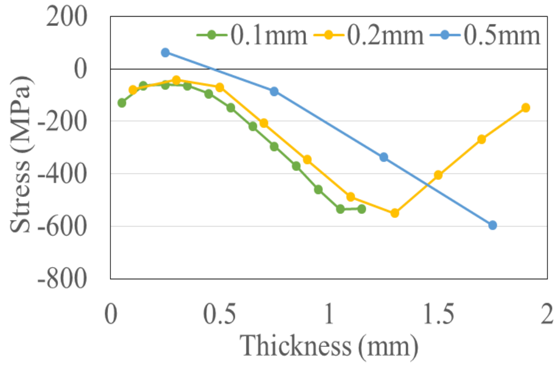

(b) transversal (S_{YY}) stress

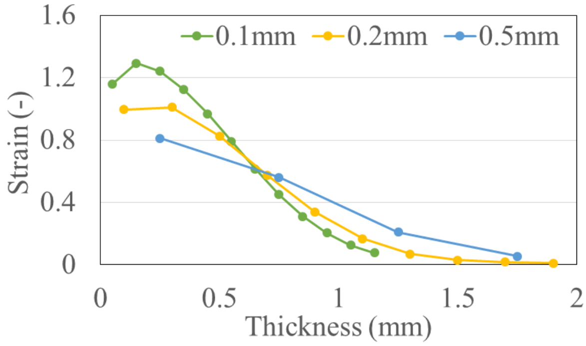

(c) effective plastic strain (EFFPLS)

Fig. 4.3 Mesh sensitivity comparison in the thickness direction.

4.3 Comparison of Numerical Simulation with Experiment

4.3.1 FE Model, Boundary and HFMI Conditions

The flat plate FE model (intermediate mesh), peening pin, and boundary conditions are the same as in the mesh sensitivity simulation, see Fig. 4.1.

The peening motion, HFMI parameters, and contact definition are the same as those in the mesh sensitivity simulation. However, to compare experimentally measured and numerically calculated residual stresses, it is thought that the same yield model used in Ref. [48-56] should be included in this simulation. The Chaboche's kinematic hardening law introduced in section 2.3.1 is implemented in Dytran by a user subroutine. The parameters "H" and "a" are set to large value and zero respectively to disable the isotropic part of hardening and strain rate effect (pure kinematic). Material parameters are the same as those presented in Table 3.2.

4.3.2 Comparison of Results

Figure 4.4 (a) and (b) show the stress distribution in the thickness direction of longitudinal (S_{XX}) and transversal (S_{YY}) residual stresses, and Fig. 4.4 (c) shows the effective plastic strain. This stress distribution is compared with experimental data in Foehrenbach et al. [48] and numerical results presented in Ernould et al. [56], getting a reasonable agreement with experimental results. Differences with Ernould's numerical results may be caused by the difference in the element formulation, element size and peening motion.

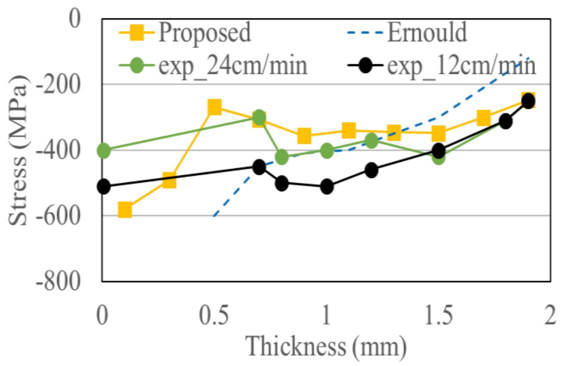

(a) longitudinal (S_{XX}) stress

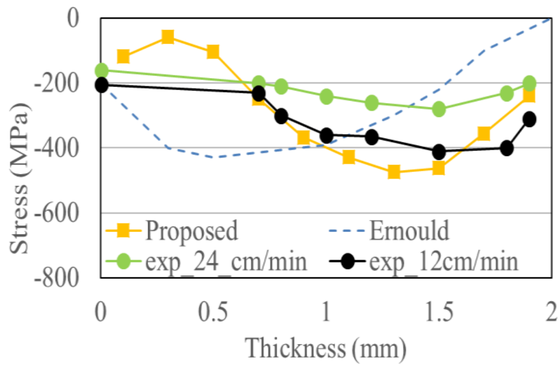

(b) transversal (S_{YY}) stress

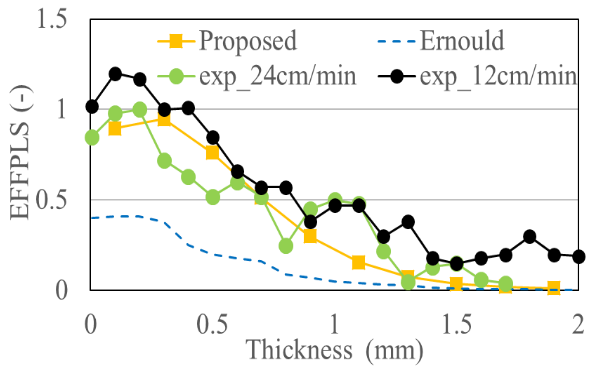

(c) effective plastic strain.

Fig. 4.4 Comparison between experimental and numerical results.

Longitudinal (S_{XX}) residual stress and effective plastic strain (EFFPLS) distribution along the treated path are shown in Fig. 4.5 (a) and (b) respectively. A closer view of the deformation shape (Z-displacement) produced by HFMI is shown by a cross section view at the middle of the treated path, see Fig. 4.5 (c).

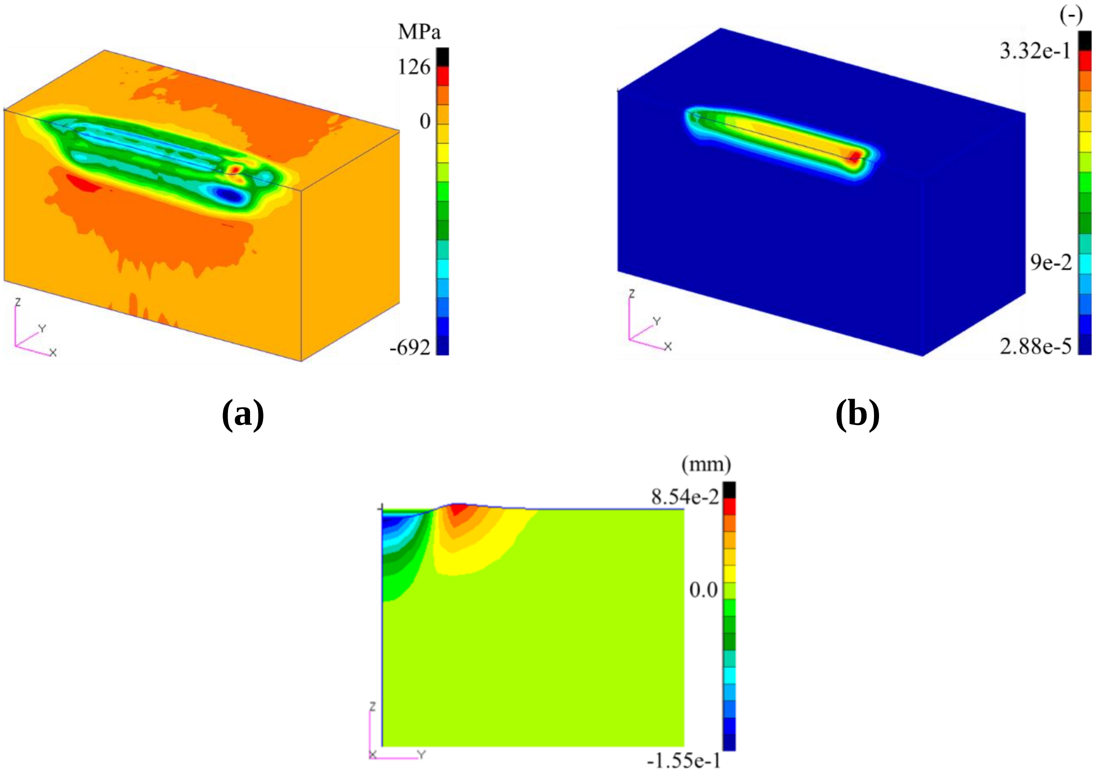

(a) **(b)**

(c)

Fig. 4.5 (a) longitudinal (S_{XX}) stress, **(b)** effective plastic strain, **(c)** Z-disp.

4.4 Study on the Influence of HFMI Conditions

In this section, comparison of the induced residual stress is shown when different parameters are considered. Table 4.2 shows the parameters used, with a total of 288 possible cases. For a better understanding of the effect of these parameters on HFMI response, a reference case is analyzed, then parameters are varied one at a time to see the effect of this parameter. HFMI tool moves with a frequency of 100Hz. Stresses are compared with the reference case. This comparison is focused on the top surface, where cracks usually arise after welding process is performed.

Table 4.2 Parameters considered

Parameters	Reference case	Variations	
Pitch (mm)	0.4	0.2	
Depth (mm)	0.2	0.1	0.3
Yield Stress (MPa)	435	210	650
Hardening	Kinematic	Non	
Hardening Coefficients	Table 3.2	Non	0.5 of Table 3.2
Strain rate dependence	no	Yes	
Radius of pin nose (mm)	2	3	

- Effect of hardening is investigated with a simulation where hardening is not considered. Also, two different hardening coefficients values are considered, reference coefficients and half of the reference coefficients, see Table 3.2. Fig. 4.6 shows a comparison of each stress component in an element on top surface at mid-length using different hardening coefficient values, see Fig. 4.2. It is overserved that longitudinal (S_{XX}) stress increases with the hardening.

- Effect of HFMI indentation depth is shown in Fig. 4.7. Three different HFMI indentations depth are considered 0.1, 0.2 and 0.3 mm. Normal components (S_{XX}, S_{YY}, and S_{ZZ}) increase with the depth indentation.

- Effect of yield stress is shown in Fig. 4.8. Three different values of the yield stress (210, 435 and 650 MPa) are considered for these analyses. It is observed that the longitudinal (S_{XX}) stress increases with the yield stress.

- Effect of strain rate: The Cowper-Symonds strain rate hardening parameters "H" and "*p*" are set to 4000.0 and 5.8 respectively [87], see Eqn. 2.5. The isotropic strain hardening parameters of Johnson-Cook strain function "a" and “b” are set to 0.000001 and 0.6 respectively, see Eqn. 2.6. Fig. 4.9 shows a comparison between two different strain rate conditions (not considered and considered). Mainly, S_{XX} increases when the strain rate is taken into account. Appendix A, shows the stress-time comparison between the reference case and the case with consideration of strain rate.

- The effect on HFMI induced residual stress was investigated, such as impact pitch (0.2 - 0.4 mm). This parameter has shown that stress components variation may be neglected, see Fig. 4.10.
- The effect of pin radius shows negligible changes, see Fig. 4.11.

Recommendations of optimum simulation conditions:

- The ratio of element size in the treated region/pin tip radius, should be equal or less than 0.1 in order to obtain reliable results.

- Hardening should be taken into account to get accurate residual stress trend in the thickness direction.

- Higher compressive residual stresses may be obtained with higher yield stress, deeper indentation.

- Strain rate has shown moderate influence on normal residual stress components. However, for simplicity of collecting material properties, analysis of residual stress induced by HFMI without consideration of strain rate dependency is adopted and found to lead to reasonable agreement with experiments.

- Moderate variation of Impact pitch and radius of pin may be neglected.

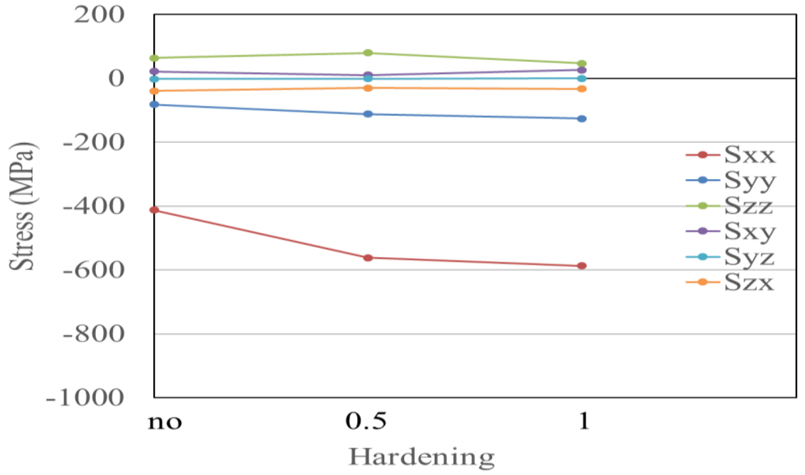

Fig. 4.6 Effect of hardening.

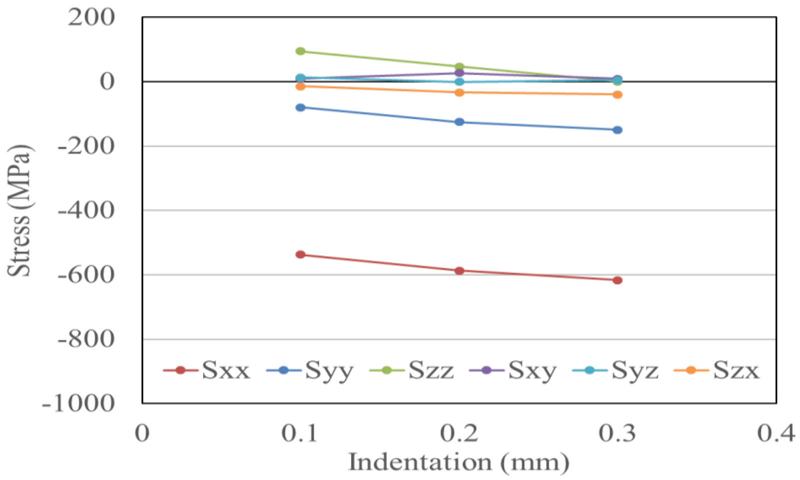

Fig. 4.7 Effect of HFMI indentation depth.

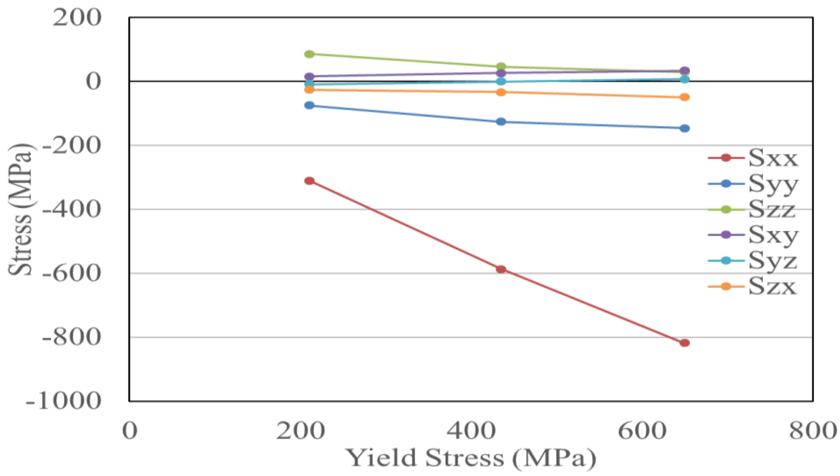

Fig. 4.8 Effect of yield stress.

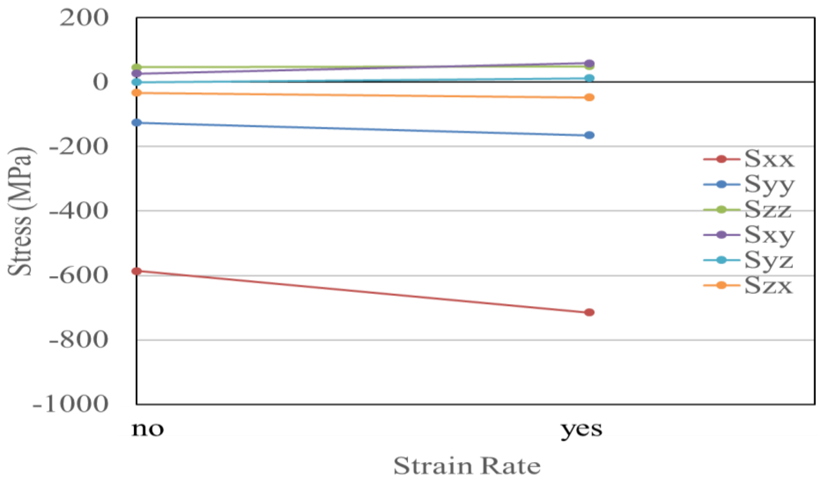

Fig. 4.9 Effect of strain rate.

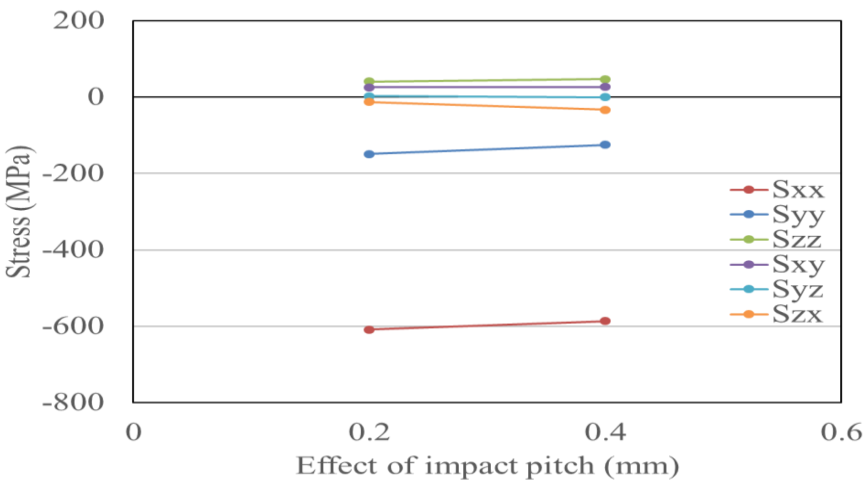

Fig. 4.10 Effect of impact pitch.

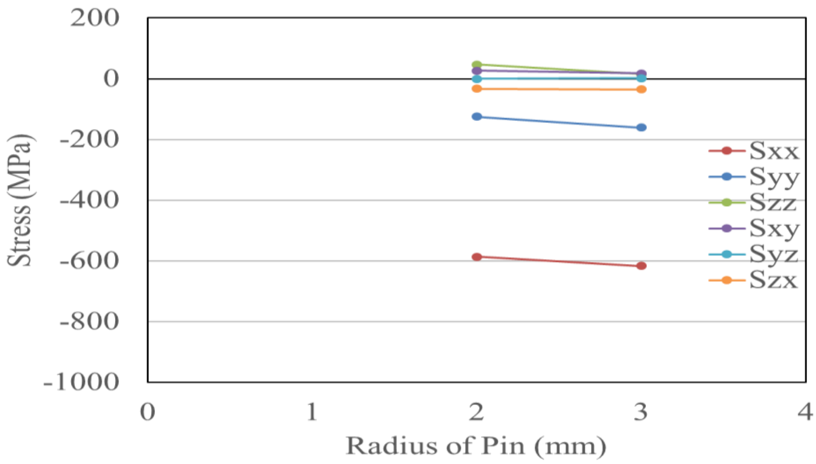

Fig. 4.11 Effect of radius of pin.

4.5 Conclusion

This chapter investigated the HFMI induced residual stress in a flat stress-free plate by means of dynamic analysis using the commercial code MSC. Dytran. First, a FE mesh sensitivity study was conducted, showing significant mesh sensitivity in the peened region. An element size in the treated region of less than or equal to one tenth of the pin tip radius is recommended. Then, the validity of the proposed numerical simulation using the recommended FE mesh size and kinematic hardening material is demonstrated by comparison with experimental measurements and numerical results, improving the numerical results presented in Ernould et al. [56]. Finally, optimum simulation conditions were proposed through a study on the influence of different HFMI simulation conditions. The obtained optimum conditions will be used in further numerical simulation.

Chapter 5 HFMI Simulation on an Out-of-Plane Gusset Welded Joint

5.1 Introduction

Following the optimum simulation conditions for a flat plate presented in chapter 4. A practical simulation of welding, followed by HFMI is examined through simulation. The target is an out of plane gusset welded joint used by Leitner et al. [66, 88]. First, welding process is carried out using the in-house code JWRIAN [68]. The computed stresses are compared with numerical results obtained by Pusan National University [PNU] and trend is verified with experimental measurement by [66].

Next, the computed residual stress field by JWRIAN are imported into MSC.Dytran [71] to predict the compressive residual stresses induced by the HFMI post-welding treatment. Finally, behavior of the computed residual stress after HFMI, through the thickness direction of the main plate at the target location is shown together with experimental measurement presented in [66].

Part of this study was included in the International Ship and Offshore Structures Congress (ISSC) ISSC'18 Committee V.3 benchmark.

5.2 Numerical Simulation of the Welding Process

5.2.1 Numerical Simulation Overview

In this study, the mechanical behavior due to welding of the out of plane gusset welded joint investigated by Leitner et al. [66] is analyzed numerically.

Welding simulation is carried out using Thermal Elastic-Plastic Finite Element code JWRIAN [68]. The computed welding residual stresses are compared with the computed stresses obtained by Pusan National University [PNU] by using the commercial code Abaqus. Also trend of the computed residual stress after HFMI is compared with experimental measurements in [66].

5.2.2 FE model, Material Properties and Welding Conditions

A half model of the target joint was used by Leitner et al. [66, 88] to perform welding-HFMI numerical analyses. In their model, the minimum element edge length was comparable with the pin radius (=2mm). This is deviating from the recommendation presented in chapter 4. Therefore, Leitner's model was remeshed such that the element edge length in the HFMI-treated area fits the recommendation of 0.2 x 0.2 x 0.2 mm. This new mesh is built of hexahedron brick elements and shown in Fig. 5.1. X, Y and Z coordinates shown in this figure are used in following discussions.

In the Thermal Elastic-Plastic Analysis, due to lack of information on experimental material properties. The temperature dependent material properties used by Kim [89] is adopted, see Fig. 5.2. In this study, phase transformation is not considered, because in mild steel S355 as well as filler material G3Si1, phase transformation occurs at high temperature and its effects on residual stresses may not be significant.

Goldak heat source model is adopted for the thermal simulation [90], see Fig. 5.3. Fig. 5.4 shows the welding conditions for each welding pass. Only rigid body motion of the workpiece is prevented during the welding simulation, see Fig. 5.1.

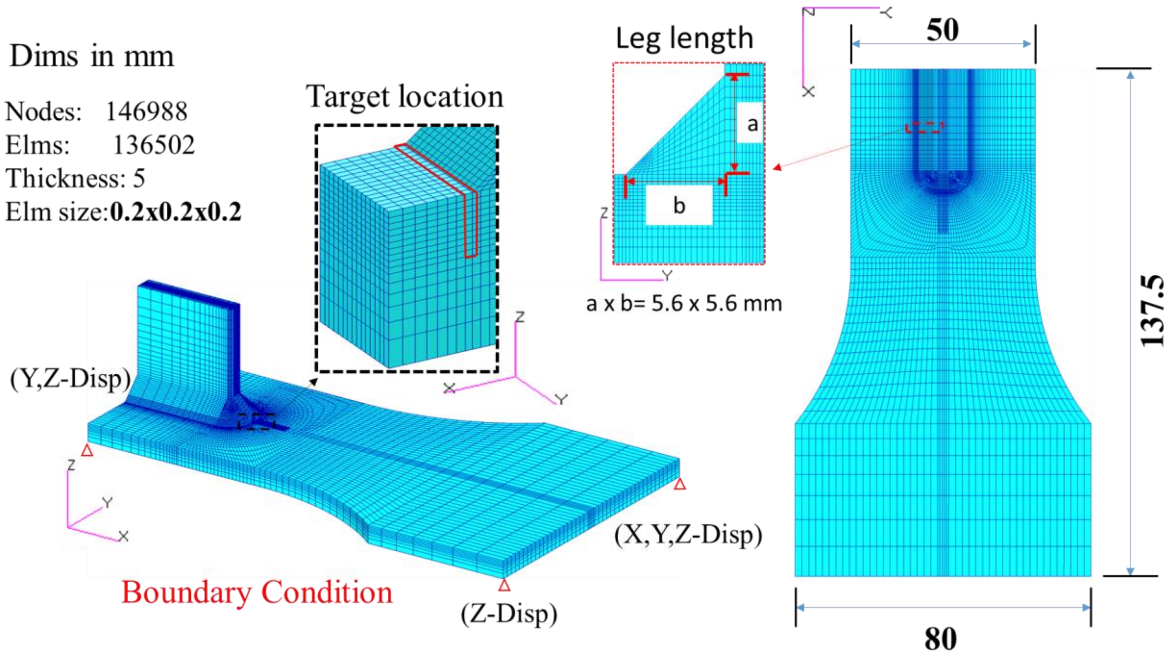

Fig. 5.1 Welding model.

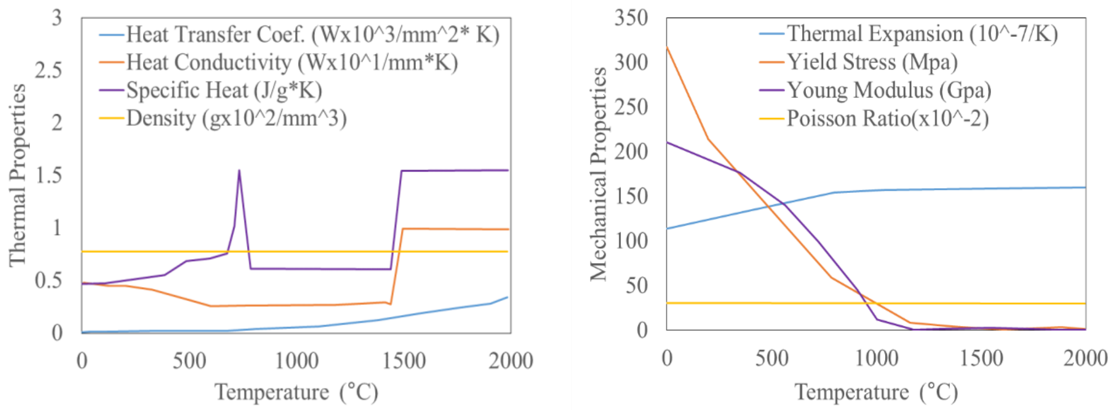

(a) Thermal properties **(b)** Mechanical properties

Fig. 5.2 Temperature dependent material properties.

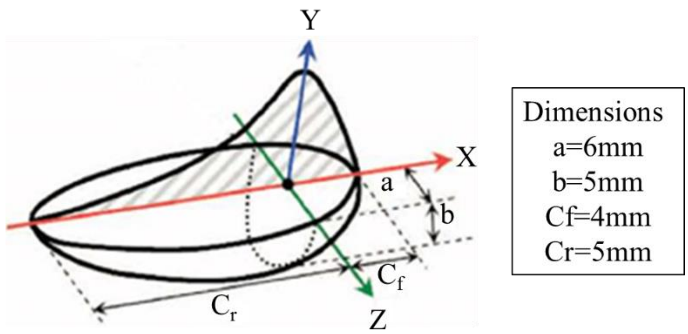

Fig. 5.3 Goldak heat source model.

Pass	Joint Type	Ampere (A)	Voltage (V)	Travel Speed (mm/s)	Efficiency
1	Fillet Seam_1	260	21	8.5	0.85
2	Rounded Seam	260	21	8.5	0.85
3	Fillet Seam_2	260	21	10.2	0.85

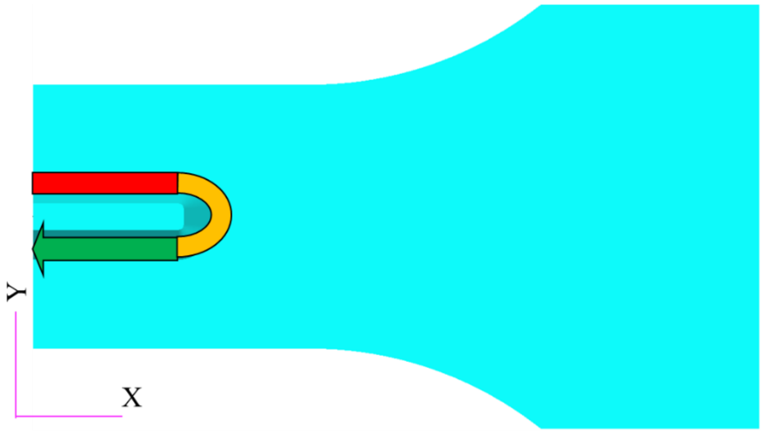

Fig. 5.4 Welding conditions and sequence around the vertical attachment.

5.2.3 Thermal Results

Figure 5.5 shows a cross-section of the simulated fusion zone of the weld, having a maximum temperature of about 2470 °C.

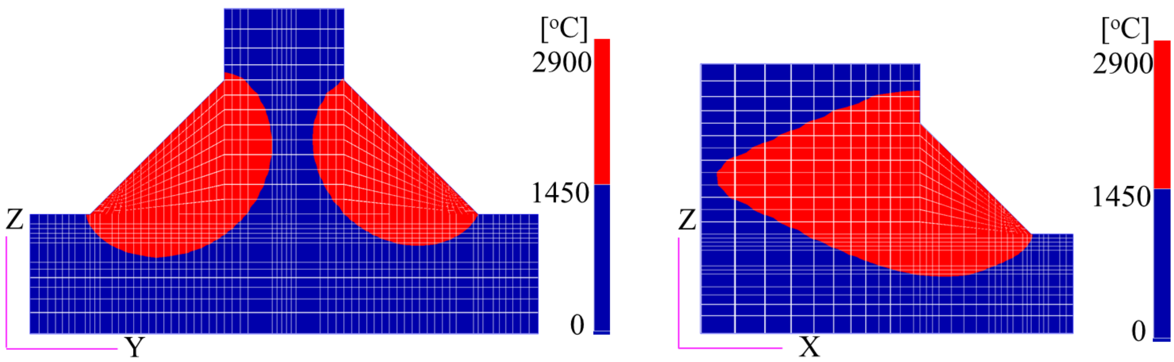

(a) Straight seam **(b)** Target location

Fig. 5.5 Fusion zone cross section.

5.2.4 Mechanical Results

Figure 5.6 shows the longitudinal (S_{XX}), transversal (S_{YY}) residual stress and Von Mises (VM) stress, obtained by the mechanical simulation after the model has cooled down to room temperature. Higher tensile residual stress concentration is observed at the end of the vertical attachment. Fig. 5.7 shows a cross section view of the longitudinal (S_{XX}), transversal (S_{YY}) residual stress and Von Mises (VM) stress at the target location. Longitudinal (S_{XX}) and transversal (S_{YY}) residual stresses show compressive residual stress in a thin layer at the surface of the filler metal. This is because the thin layer at the surface of the filler metal cools faster than the rest of the filler metal. A study of out of plane gusset joint focusing on the crack growth in welded structures by Murakawa [91] showed similar residual stress field at the target location.

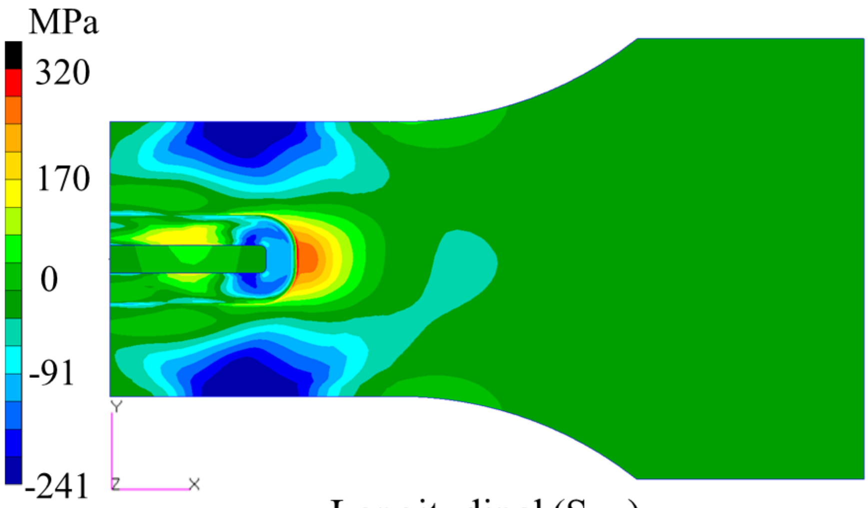

Longitudinal (S_{XX})

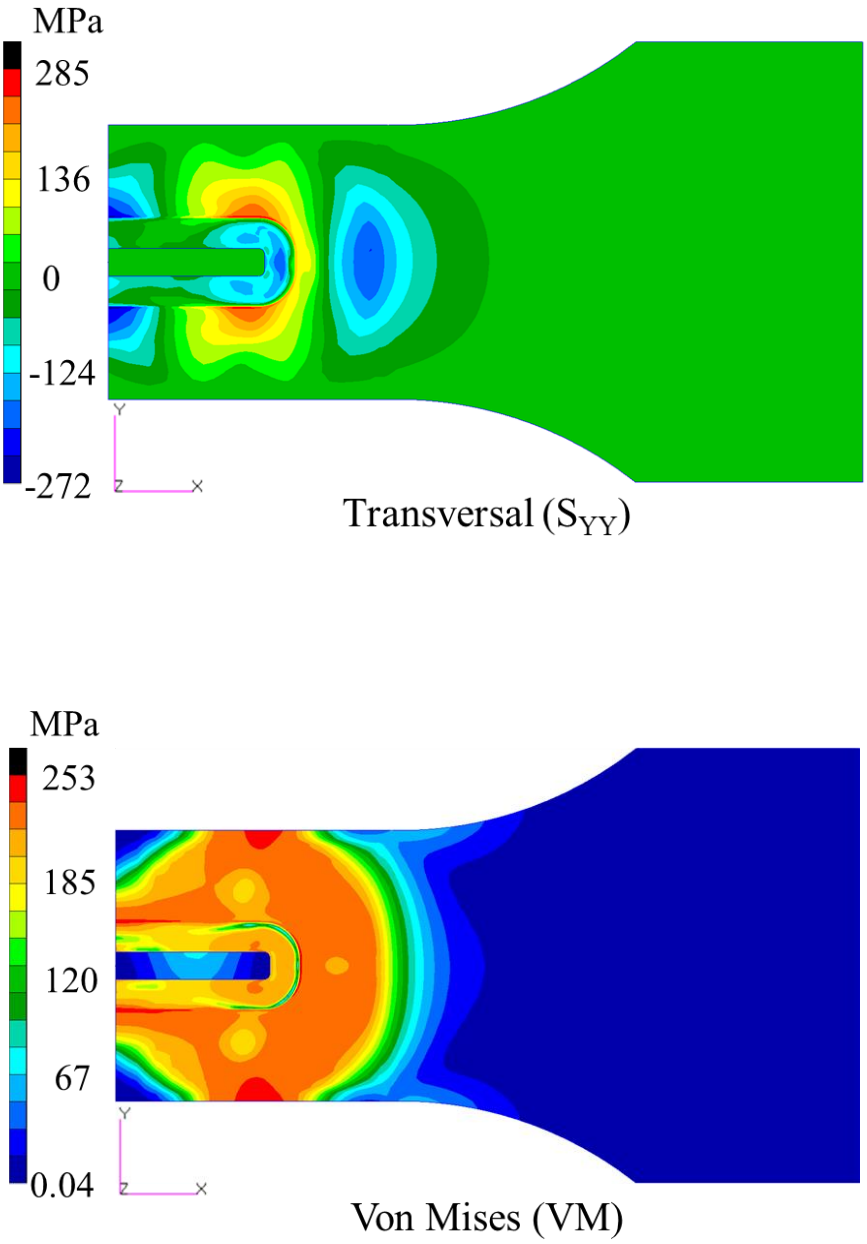

Fig. 5.6 Welding residual stress.

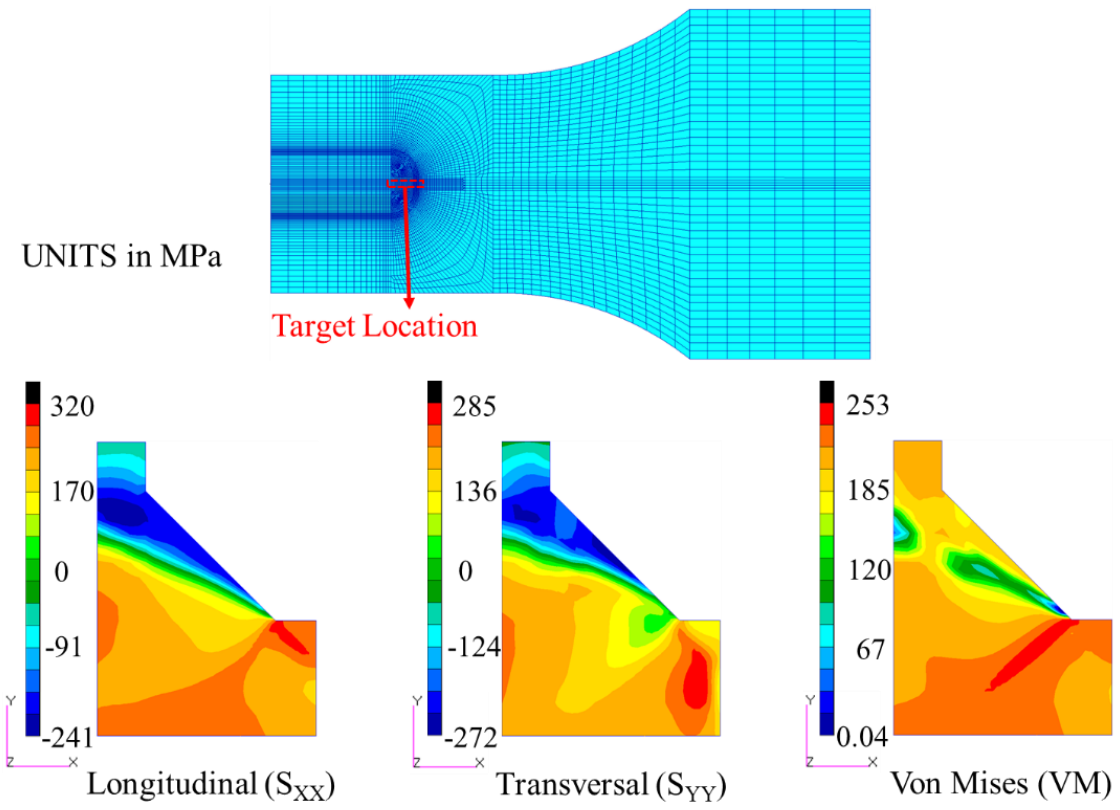

Fig. 5.7 Welding residual stress at the target location.

Figure 5.8 shows a comparison between the computed welding residual stress obtained by JWRIAN and that independently obtained by Abaqus. Similar trends of stress variation through the thickness of the main plate at the target location may be observed. Differences in stress levels may be caused by different element formulations in the two codes and different modeling methods of welding conditions, for example the used heat source model and heat input to weld elements.

Similarly, experimental measurements [66] of stress through the thickness of the main plate at the target location is also shown in Fig. 5.8. Similar trend to the computed results may be observed. It should be noted that different materials were assumed due to lack of exact properties of the material used in the experiment. Experimental compressive residual stress in the longitudinal direction (X-dir.) near the top surface (0.01mm to 0.08mm) may be caused by the heat convection between air with the surface of the weld bead, causing the bead surface to cool faster than the bead internal material. Residual stress increases from 0.1mm to 0.6mm, this behavior may be caused by experimental measurement errors.

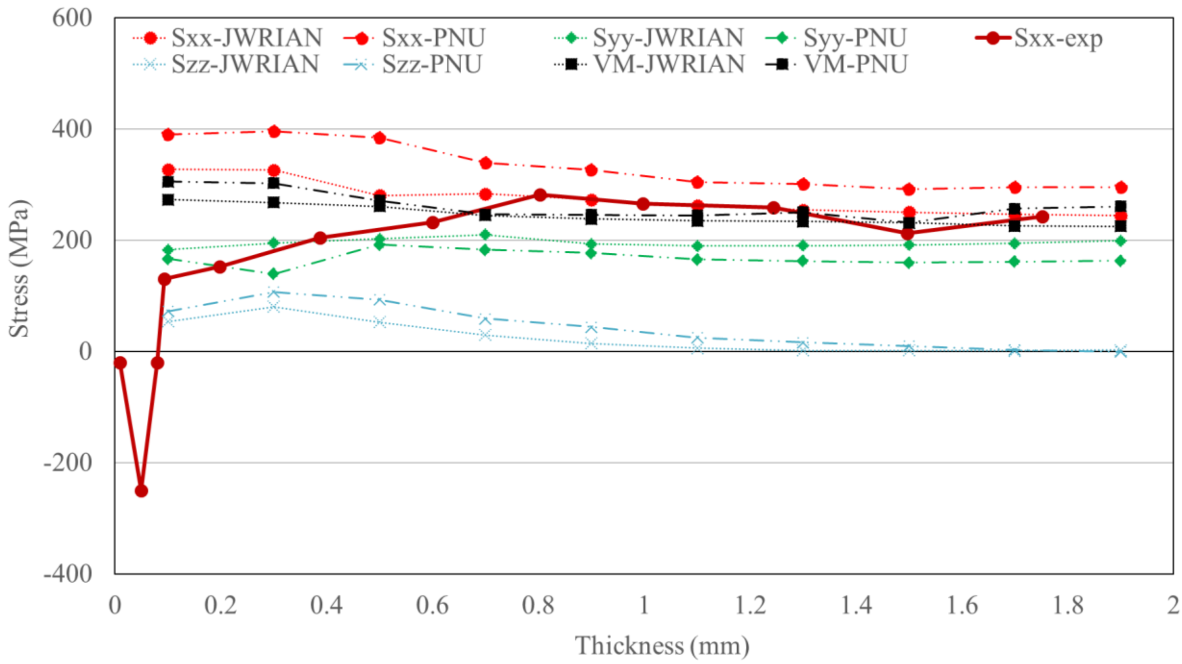

Fig. 5.8 Welding residual stress comparison in the thickness direction.

5.3 Numerical Simulation of HFMI

5.3.1 Numerical Simulation Overview

Following the welding simulation, the mechanical behavior due to HFMI of the welded joint is investigated. HFMI process is simulated by means of dynamic analysis using the explicit commercial code MSC.Dytran [71]. First, HFMI response on a stress-free model is investigated. Then, results are compared with those obtained when welding residual stresses computed by JWRIAN are considered. The computed welding residual stress field computed by JWRIAN is imported as initial stress in MSC.Dytran using a user subroutine developed for this purpose. This subroutine is explained in the next section.

5.3.2 Importing Welding Residual Stress Field

In MSC.Dytran the user can create his own code in a "user subroutine" which can be compiled with MSC.Dytran. Dytran will then call the user subroutine during the simulation. Several plugs for user subroutines are available and can be used to plug and call user subroutines from the program at different times in the simulation cycle. Stress may be initialized in MSC.Dytran by two different methods;

- By specifying the stress for element groups or geometric regions in the input file. However, this is effective if the stress is uniform over a large number of elements or over geometric regions. Preparing such data for welding residual stress can be tedious.

- By using a user subroutine. One of the available subroutines, "EXINIT.f" is intended to set initial conditions in Dytran model at the beginning of the simulation. The user may code this user subroutine to set any initial conditions he may want to set at the beginning of the simulation.

In this study the user subroutine EXINIT.f is used. It is coded such that it reads JWRIAN residual stress components of each element from JWRIAN results, do any necessary adjustments to account for a possible difference in the units used in JWRIAN and DYTRAN models, then set these stresses as initial stress in Dytran model at the beginning of the HFMI simulation. It is to be noted that the same model is used in JWRIAN and Dytran. Therefore, element stresses are set one to one and there is no need for interpolation mapping.

However, reduced integration (one integration point in the element center) is adopted in Dytran's HFMI analyses while selective reduced integration (8 integration points) is used in JWRIAN welding simulation. Because of this difference, it was thought that Dytran model's initial stress imported from JWRIAN results may not be in equilibrium, and this may cause numerical noise. In order to remove this noise, a short time (0.002 s) is allowed to let stresses to settle down and the unbalance forces to vanish. During this period, damping of 20% of the critical damping is applied. Following this procedure, an equilibrium state is achieved in Dytran model. In fact, it was found that, in the analyzed gusset joint, the unbalance forces in Dytran at the time of stress import from JWRIAN were very small. Stress after achieving equilibrium was different from that imported by a maximum of less than 1%. Fig. 5.9 shows the comparison of JWRIAN longitudinal (S_{XX}) residual stress with that after reaching equilibrium in Dytran. The black spot in fig. 5.9 (b) is the peening tool.

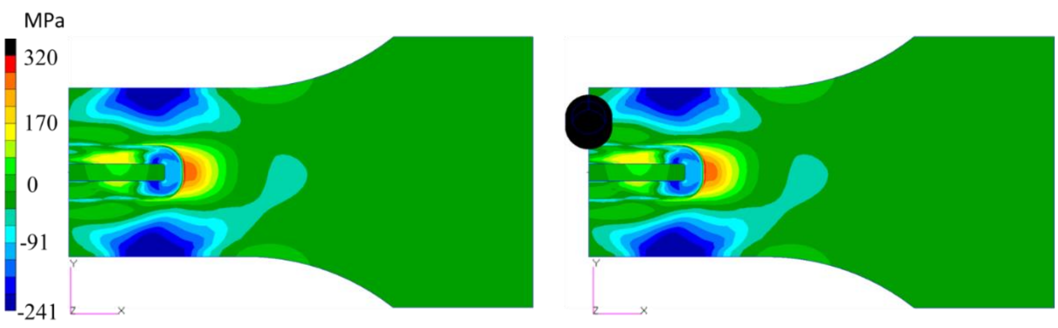

(a) **(b)**

Fig. 5.9 Longitudinal (Sxx) residual stress. **(a)** JWRIAN. **(b)** Dytran.

In HFMI simulation, kinematic hardening is adopted. Naturally, hardening depends on the plastic strain. It may look attractive to initialize the plastic strain in HFMI simulation from JWRIAN results. However, in welding, most of the plastic strain occurs at high temperature and it is unclear what would be its effect on hardening in HFMI simulation. In order to include the effect of welding on material properties, it is necessary to test specimens taken from the weld and HAZ. This is not considered in the present simulation.

5.3.3 Boundary and HFMI Conditions

As mentioned before, the FE model used for HFMI simulation is the same as that used for welding simulation. As in HFMI on a flat plate, peening tool is composed of a conical pin and a guide. Pin nose radius is 2 mm. Rigid shell elements are used to model this tool. The tool is positioned, as shown in Fig. 5.10. All nodes of the workpiece lower surface are prevented from motion in the Z-direction; the symmetry face is fixed only in the X-direction, and one node only is fixed in the Y-direction, see Fig. 5.11.

As in the stress-free flat plate simulation, displacement controlled simulation is adopted in this study. The indentation depth and the impact period are assumed constant. To reduce computational time, HFMI is carried out only at the weld toe around the end of the attachment, see Fig. 5.10. Chaboche kinematic hardening model is implemented, material parameters are shown in Table 3.2. The parameters “H” and “a” are set to large value and zero respectively to disable the strain rate effect and isotropic part of hardening (pure kinematic) as was were adopted in section 4.3. Friction coefficient μ between the joint and pin is taken as μ = 0.3. Table 5.1 shows the HFMI parameters.

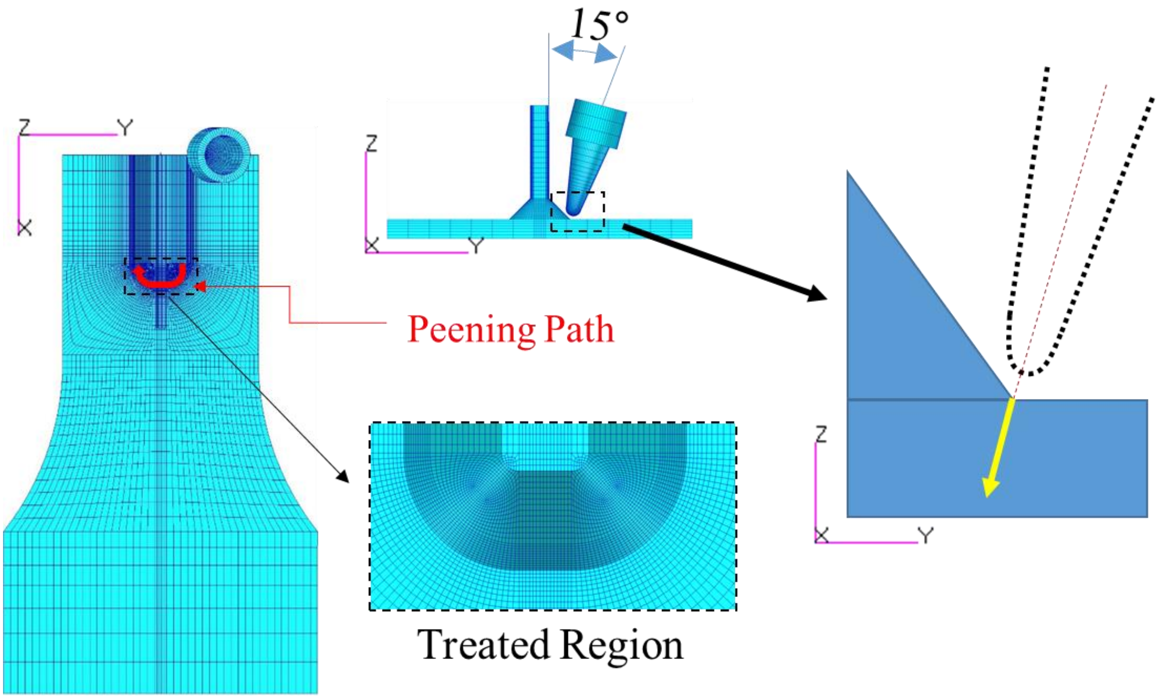

Fig. 5.10 Position of the peening tool and peened region.

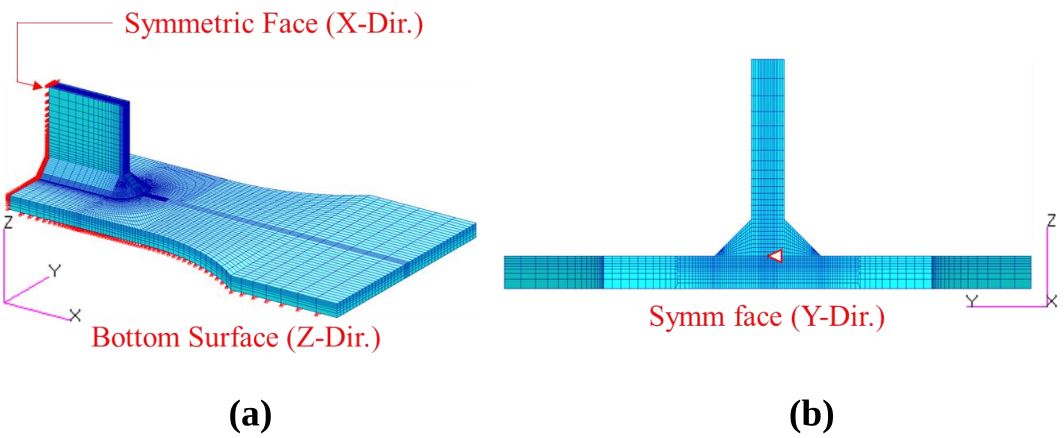

Fig. 5.11 Boundary conditions. **(a)** bottom surface. **(b)** symmetric face.

Table 5.1 HFMI parameters

Parameters	Values
HFMI Length (mm)	23.7
Indentation depth (mm)	0.2
Pitch (mm)	0.4
Frequency (Hz)	100

5.3.4 Results

Many researchers have the hypothesis that welding residual stresses may be neglected in the study of HFMI simulation because most of the stresses are superimposed during the post-welding treatment. Therefore, the compressive residual stresses induced by HFMI considering and not considering welding residual stresses are compared to investigate the reliability of this hypothesis. Fig. 5.12 shows a comparison of the longitudinal (S_{XX}) residual stress field after HFMI a stress-free model and after HFMI a model with welding residual stresses. This comparison shows a similar stress distribution in the peened region. However, a different stress field around the target location which may have effect in the thickness direction is observed. A comparison of the computed longitudinal (S_{XX}) residual stress in the thickness direction at the target location is shown in Fig. 5.13. Results show similar trend, but, a difference of about 23% (-480 MPa to -379 MPa) near the top surface, having a maximum difference of about 41% in the thickness direction. This difference reveals that welding residual stresses cannot be neglected in the numerical simulation of residual stress after HFMI.

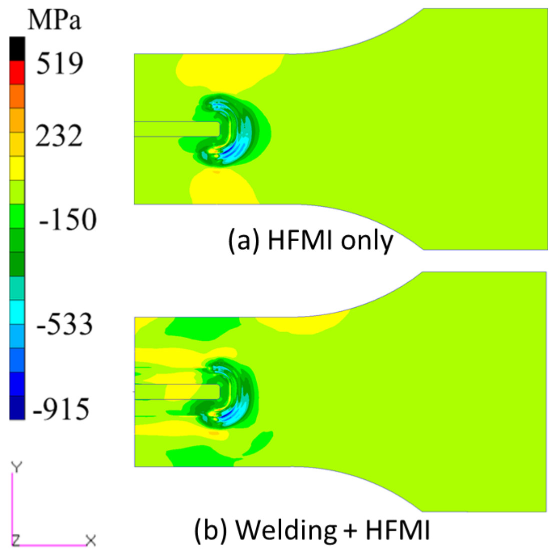

Fig. 5.12 Longitudinal (S_{XX}) residual stress field comparison.

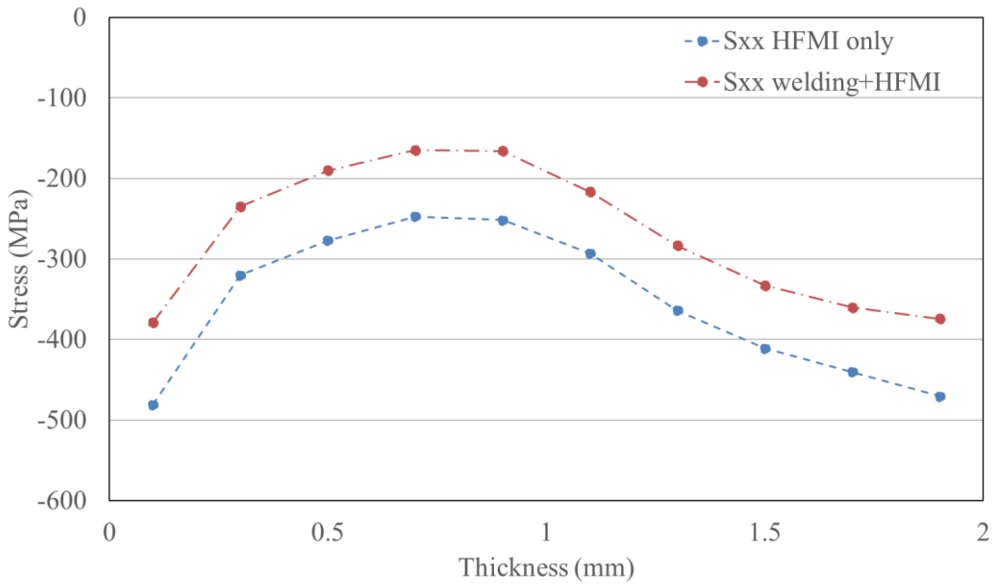

Fig. 5.13 Longitudinal (S_{XX}) residual stress in the thickness direction at the target location.

Next, a comparison of the residual stress before and after HFMI is presented. Fig. 5.14 shows the residual stress field in the Longitudinal (S_{XX}), Transversal (S_{YY}) and Von Mises (VM) stress before and after HFMI. Figure 5.14 (a) and (b) show high compressive stress in the peened region. Fig. 5.14 (c) shows an increment of the Von Mises stress in this region.

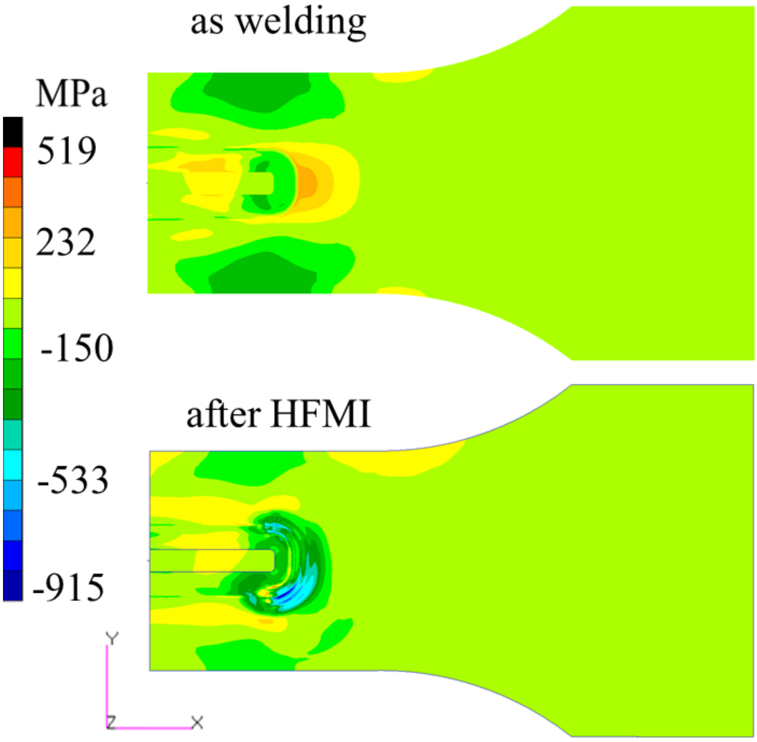

(a) Longitudinal (S_{XX})

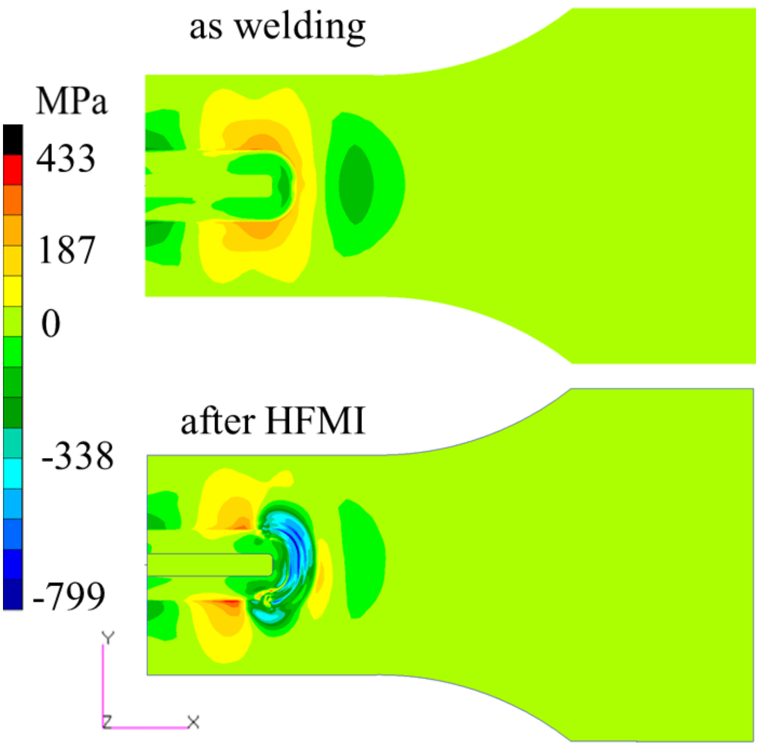

(b) Transversal (S_{YY})

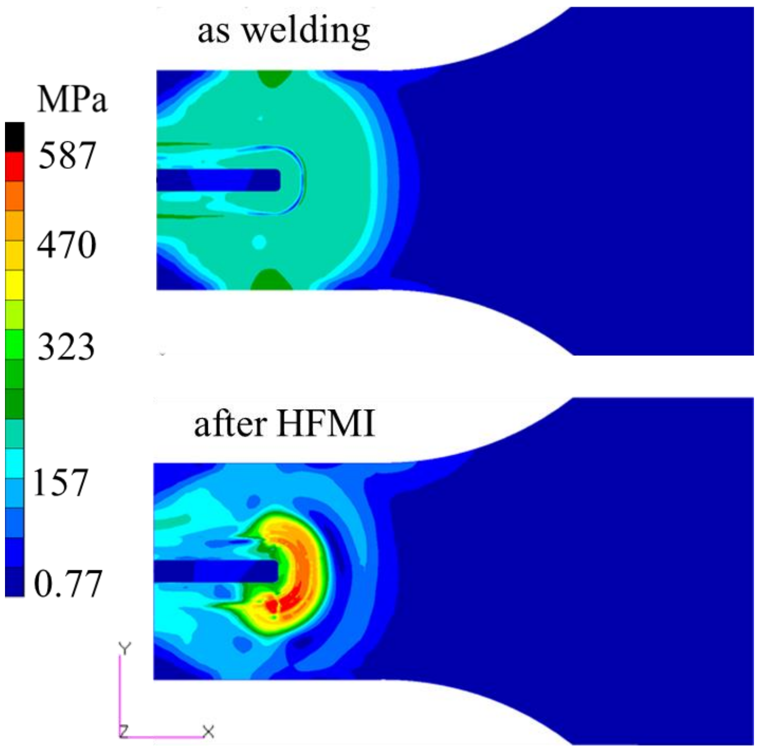

(c) Von Mises (VM)

Fig. 5.14 Residual stress before and after HFMI. **(a)** S_{XX}. **(b)** S_{YY}. **(c)** VM.

Stress profile at the target location before and after HFMI is shown in Fig. 5.15. Fig. 5.15 (a) and (b) show the HFMI-induced high compressive stresses near the top surface. Fig. 5.15 (c) shows the HFMI-induced high Von Mises stress close the contact surface. Comparison of the effective plastic strain is shown in Fig. 5.16, this shows the effective plastic strain increment and distribution in the treated region after HFMI.

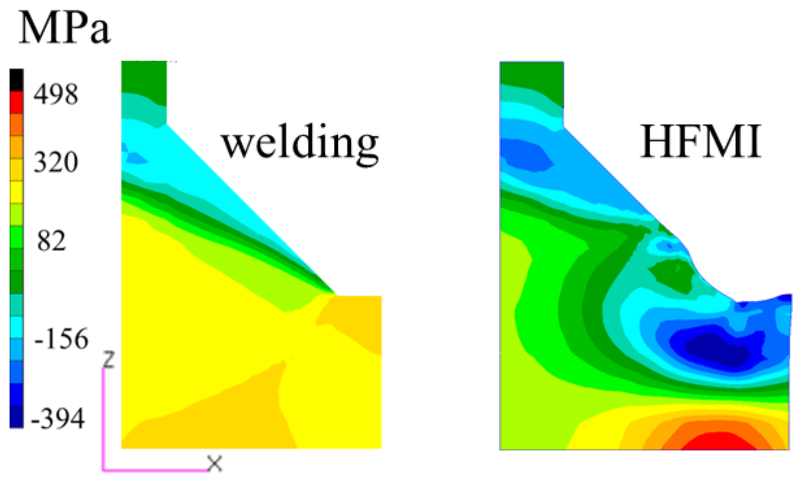

(a) Longitudinal (S_{XX})

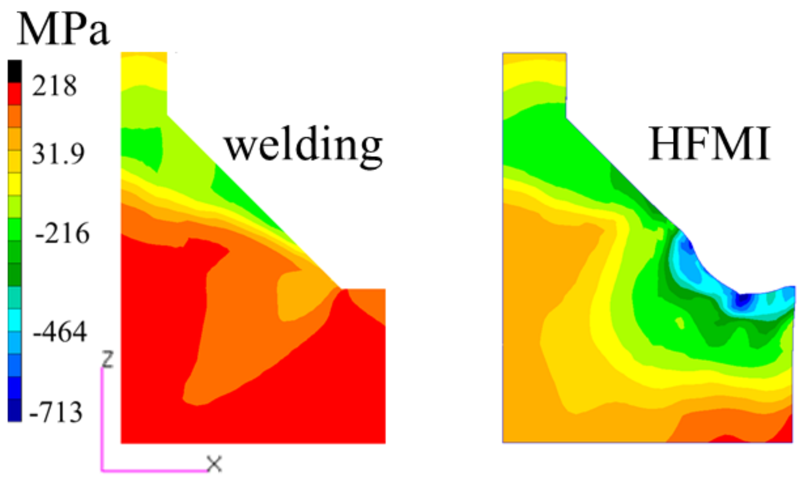

(b) Transversal (S_{YY})

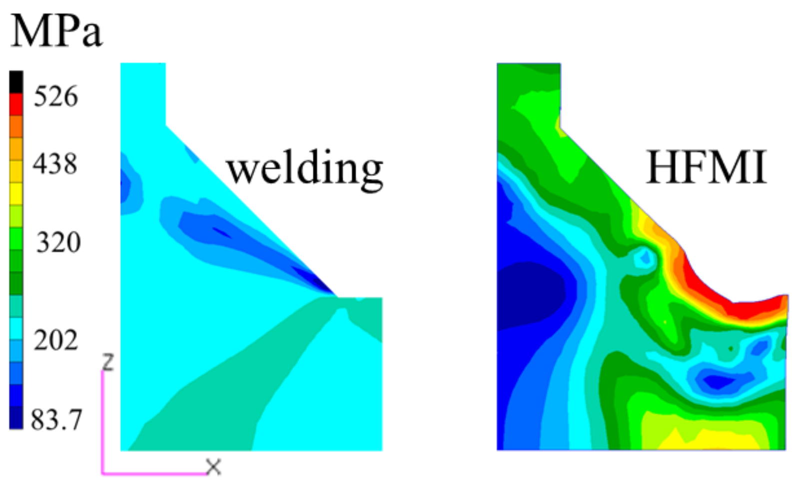

(c) Von Mises (VM)

Fig. 5.15 Residual stress comparison at the target location.

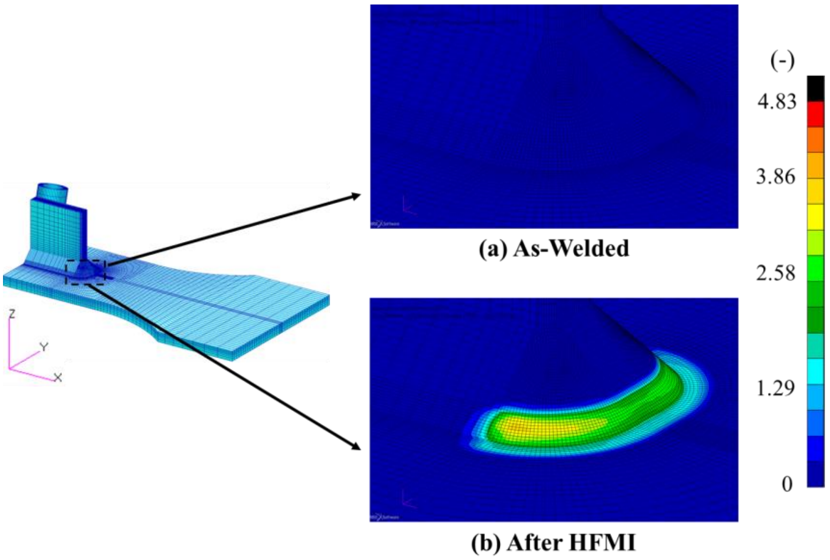

Fig. 5.16 Effective plastic strain comparison.

Figure 5.17 shows a comparison of the three normal stress components and Von Mises stress variation in the thickness direction of the main plate at the target location before and after HFMI. The figure shows high compressive stress, higher than the yield stress, because all components are compressive. Similar stress behavior was observed in [48], where FE-simulation and neutron diffraction stress measurement were used. Furthermore, Von Mises stress increases to the yield stress level with consideration of hardening. Additionally, experimental measurements (S_{XX}) from the literature [66] are presented. It is shown that:

- The expected residual stress behavior is obtained, turning from tensile to compressive.
- Similar trend between measurement and simulation up to about 1.3 mm depth from the surface is observed. despite the different material properties and boundary conditions considered in the simulation.

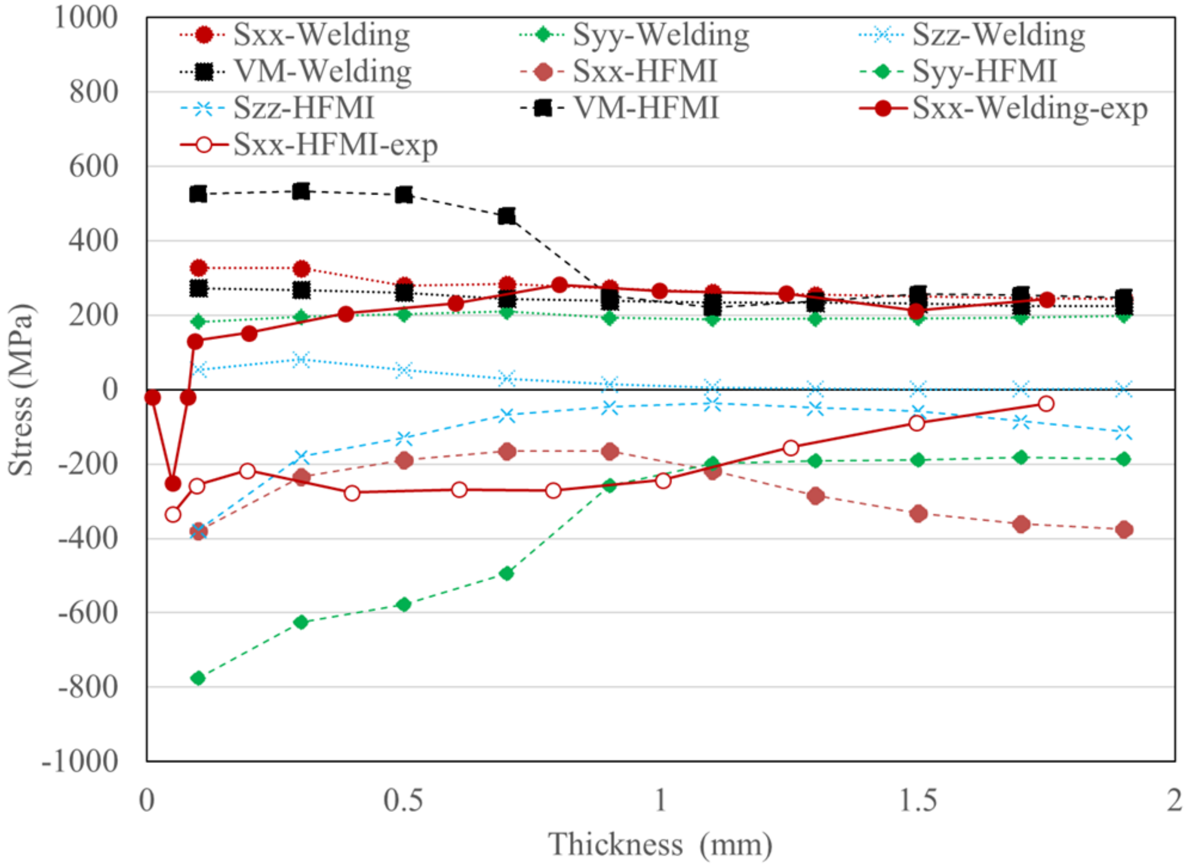

Fig. 5.17 Normal stresses and Von Mises stress before and after HFMI.

Appendix C shows the HFMI induced residual stress in the thickness direction under different boundary conditions. Furthermore, comparison between the simulated residual stress with PNU's results is shown.

5.4 Conclusions

This chapter showed numerical simulation of welding followed by HFMI treatment on an out-of-plane gusset welded joint. The welding process was analyzed using the thermal elastic-plastic FE simulation code JWRIAN. The computed welding residual stresses by JWRIAN were in good agreement with that computed by Abaqus, proving the reliability of the computed residual stresses by JWRIAN. Differences may be caused by different element formulations in the two codes. Furthermore, experimental measurements [66] show similar trend with those numerical results in the middle of the thickness as presented in Fig. 5.8, even though different material and conditions are considered in the numerical simulation.

The experimental compressive welding residual stress [66] near the top surface may be caused by convection between air and the surface of the weld bead. Increase of residual stress from 0.1mm to 0.6mm in the thickness direction may be caused by experimental measurement errors.

Then, the mechanical behavior after HFMI was analyzed by means of dynamic analysis using the explicit commercial code MSC.Dytran. The mechanical behavior in a stress-free model was investigated. Then, the computed results were compared with those obtained after HFMI when welding residual stresses computed by JWRIAN were taken into account. Differences reveal that welding residual stresses can not be neglected when predicting the residual stress after welding and HFMI.

Comparison of the computed mechanical behavior before and after HFMI is presented. This showed the expected residual stress behavior, turning from tensile to compressive. Finally, the experimental measurements (S_{XX}) from the literature showed similar trend near the top surface and up to about 1.3mm depth from the surface, despite the different material properties, boundary conditions and welding residual stress field were used in the HFMI numerical simulation. The computed residual stress field will be used in cyclic loading simulation to investigate the stability of HFMI residual stress under different loading conditions.

Chapter 6 Stability of Residual Stress Field under Cyclic Loading

6.1 Introduction

The objective of this section is to investigate the stability of the residual stress induced by HFMI in the out of plane gusset joint investigated in Chapter 5. First, a study of the effect of frequency on cyclic loading response is considered. Then, the effect of different constant amplitude cyclic loading scenarios on residual stress is analyzed. Finally, the effect of different cyclic loading scenarios with a peak load in the first cycle is investigated.

6.2 Effect of Cyclic Loading Frequency

In order to reduce the computational time during simulation of low-frequency cyclic loading, a higher frequency which does not appreciably affect the response of the target out-of-plane gusset joint is preferable. The joint is stressed by applying a remote cyclic uniform stress in the longitudinal direction (X-dir.) as shown in Fig. 6.1. Three frequencies are considered, 100 Hz, 300 Hz and 600 Hz. Fig. 6.2 shows the constant amplitude load scenario. A maximum nominal stress of +150 MPa and a minimum nominal stress of 0 MPa, with a stress ratio (min. stress/max. stress) of R=0. Five cycles are applied in order to reach a stable stress-strain behavior. The same boundary conditions as that in the HFMI simulation are used, see Fig. 6.1, and strain rate effects are not considered.

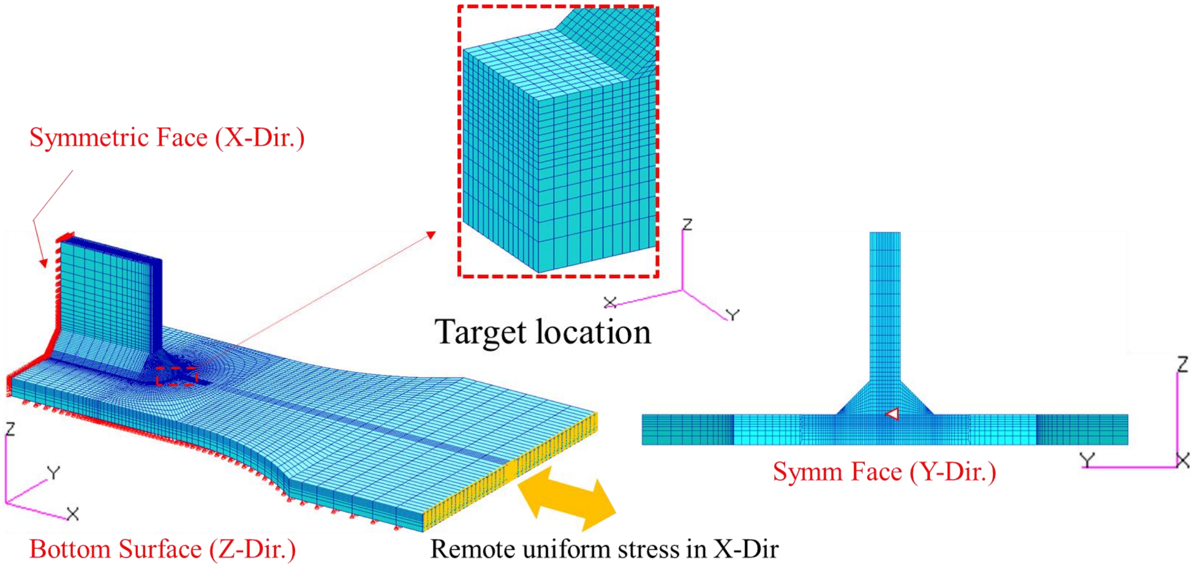

Fig. 6.1 Boundary and cyclic loading conditions.

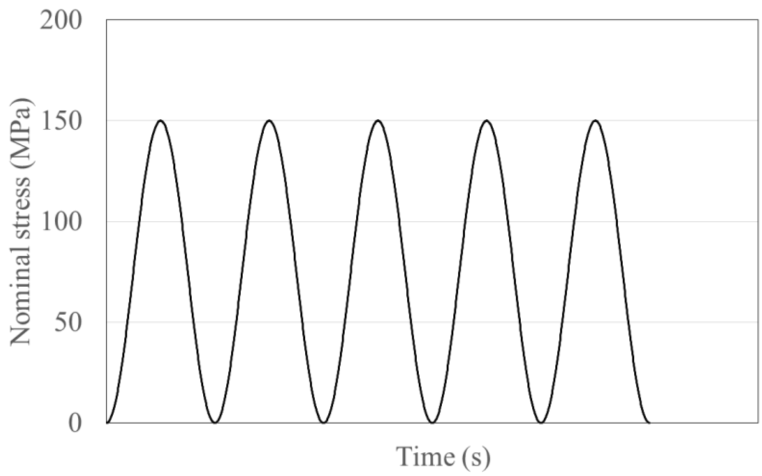

Fig. 6.2 Cyclic loading scenario in the longitudinal direction (X-Dir).

Figure 6.3 shows a comparison of the obtained longitudinal (S_{XX}) stress, transversal (S_{YY}) stress, and effective plastic strain (EFFPLS) distribution in the thickness direction of the main plate at the target location using each frequency. Only negligible differences between stresses and effective plastic strain produced by different frequencies may be observed. This means that if strain rate is not taken into account, different frequencies up to 600 Hz may be used without having an appreciable effect on stresses and strains; and that in the target joint, inertia effects may be neglected up to a frequency of 600 Hz. In this study a frequency of 300 Hz is used.

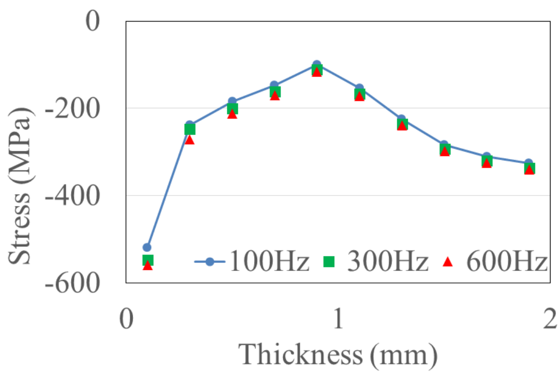

(a) Longitudinal (S_{XX}) stress

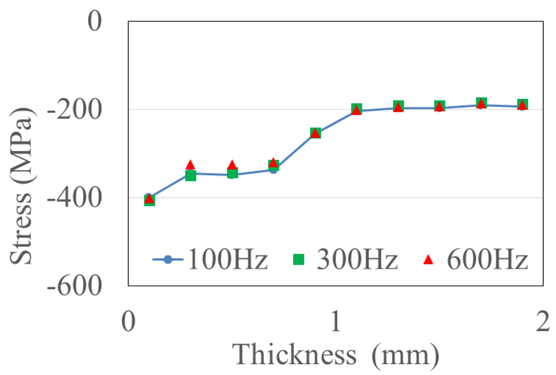

(b) Transversal (S_{YY}) stress

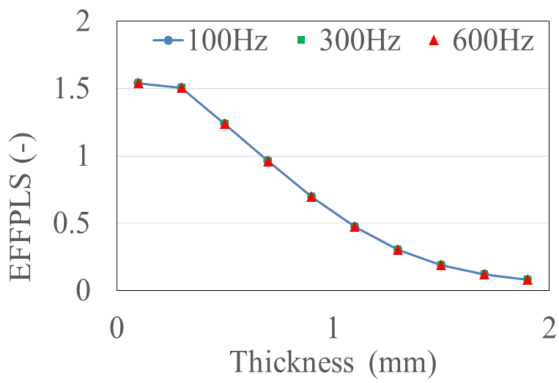

(c) Effective Plastic Strain (EFFPLS)

Fig. 6.3 Mechanical behavior under different frequencies.

Finally, Fig. 6.4 shows the longitudinal (S_{XX}) residual stress time history in an element on the top surface at the target location. This shows that residual stress variation is stable after the first cycle. Therefore, three cycles will be used for further simulation. Maximum and minimum stress of each cycle for other components at the target location are shown in appendix E.

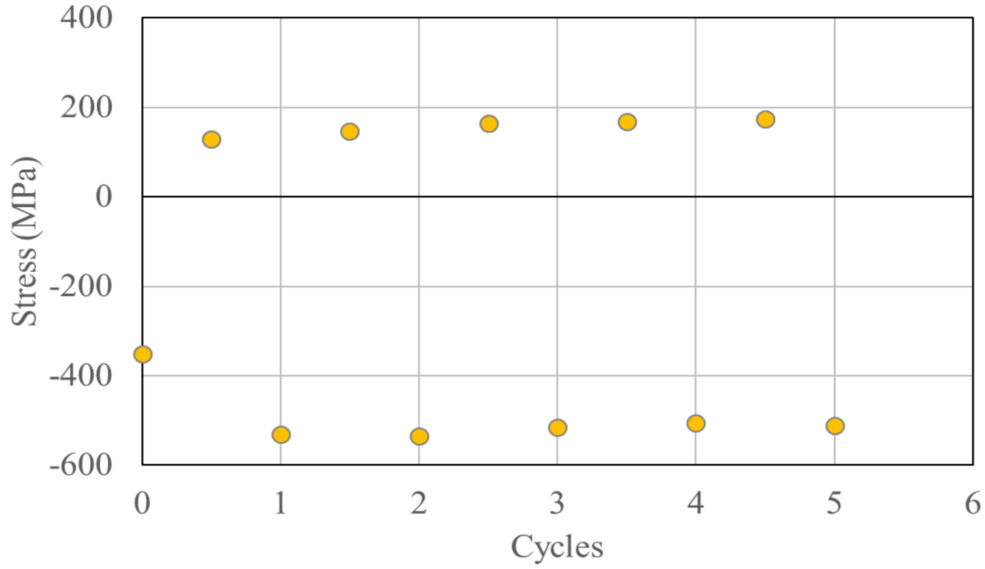

Fig.6.4 Maximum and minimum Longitudinal (S_{XX}) stress of each cycle at the target location.

6.3 Constant Amplitude Loading

Cyclic loading simulation is carried out to investigate the stability of the residual stress field at the target location under different constant amplitude loading scenarios. These loading scenarios are applied to the out of plane gusset welded joint, assuming three different residual stress fields: stress-free, welding residual stress, and welding and HFMI residual stress. Boundary conditions are shown in Fig. 6.1.

6.3.1 Cyclic Loading Scenarios

Figure 6.5 shows three constant amplitude cyclic loading with a maximum nominal stress of +50 MPa, +75 MPa, and +150 MPa respectively. A minimum nominal stress of 0 MPa, with a stress ratio (min. stress/max. stress) of R=0. The load is applied as remote uniform stress in X-direction, see Fig. 6.1. Three cycles are applied in order to reach a stable stress-strain behavior, as was found enough in previous section.

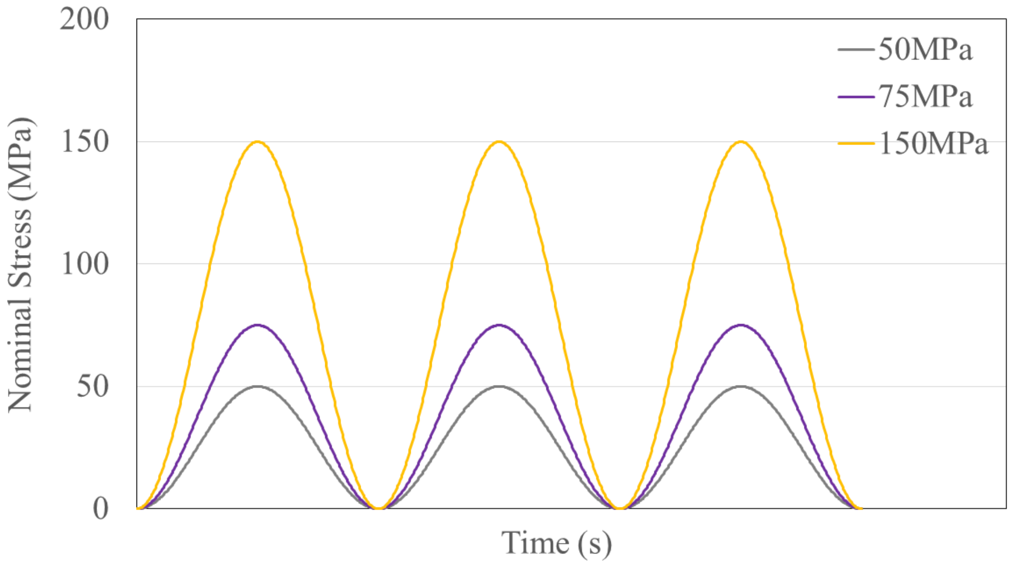

Fig. 6.5 Constant Amplitude loading scenarios.

6.3.2 Stress-Free Out-of-Plane Gusset Joint

In order to determine the minimum nominal stress which produces plasticity during cyclic loading, a stress-free welded joint model is used to investigate the stress behavior using the cyclic loading scenarios shown in Fig. 6.5.

Figure 6.6 shows the effective plastic strain (EFFPLS) time history, longitudinal (S_{XX}) residual stress and transversal (S_{YY}) residual stress of an element on the top surface at the target location. This shows that +50 MPa and +75 MPa do not induce plastic strain. However, a maximum stress of +150 MPa induces tensile plastic strain as shown in Fig. 6.6 (a). Then once the load is released, the produced tensile plastic strain at the target location causes additional elastic compressive strain and compressive stress arises at the target location, see Fig. 6.6 (b, c). However, plastic strain does not increase after the first cycle. Maximum and minimum stresses at the target location are also stable after the first cycle. Appendix F shows the stress/strain relationship of the analyzed element under constant amplitude loading scenario shown in Fig. 6.5.

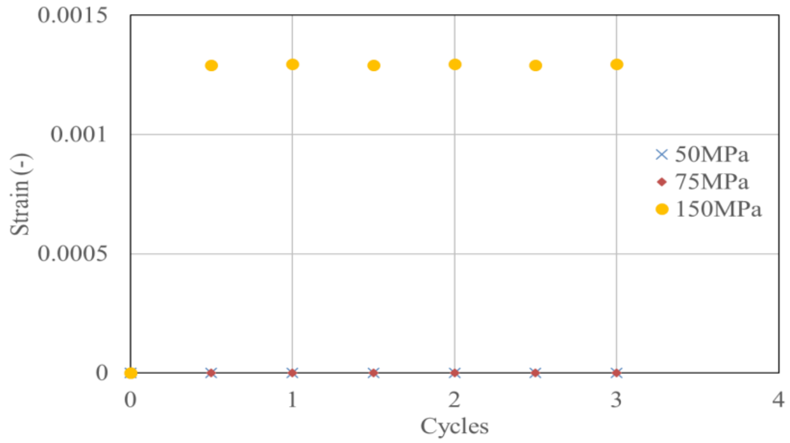

(a) Effective plastic strain (EFFPLS)

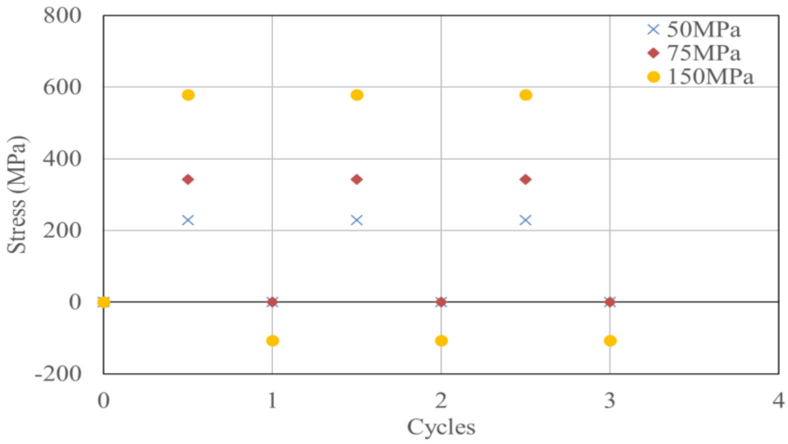

(b) Longitudinal (S_{XX}) stress

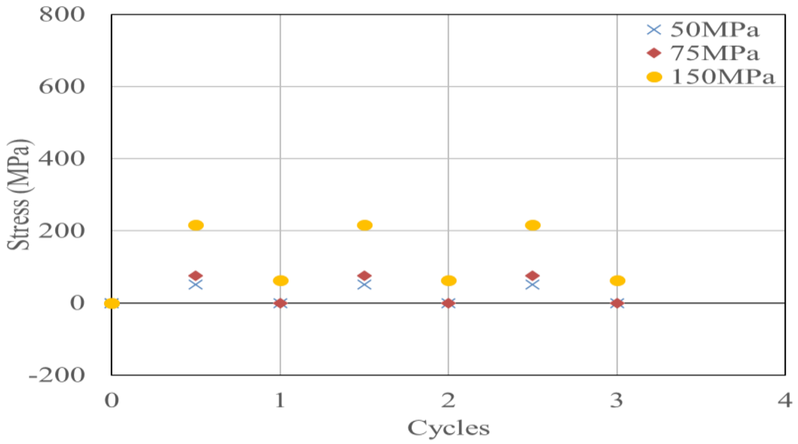

(c) Transversal (S_{YY}) stress

Fig. 6.6 Mechanical behavior under different cyclic loading scenarios.

6.3.3 Out-of-Plane Gusset Welded Joint Considering Welding Residual Stress

In this section, effect of cyclic loading on the residual stress induced by welding is investigated for a better understanding of the stress field without HFMI. Figure 6.7 (a) and (b) show a comparison between the obtained welding residual stresses by JWRIAN with those after cyclic loading without HFMI. Only constant amplitude loading with a maximum nominal stress of +75 MPa and +150 MPa are considered in this comparison. This comparison shows that tensile welding residual stress is reduced after applying cyclic loading. Higher nominal stress of +150 MPa shows more relaxation, turning the longitudinal (S_{XX}) residual stress at the target location from tensile to compressive. This behavior agrees with the result showed on a stress-free model in Fig. 6.6 (b). The comparison of the longitudinal (S_{XX}) residual stress on the top surface between welding residual stress and the obtained residual stress after cyclic loading is shown in Fig. 6.8. Appendix G shows the stress distribution with constant amplitude loading under a maximum stress of +50 MPa.

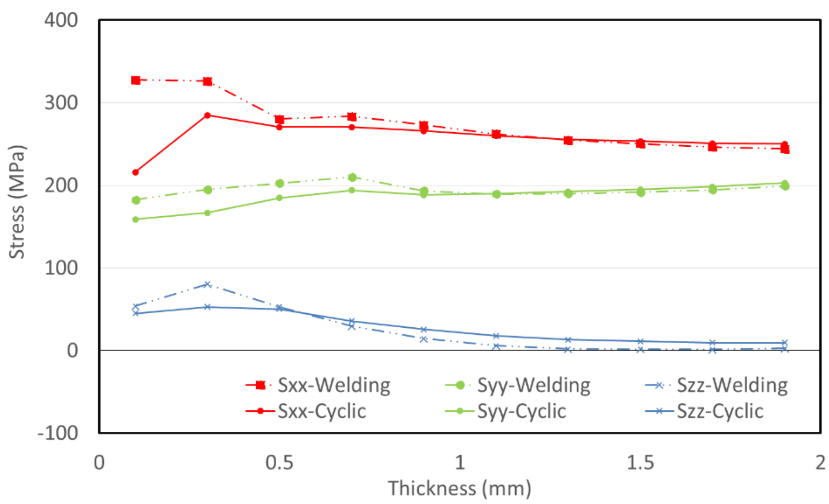

(a) Constant amplitude loading with maximum stress of +75 MPa.

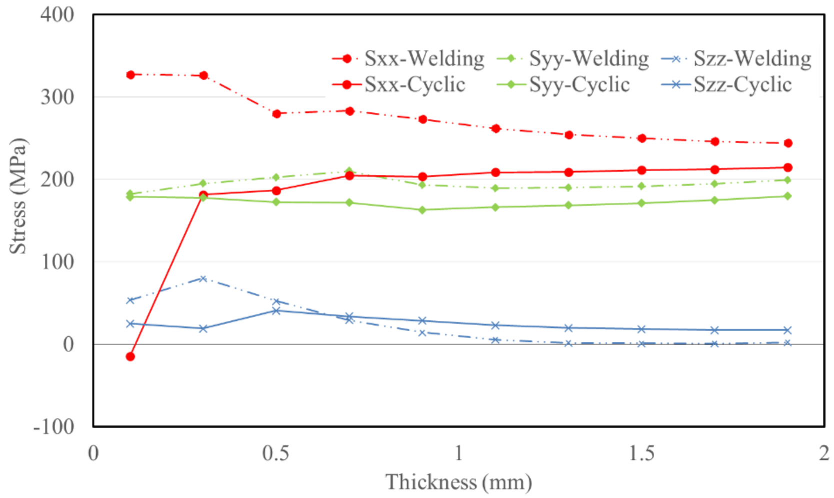

(b) Constant amplitude loading with maximum stress of +150 MPa.

Fig. 6.7 Comparison between residual stress at the target location after welding and after welding + cyclic loading.

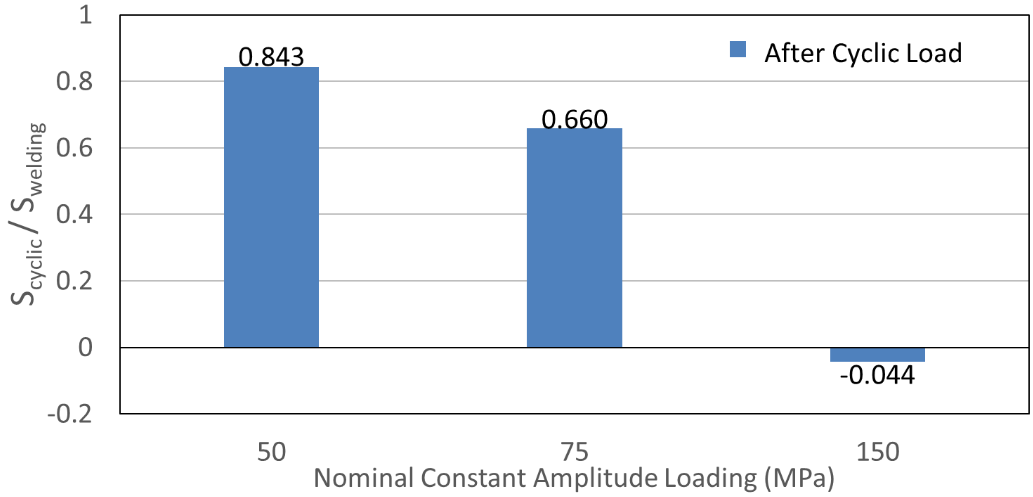

Fig.6.8 Comparison of welding longitudinal (S_{XX}) residual stress with the obtained longitudinal residual stress on the top surface after cyclic loading.

6.3.4 Effect of Cyclic Loading on HFMI Residual Stress

Figure 6.9 shows the residual stress distribution in the thickness direction of the main plate at the target location after HFMI and after cyclic loading. Fig. 6.10 shows a comparison of the HFMI and after cyclic loading induced residual stress on the top surface. Fig. 6.11 shows a comparison of the induced strain. The following may be observed:

Longitudinal (S_{XX}) residual stress

Constant amplitude loading with a maximum nominal stress of +50 MPa and +75 MPa, have a negligible effect on the residual stresses induced by HFMI. On the other hand, a maximum nominal stress of +150 MPa causes the compressive stress on the top surface to increase. However, only negligible differences are observed at depth larger than 0.2 mm. The longitudinal (S_{XX}) residual tress comparison on the top surface is shown in Fig. 6.10, this figure shows that the applied tensile constant amplitude loading introduces compressive (S_{XX}) residual stress on the top surface, getting an increment of about 44.5% with +150 MPa.

Transversal (S_{YY}) residual stress

Relaxation of the compressive residual stress induced by HFMI is observed up to a depth of about 1 mm when applying each load scenario. This is because tensile residual stress is induced in the transversal (Y-dir.) direction at the target location under the chosen conditions, see Fig. 6.6c.

Out of plane (S_{ZZ}) residual stress

The applied load scenario has a small influence on the out of plane residual stress.

Von Mises (VM) residual stress

Each load scenario deteriorates Von Mises residual stress field up to about 1 mm in the thickness direction.

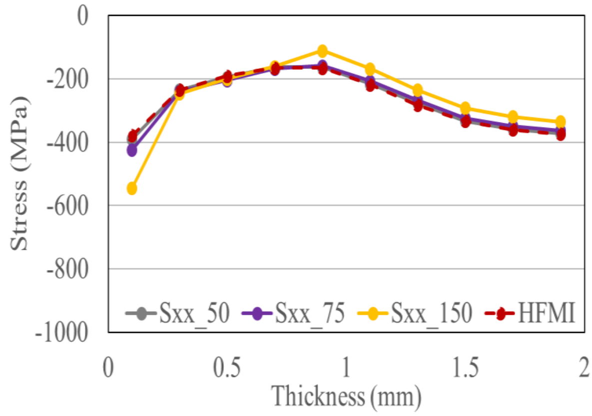

(a) Longitudinal (S_{XX}) stress

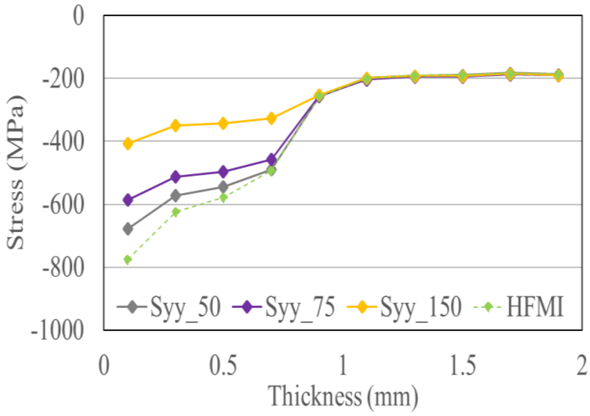

(b) Transversal (S_{YY}) stress

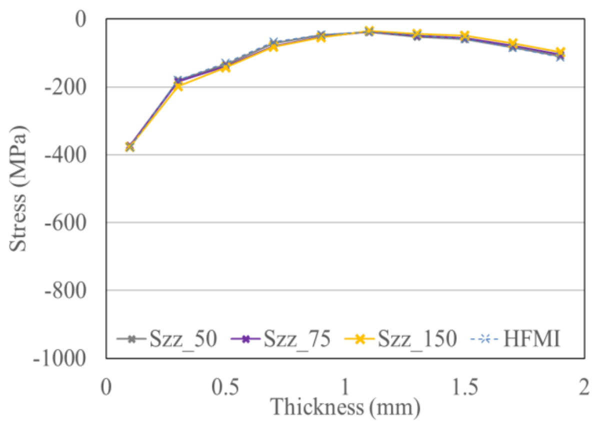

(c) Out of plane (S_{ZZ}) stress

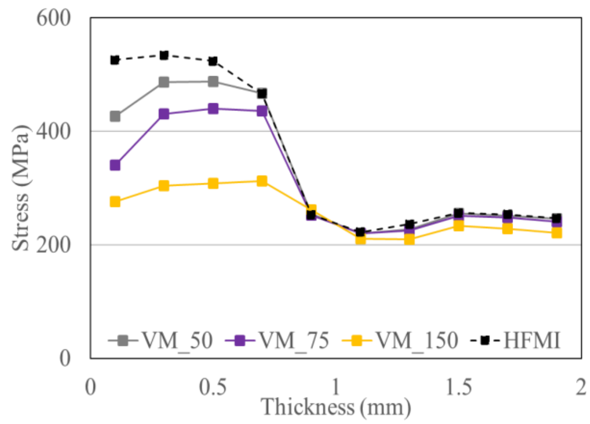

(d) Von Mises (VM) stress

Fig. 6.9 Residual stress comparison in the thickness direction.

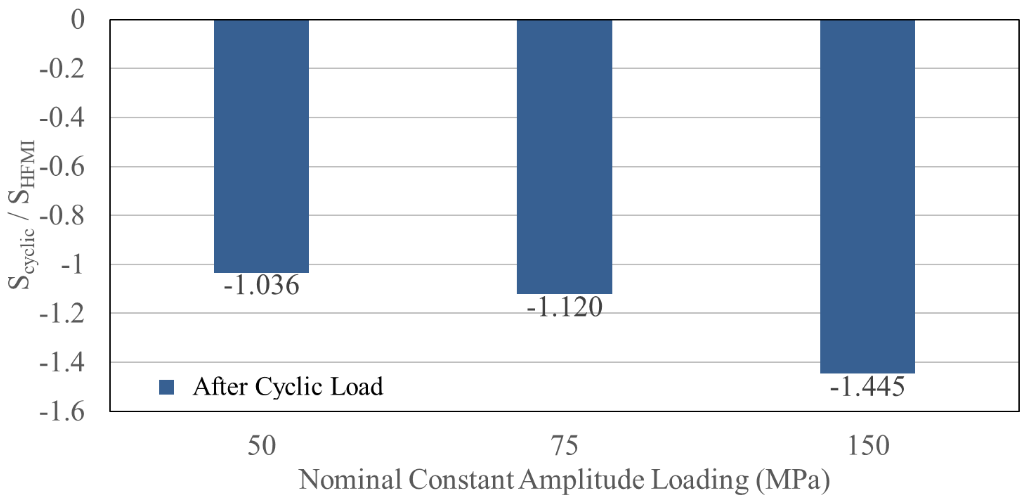

Fig. 6.10 Comparison of longitudinal (S_{XX}) residual stress on the top surface after HFMI with that after constant amplitude loading.

Strain Comparison

Figure 6.11 (a) shows an increase of the effective plastic strain when applying each cyclic loading scenario. A maximum nominal stress of +50 MPa increases the plastic strain by about 0.03%, +75 MPa by about 0.07%, and +150 MPa by about 0.2%. This is because of the re-distribution of the induced residual stress by welding and HFMI around the target location. This increase occurs only in the first cycle.

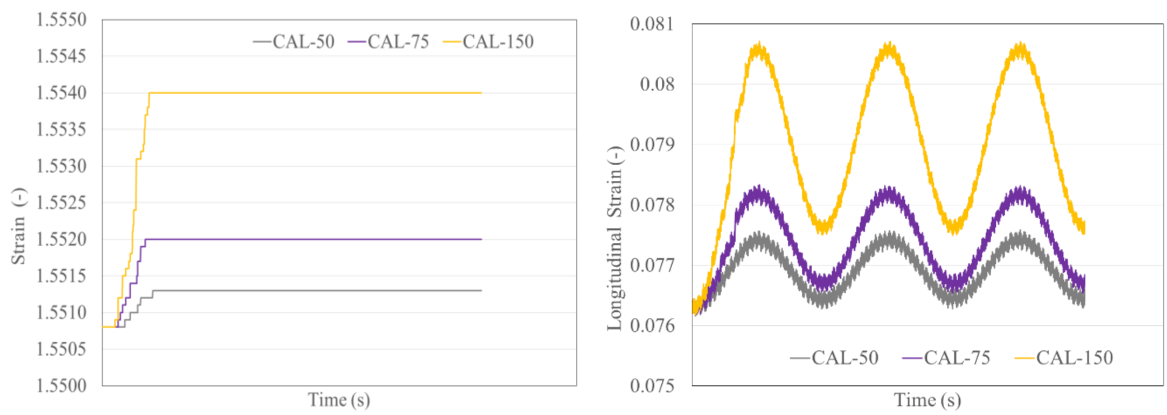

(a) Effective plastic strain (EFFPLS) **(b)** Longitudinal strain (EPS_{XX})

Fig. 6.11 Strain comparison after each cycle.

6.4 Cyclic Loading with Peak Load

In this section, the effect of different cyclic load scenarios with a peak load in the first cycle is investigated. The load is applied as a remote uniform stress in X-direction. Boundary conditions are shown in Fig. 6.1.

Since relaxation is more significant during a compressive peak [63, 65, 92, 93], the simulation is focused on the effect of compressive peak loads, S_{min}. Considering yielding at the target location, S_{min} in term of nominal stress is define as in Eqs 6.1.

$$S_{min} * \boldsymbol{k_t} = \boldsymbol{k} * \sigma_Y \tag{6.1}$$

Where, $\mathbf{k}_t$ is the stress concentration factor of 1.6, σ_Y is yield stress of 355MPa, and $\boldsymbol{k}$ is the peak load factor (k=0.75, 1, 1.25, and 1.36).

After each peak load cycle, a constant amplitude cyclic loading with a maximum nominal stress of +50 MPa, +75 MPa or +150 MPa is applied.

6.4.1 Cyclic Loading Scenarios

Fig. 6.12 shows the four load scenarios. The selected load scenarios were inspired by [63, 65].

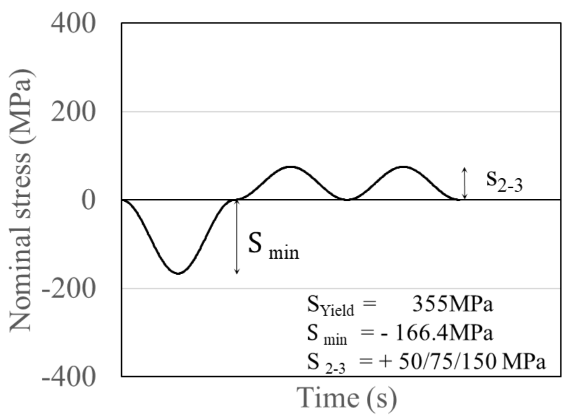

Scenario	Max. Nominal stress (S_{min})	Min. Nominal stress	Max. Nominal stress (CA-loading) (S_{2-3})	Min. Nominal stress (CA-loading)
1	-166.4 MPa	0	50, 75, 150 MPa	0
2	-221.8 MPa	0	50, 75, 150 MPa	0
3	-277.3 MPa	0	50, 75, 150 MPa	0
4	-301.7 MPa	0	50, 75, 150 MPa	0

Fig. 6.12 Conditions of cyclic loading with peak load.

6.4.2 Effect of Peak Load on Residual Stress Relaxation

6.4.2.1 Residual stress comparison under compressive peak load

Figure 6.13 shows a stress comparison after compressive peak load shown in Fig. 6.12. The following may be observed:

Longitudinal (S_{XX}) Stress

Considerable residual stress relaxation near the top surface under all compressive peak load scenarios is obtained. Minimum stress relaxation near the top surface with compressive peak load of S_{min}=-166.4 MPa (about 65%) and maximum with compressive peak load of S_{min}=-301.7 MPa (about 104%). Also relaxation in the thickness direction is observed.

Transversal (S_{YY}) Stress

Relaxation is observed with each compressive peak load. Getting a minimum relaxation of about 24% (from -774 MPa to -585 MPa) near the top surface with a compressive peak load of S_{min}=-166.4 MPa.

Out of Plane (S_{ZZ}) Stress

Negligible changes near the top surface are obtained. However, considerable relaxation in the thickness direction is observed.

Von Mises (VM) stress

Relaxation through the thickness direction is observed. Getting a minimum relaxation of about 18% (from 525 MPa to 420 MPa) near the top surface with a compressive peak load of S_{min}=-166.4 MPa.

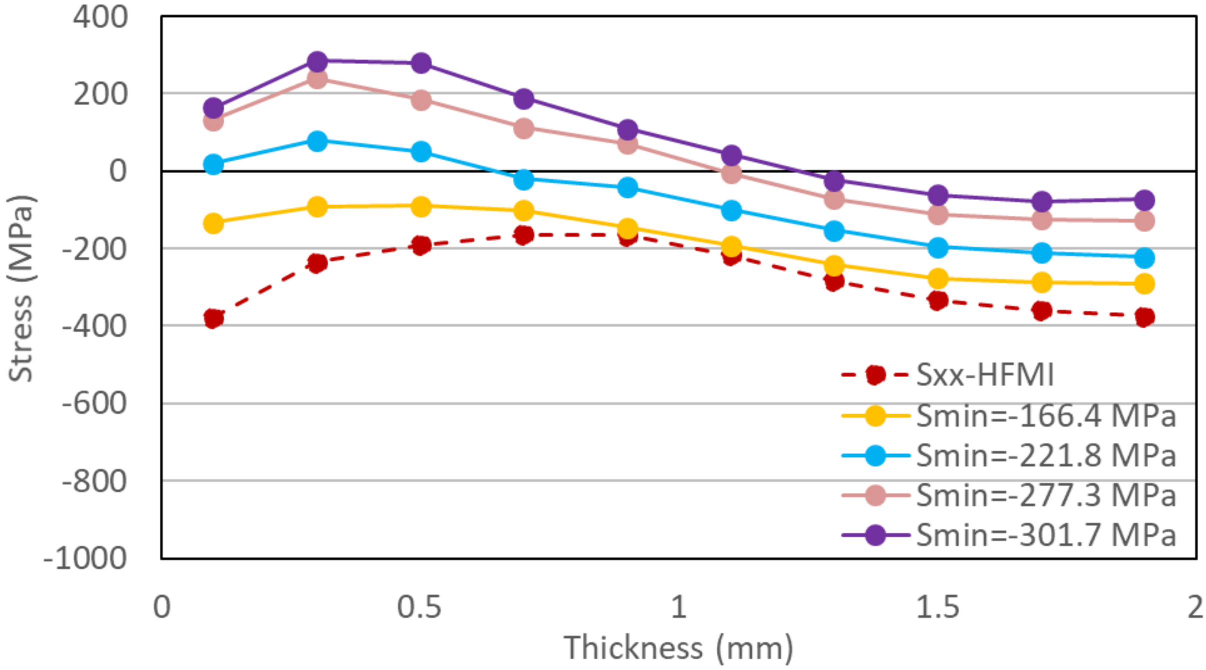

(a) Longitudinal (S_{XX}) stress.

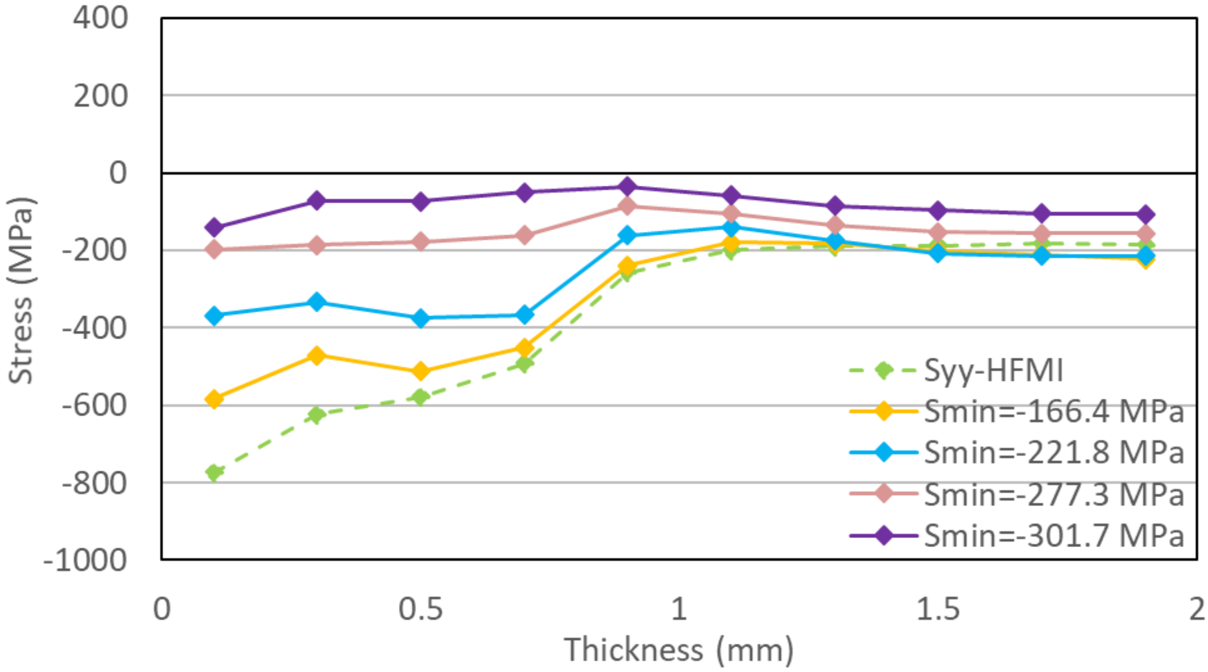

(b) Transversal (S_{YY}) stress.

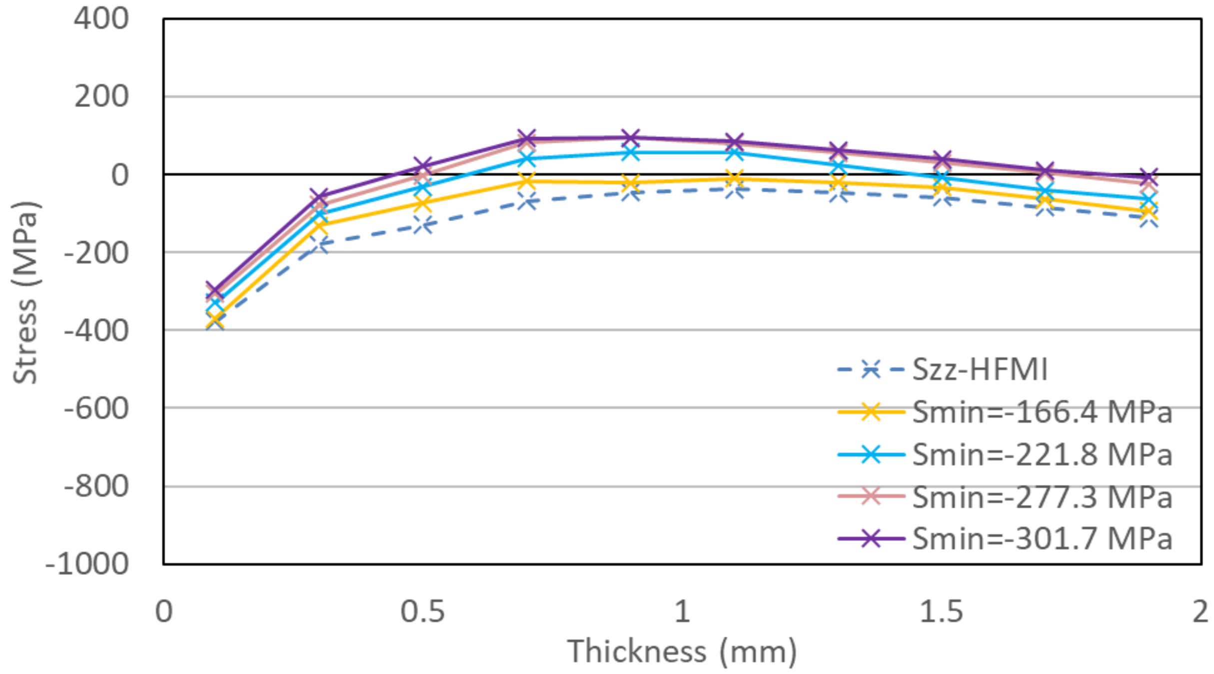

(c) Out of plane (S_{ZZ}) stress.

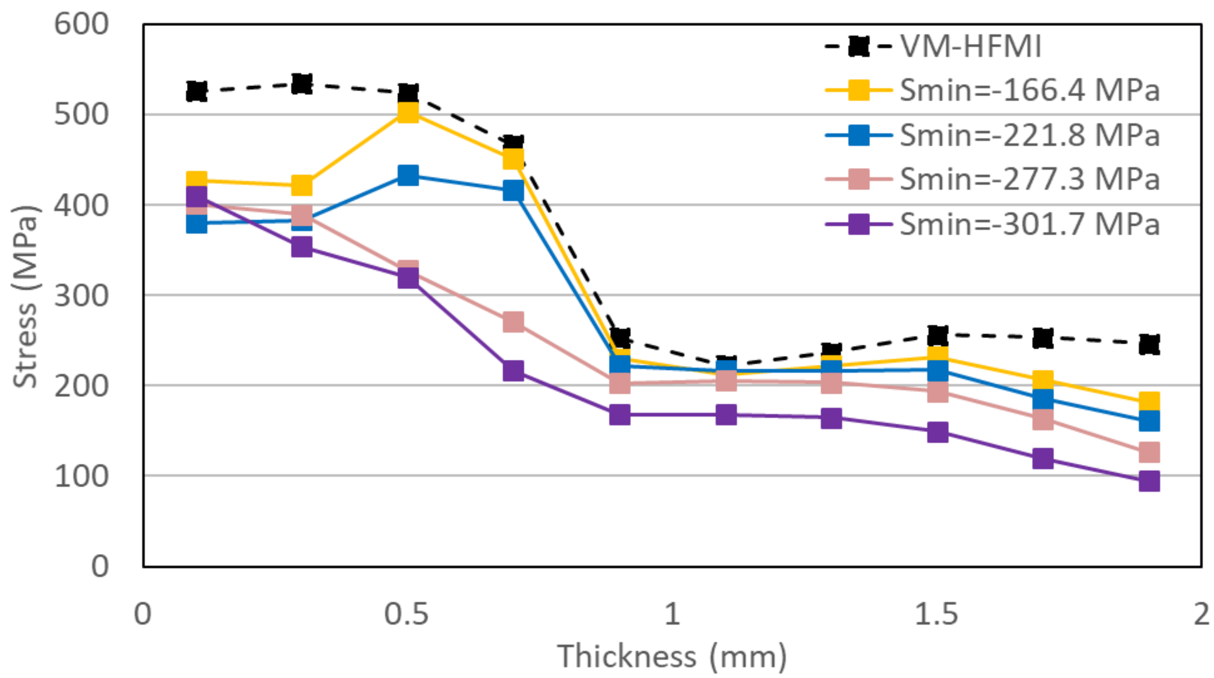

(d) Von Mises (VM) stress.

Fig. 6.13 Residual stress comparison before and after compressive peak loads.

6.4.2.2 Peak load with constant amplitude loading of +50 MPa

Fig. 6. 14 shows a stress comparison under the cyclic loading scenarios shown in Fig. 6.12 with a maximum nominal stress of +50 MPa during the constant amplitude loading.

Longitudinal (S_{XX}) Stress

Relaxation in the longitudinal residual stress is observed for each cyclic peak loading scenario. Getting tensile stress up to a depth of about 1.3 mm when a S_{min}=-301.7 MPa is applied. This demonstrates that a maximum nominal stress of +50 MPa does not has any benefit in the stability of compressive residual stresses.

Transversal (S_{YY}) Stress

Relaxation of the stresses are comparable to those obtained with a maximum stress of +75 MPa during the constant amplitude load.

Out of Plane (S_{ZZ}) Stress

Considerable stress relaxation of about 21% (-377 MPa to -304 MPa) near the top surface with a S_{min}=-301.7 MPa. Furthermore, considerable relaxation in the thickness direction may be observed.

Von Mises (VM)

Similar relaxation near the top surface may be observed. However, relaxation is decreased in the thickness direction when compared with previous cases.

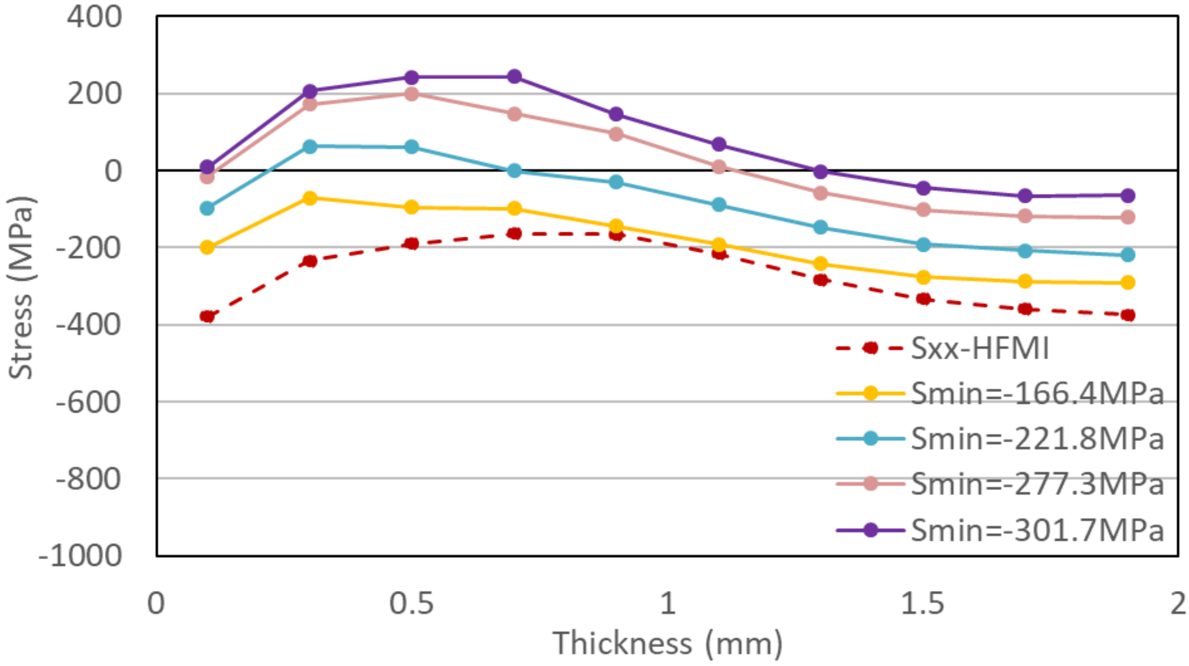

(a) Longitudinal (S_{XX}) stress.

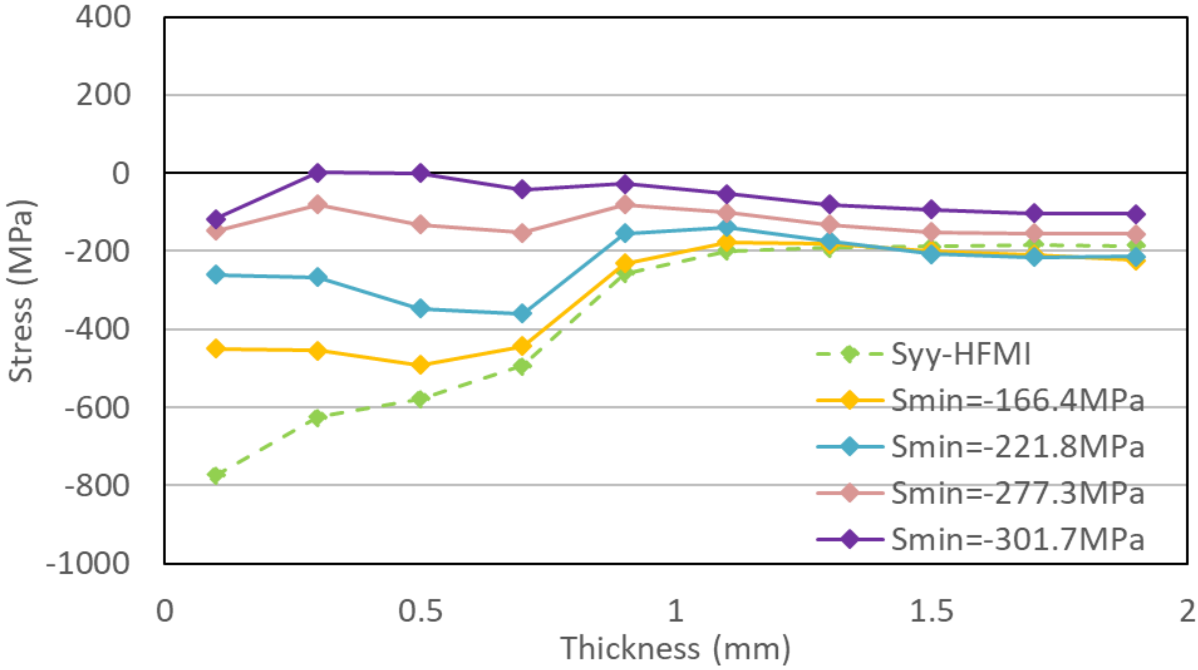

(b) Transversal (S_{YY}) stress.

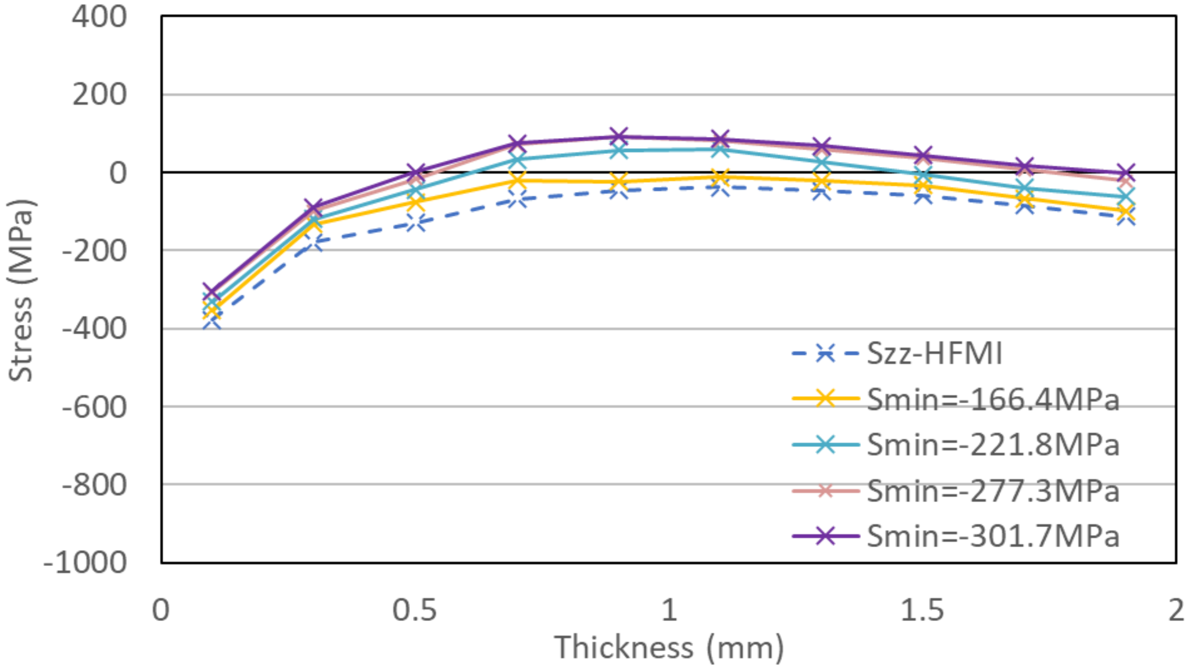

(c) Out of plane (S_{ZZ}) stress.

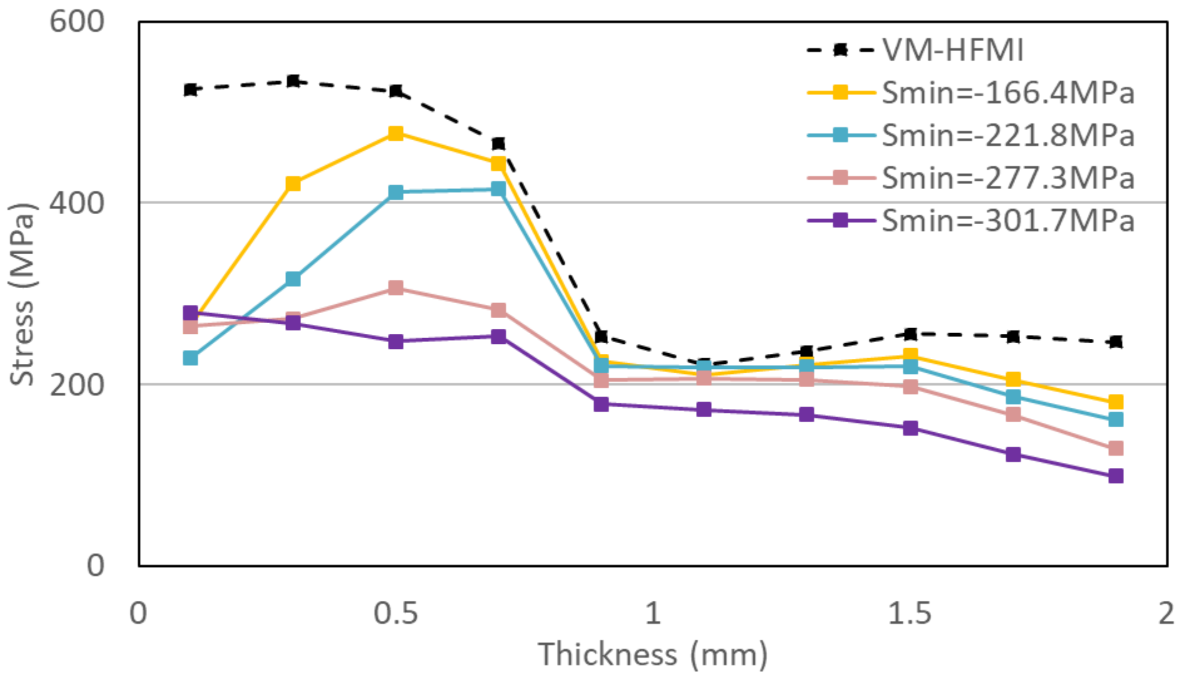

(d) Von Mises (VM) stress.

Fig. 6.14 Residual stress comparison under peak load with constant amplitude of + 50 MPa.

6.4.2.3 Peak load with constant amplitude loading of +75 MPa

Fig. 6. 15 shows a stress comparison under the cyclic loading scenarios shown in Fig. 6.12 with a maximum nominal stress of +75 MPa during the constant amplitude loading.

Longitudinal (S_{XX}) Stress

Stress relaxation with each cyclic loading scenario is obtained. Near the top surface, the minimum relaxation is obtained with S_{min}=-166.4 MPa, of around 39% (-352 MPa to -254 MPa), and the maximum relaxation is obtained with Smin=-301.7 MPa, of around 135% (-352 MPa to -73 MPa).

Transversal (S_{YY}) Stress

High relaxation is observed with each cyclic loading scenario. A minimum relaxation of around 66% (-774 MPa to -387 MPa). Comparing with the obtained stress when applying a peak load followed by constant amplitude loading with a maximum stress of +150 MPa the relaxation is decreased about 40%.

Out of Plane (S_{ZZ}) Stress

Negligible changes in the thickness direction are obtained.

Von Mises (VM)

Comparable stress relaxation near the top surface with those showed in Fig. 6.12 (d) may be observed. However, less relaxation is obtained in the thickness direction.

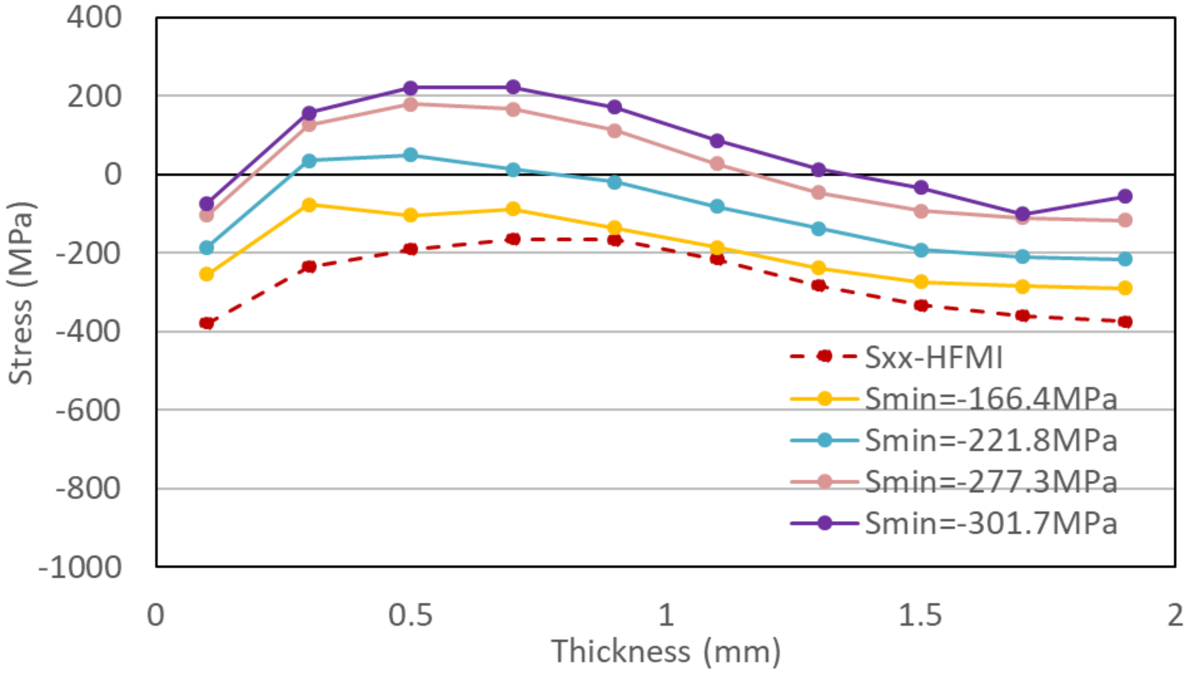

(a) Longitudinal (S_{XX}) stress.

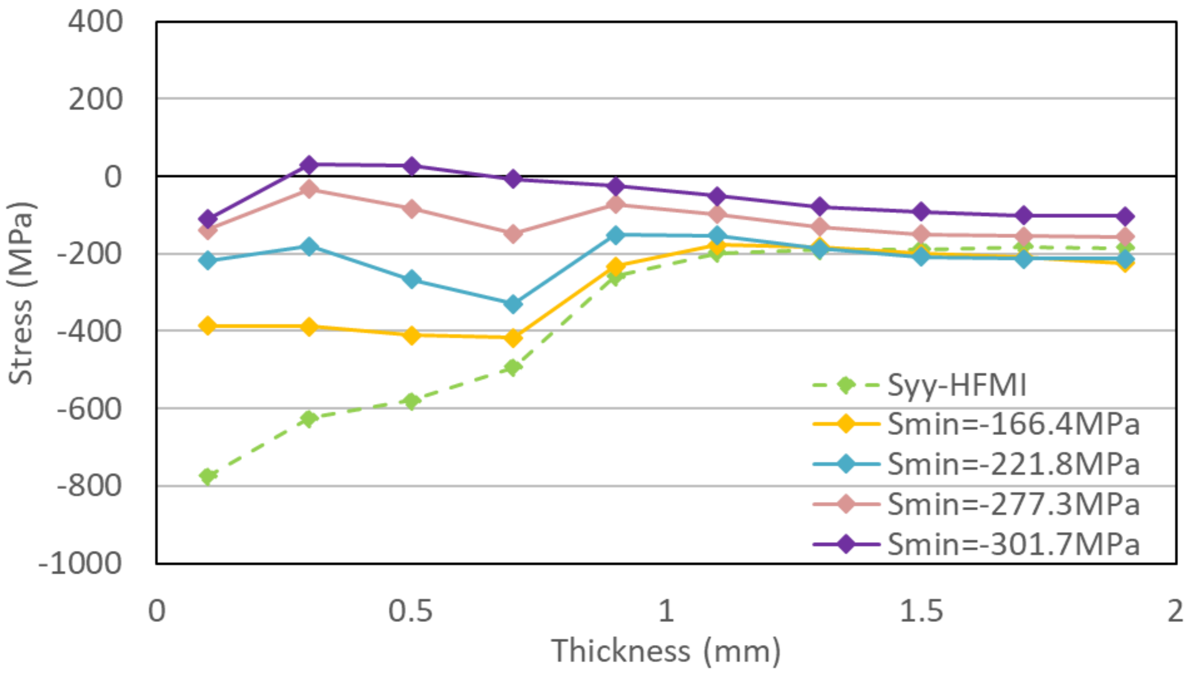

(b) Transversal (S_{YY}) stress.

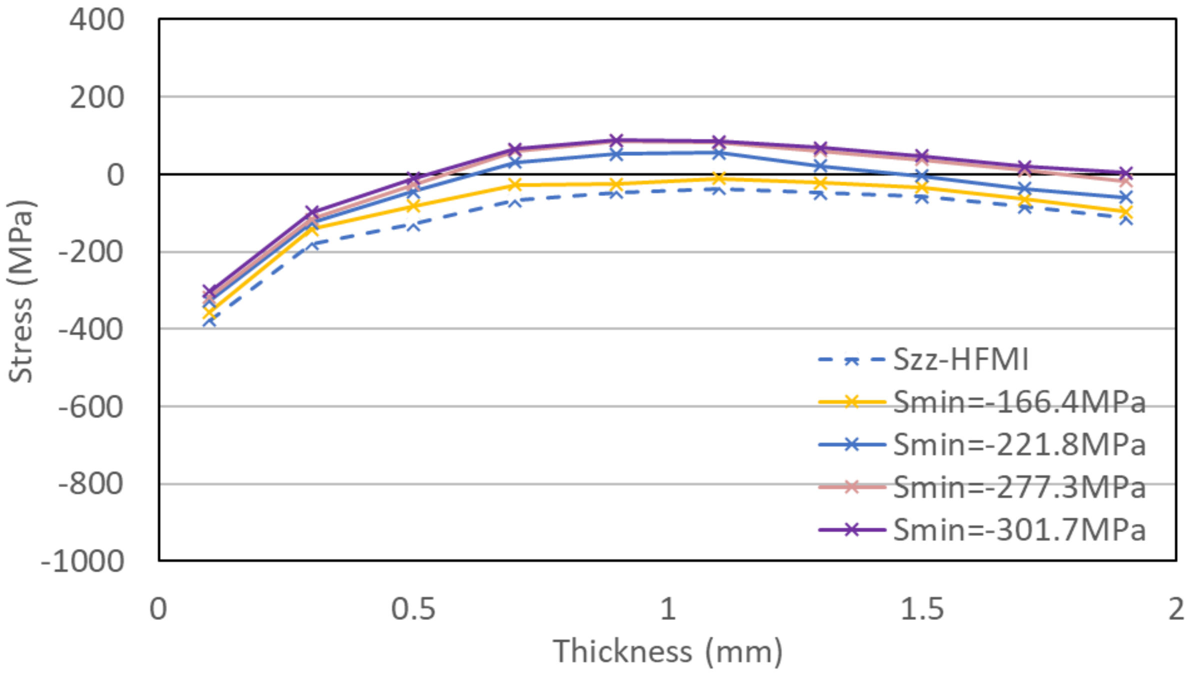

(c) Out of plane (S_{ZZ}) stress.

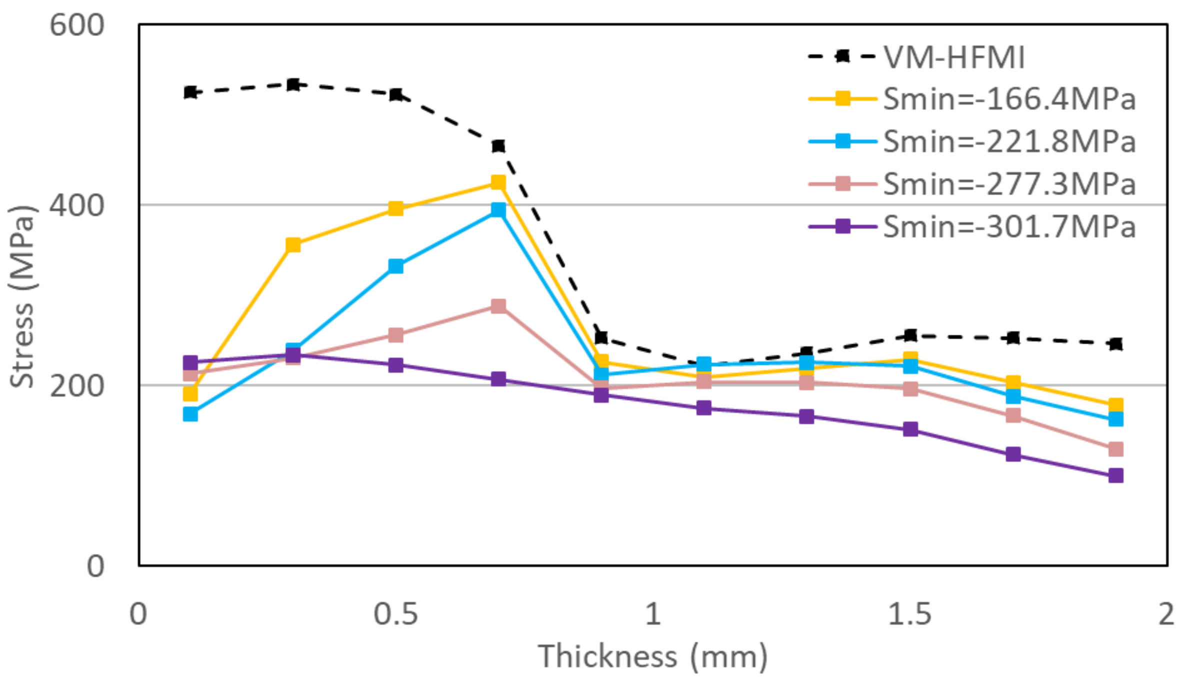

(d) Von Mises (VM) stress.

Fig. 6.15 Residual stress comparison under peak load with constant amplitude of + 75 MPa.

6.4.2.4 Peak load with constant amplitude loading of +150 MPa

Figure 6.16 shows a stress comparison under the cyclic loading scenarios shown in Fig. 6.12. Appendix H shows the maximum and minimum stress and strain of each cycle when peak load with constant amplitude loading of +150 MPa is applied.

The following may be observed:

Longitudinal (S_{XX}) Stress

Even though high compressive peak values are induced in the longitudinal direction (X-Dir), negligible changes near the top surface are obtained. However, slight relaxation deeper below the surface is observed. On the other hand, compressive stress is induced near the top surface with compressive peak loads of S_{min}=-166.4 MPa (about 21%) and S_{min}=-221.8MPa (about 10%).

Transversal (S_{YY}) Stress

High relaxation is observed with each cyclic loading scenario. Getting a minimum relaxation of about 103% (-774 MPa to -256 MPa) near the top surface with a minimum peak load of S_{min}=-166.4 MPa.

Out of Plane (S_{ZZ}) Stress

Negligible changes in the thickness direction are obtained.

Von Mises (VM)

High relaxation up to a depth of about 1 mm is observed. Relaxation of about 70% (525 MPa to 240 MPa) near the top surface is obtained.

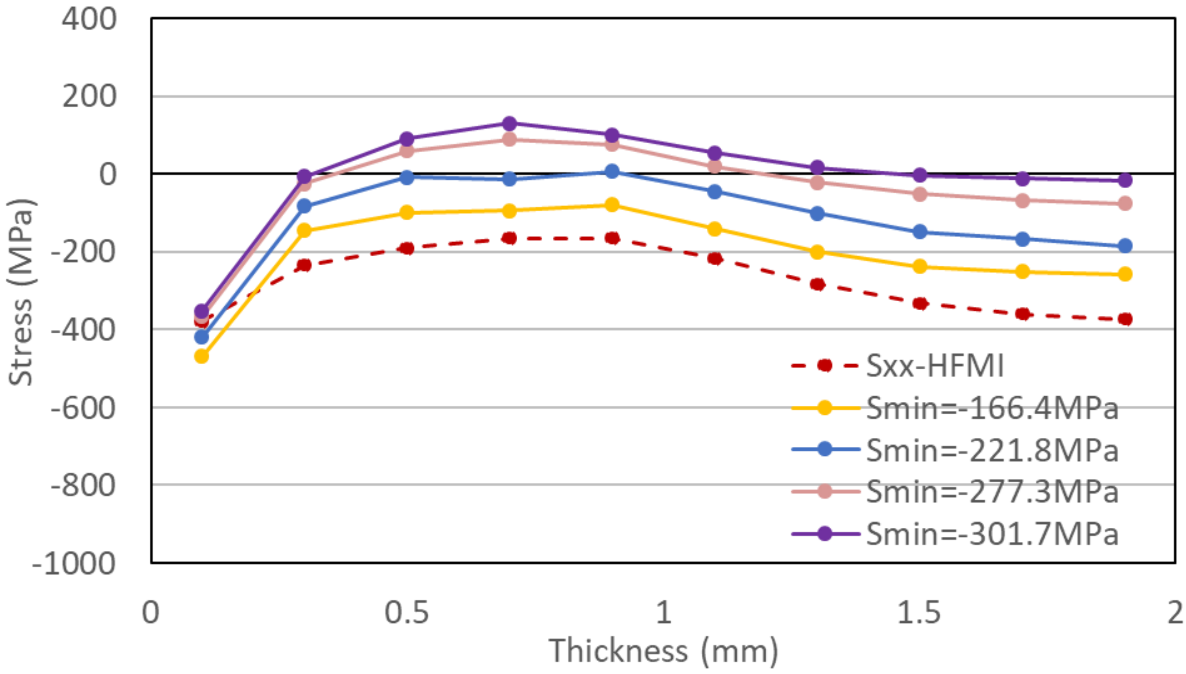

(a) Longitudinal (S_{XX}) stress.

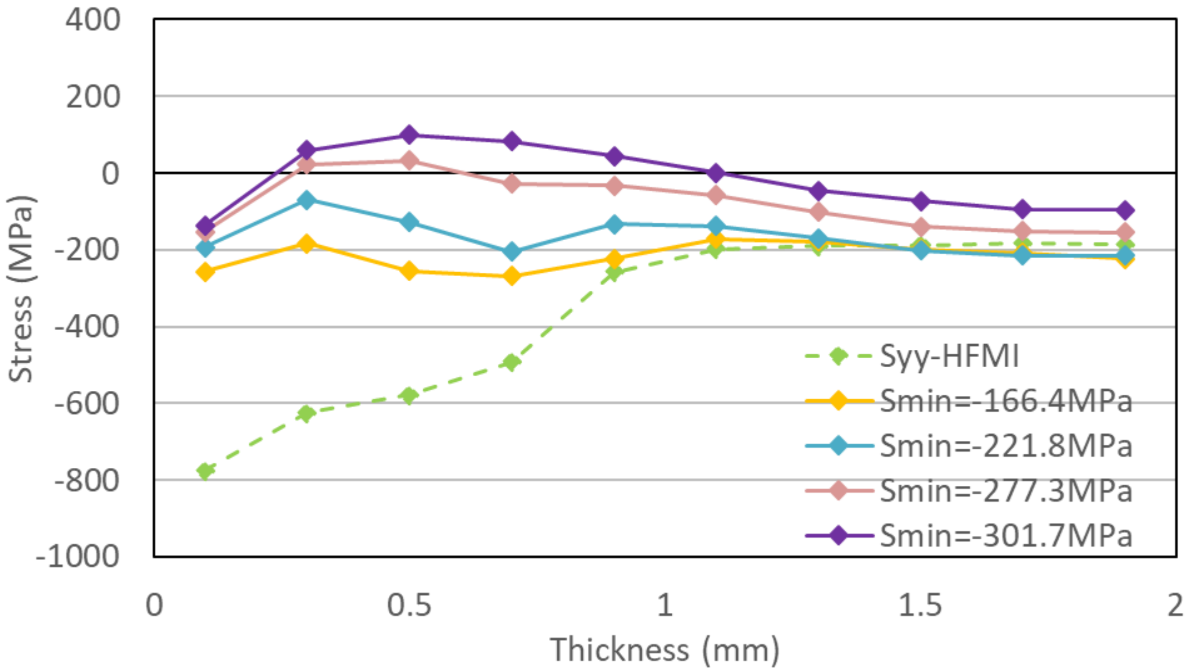

(b) Transversal (S_{YY}) stress.

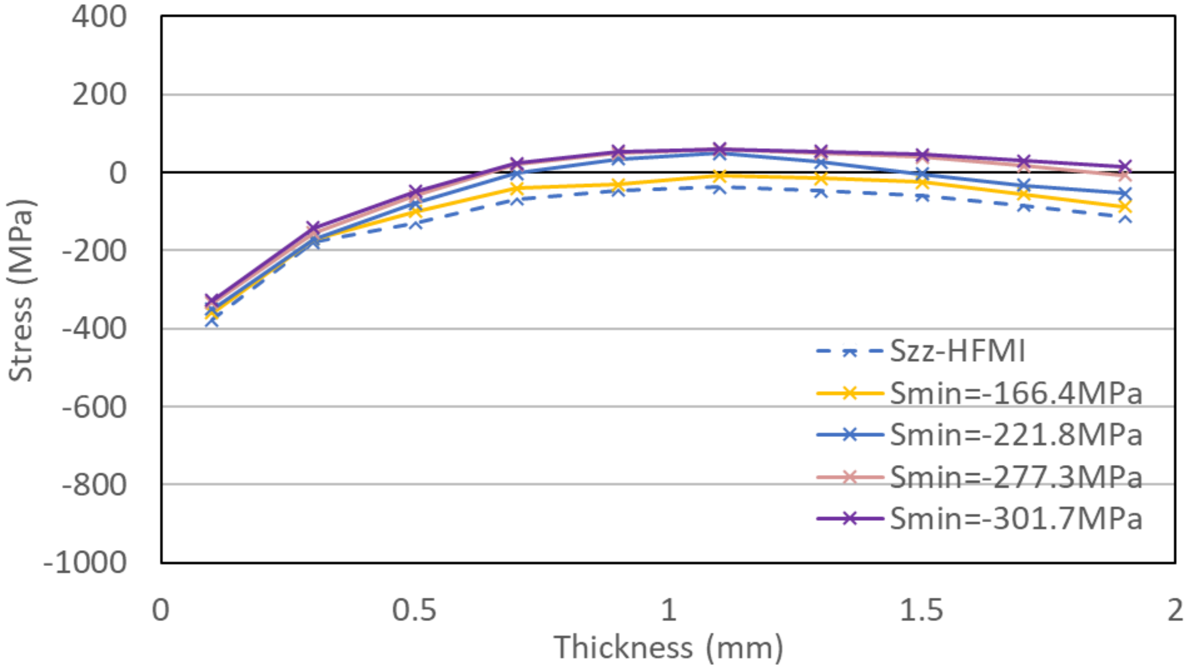

(c) Out of plane (S_{ZZ}) stress.

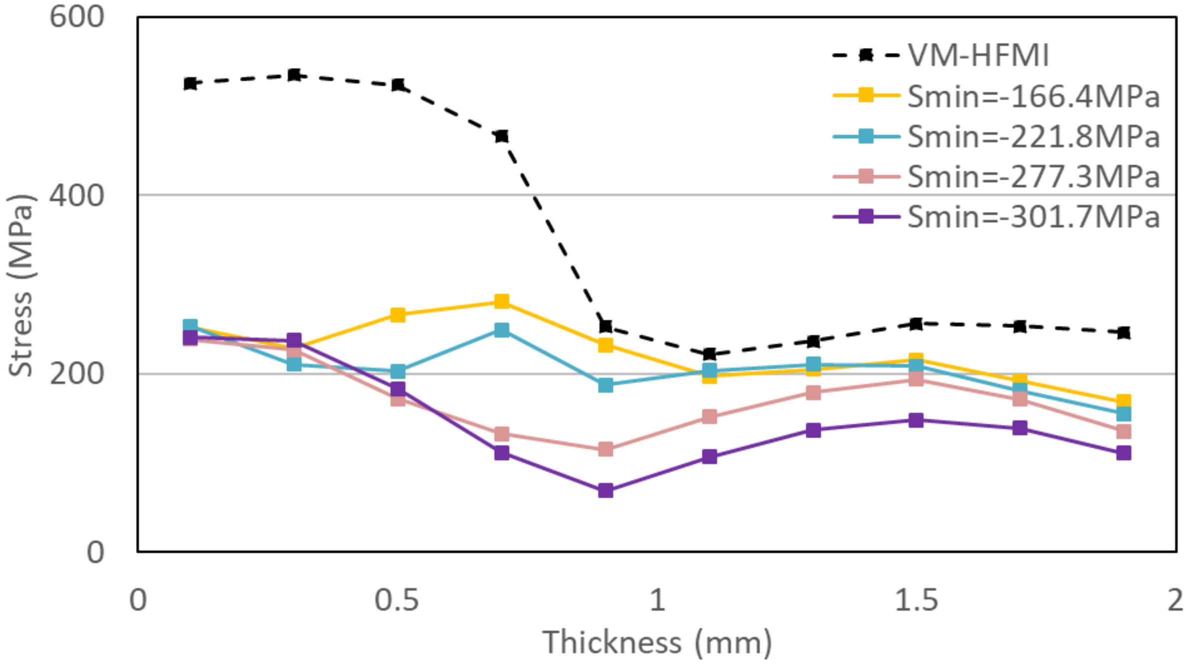

(d) Von Mises (VM) stress.

Fig. 6.16 Residual stress comparison under peak load with constant amplitude of +150 MPa.

6.4.2.5 Longitudinal (S_{XX}) residual stress change on the top surface

Fig. 6. 17 summarizes the longitudinal (S_{XX}) residual stress comparison on the top surface between residual stress after HFMI with that after the cyclic loading scenarios shown in Fig. 6.12.

After compressive peak loads

It is shown that the benefits of the compressive residual stress induced by HFMI on the top surface decrease under the applied compressive peak load. Getting a minimum relaxation of about 65% (from -378MPa to -132MPa).

After compressive peak load followed by constant amplitude of +50 MPa

It is shown that the applied cyclic loading with a maximum nominal stress of +50 MPa induces compressive residual stress on the top surface. Getting a minimum relaxation of about 52.8% (from -378 MPa to -200 MPa).

After compressive peak load followed by constant amplitude of +75 MPa

Applying a maximum nominal stress of +75 MPa after the compressive peak load gives stress relaxation of about 32.9% (from -378MPa to -254 MPa).

After compressive peak load followed by constant amplitude of +150 MPa

Applying a maximum nominal stress of +150 MPa after the compressive peak load gives negligible relaxation of about 7% (from -378 MPa to -352 MPa). When compressive peak load of S_{min}=-166.4 MPa and S_{min}=-221.8 MPa are applied, compressive residual stress is introduced on the top surface. Getting a maximum increase of about 23.6% (from -378 MPa to -468 MPa).

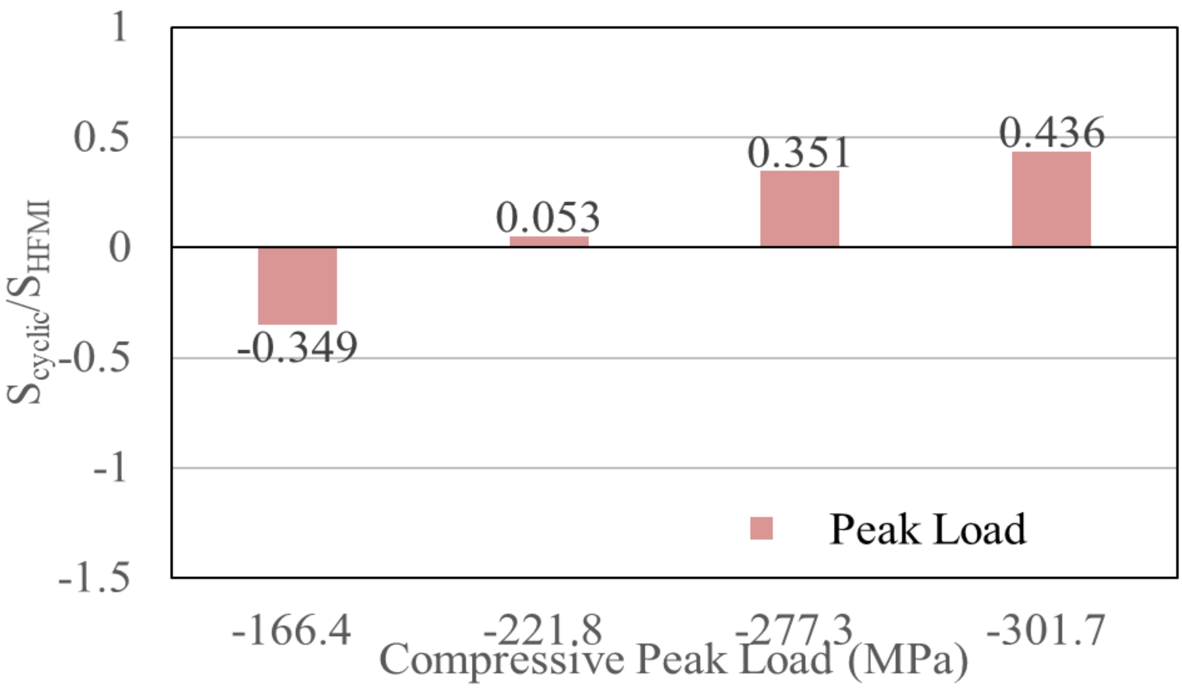

(a) Residual stress comparison after compressive peak load.

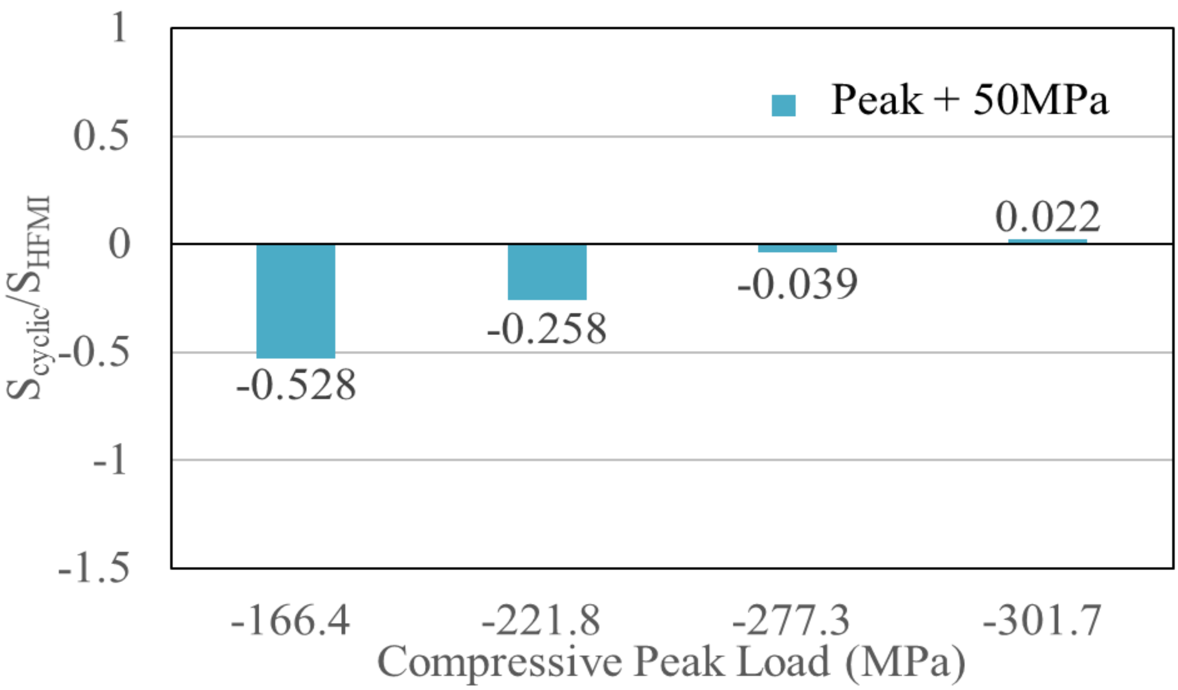

(b) Compressive peak load with constant amplitude of +50 MPa.

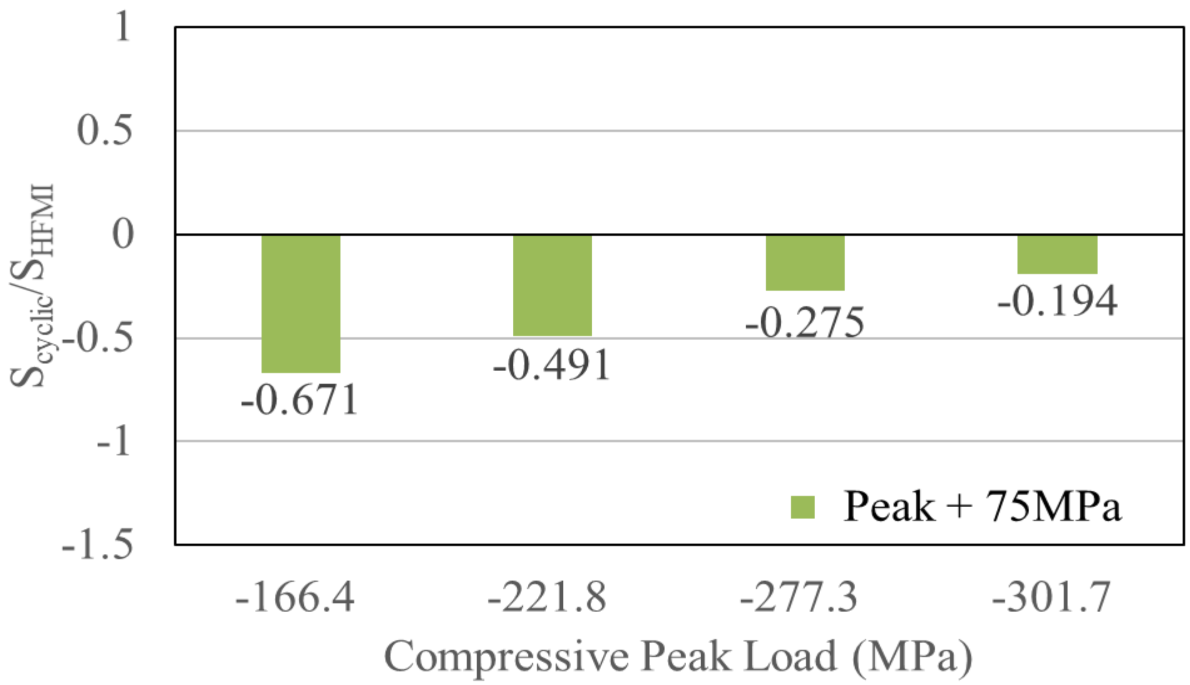

(c) Compressive peak load with constant amplitude of +75 MPa.

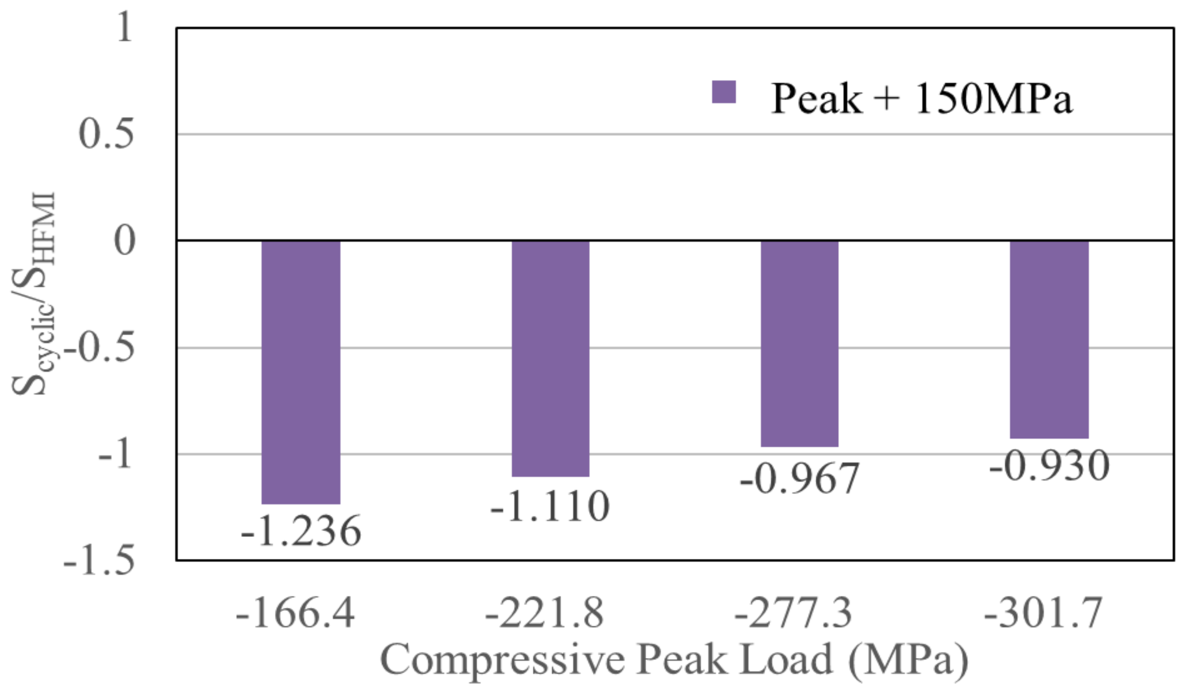

(d) Compressive peak load with constant amplitude of +150 MPa.

Fig. 6.17 Longitudinal residual stress comparison on the top surface under peak load with constant amplitude.

6.5 Conclusions

Stability of the compressive residual stress induced by HFMI under different cyclic loading scenarios was numerically investigated. The benefits of HFMI have only small deteriorations in the loading direction (X-dir) under small tensile constant amplitude loading. Higher nominal stress during constant amplitude loading scenarios induce compressive stress in the loading direction (X-dir). However, relaxation of transversal (S_{YY}) and Von Mises stress is observed.

The benefit from HFMI compressive residual stress deteriorate under cyclic loading with peak loads that causes compressive yielding in the HFMI treated region. These trends are similar to stress behavior focusing on the stability of residual stress induced by ultrasonic peening shown in Hara et al. [63] and pneumatic impact treatment shown in [65]. However, if high nominal cyclic tensile stress is applied in the subsequent constant amplitude loading, an increment of the compressive residual stress in the loading (X-dir.) direction near the top surface is obtained.

Chapter 7 Conclusions and Recommendations

7.1 Introduction

This chapter summarizes the thesis and identifies the major contributions by this research work. Directions for future work and possible extensions to this research are presented at the end of this chapter.

7.2 Conclusions and Contributions

In this research, optimum HFMI simulation conditions were recommended for the post-weld treatment HFMI. Furthermore, practical numerical simulation method of welding, followed by HFMI has been developed. Finally, stability of the compressive residual stress induced by HFMI under different cyclic loading scenarios was numerically investigated. The major conclusions of the thesis are:

HFMI simulation on a flat stress-free plate:

1. Finite element mesh sensitivity simulation

    a. Finite element mesh has a significant effect on results. It was found that the ratio of element size in the treated region/pin tip radius, should be equal or less than 0.1 in order to obtain reliable results.

2. Comparison of numerical simulation with experiment

    a. The validity of the proposed numerical simulation using the recommended FE mesh size and the implementation of the kinematic hardening material by a user subroutine in Dytran, was demonstrated by comparison with experimental measurements and numerical results, improving the numerical results presented in Ernould et al. [56].

3. Recommendation of optimum simulation conditions

   a. Strain hardening should be taken into account to get accurate residual stress in the thickness direction.

   b. Moderate variation of hardening coefficient has not shown a big influence on residual stress.

   c. Increase of HFMI indentation depth causes increases of residual stress components.

   d. Strain rate has shown moderate influence on normal residual stress components. However, for simplicity of collecting material properties, analysis of residual stress induced by HFMI without consideration of strain rate dependency is adopted and found to lead to reasonable agreement with experiments.

   e. Yield stress shows a big impact on the longitudinal (X-dir.) residual stress.

   f. Moderate variation of impact pitch and radius of pin have not shown a big influence on residual stress.

HFMI Simulation on an Out-of-Plane Gusset Welded Joint:

1. Welding Simulation:

   a. Comparison between the computed residual stress by JWRIAN with Abaqus showed good agreement with similar trend through the thickness direction. Differences are observed, they may be caused by different element formulations.

   b. The computed residual stress distribution in the thickness direction of the main plate shows similar trend with the experimental measurements, even though different material properties, welding and boundary conditions were used in the numerical simulation.

   c. The experimental compressive welding residual stress [66] near the top surface may be caused by convection between air with the surface of the weld bead. Increase of residual stress from 0.1mm to 0.6mm in the thickness direction of the main plate may be caused by experimental measurement errors.

2. HFMI simulation:

   a. The welding residual stress field from JWRIAN into Dytran was well imported.

   b. HFMI induced residual stress when welding residual stress is taken into account is compared to that when welding residual stress is not taken into account. Differences of about 23% near the top surface and 41% in the thickness direction were found. These differences reveal that welding residual stresses cannot be neglected in the HFMI simulation.

c. The expected change of welding residual stress behavior due to HFMI, turning from tensile to compressive is confirmed.

d. The computed longitudinal (S_{XX}) compressive residual stress shows similar trend with the experimental measurements, especially near the top surface, despite the different material properties, boundary conditions and welding residual stress field which were assumed in the HFMI numerical simulation.

e. The proposed practical numerical simulation method of welding, followed by HFMI through simulation was established and demonstrated.

3. Cyclic Loading Simulation:

3.1 Cyclic Constant Amplitude Loading

a. It was found that the tensile constant amplitude loading scenarios investigated in this study, cause the HFMI induced compressive residual stress to increase near the top surface in the loading (X-dir.) direction at the target location.

b. Transversal (Y-dir.) stress and Von Mises (VM) stress are relaxed under any scenario.

3.2 Cyclic Loading with Peak Load

a. In general, a compressive peak load deteriorates the benefits of HFMI. Getting similar behavior as in Refs. [63, 65] even with different materials and conditions.

b. When high maximum nominal stress in the subsequent constant amplitude loading is applied, an increment of the compressive residual stress in the loading (X-dir.) stress near the top surface is obtained. However, some relaxation in the thickness direction is observed.

7.3 Recommendations for Future Works

This study provides the basis to carry out a practical numerical simulation of welding, followed by HFMI and cyclic loading. However, additional improvements are necessary:

a. This study considered kinematic hardening model during HFMI and cyclic loading simulation. However, stress response with isotropic and combine isotropic-kinematic hardening material should be considered for a better understanding of the material behavior in the post-weld treatment process and the stress relaxation.

b. In this study, the stability of residual stress under common constant amplitude loadings and cyclic loading with a compressive peak load followed by constant amplitude loadings was investigated. However, it is necessary to find out the magnitude of the loading that does not considerably deteriorate the benefits of the post-weld treatment. Also, it is needed to use realistic loadings conditions with variables wave amplitudes.

c. This study compared numerical results with experimental measurements. However, due to lack of information from the literature, comparison using the proper material properties and welding / HFMI / cyclic loading conditions could not be done. Therefore, it is necessary to carry out a comparison between numerical simulation (welding, HFMI and cyclic loading) with experimental measurements, where all conditions are well known.

References

1. Gurney T R (1979) Fatigue of welded structures. 2nd edition, Cambridge University Press, Cambridge.

2. Fisher J W (1984) Fatigue and fracture in steel bridges. Wiley Interscience.

3. Maddox S J (1991) Fatigue strength of welded structures. 2nd edition, Abington Publishing, Abington, Cambridge.

4. ASM International (2008) Elements of metallurgy and engineering alloys.

5. Ship Research Panel 245 – SR245 (2000) Study on ship structural life of the double hull tanker. The Shipbuilding Research Association of Japan (JSRA) (in Japanese).

6. Maddox S J (2011) Fatigue design rules for welded structures. Fracture and Fatigue of Welded Joints and Structures, Elsevier BV, 168-207, https://doi.org/10.1533/9780857092502.2.168.

7. Ueda Y, Murakawa H, Ma (1996) Measuring method for residual stress in explosively clad plates and a method of residual stress reduction. ASME, JI Engi Mater Tech, 118(10),576-82.

8. Ueda Y, Fukuda k, Nishimura I, Iiyama H, Chiba N, Fukuda M (1983) Three-dimensional cold bending and welding residual stresses in penstock 80kgf/mm^2 class high strength steel plate. Trans JWRI, 12(2), 117-26.

9. Ueda Y, Kim Y, Yuan M (1989) A predicting method of welding residual stress using source of residual stress (Report I), characteristics of inherent strain (Source of Residual stress). Trans JWRI, 18(1), 135-41.

10. Yuan M (1990) Research on estimating method of welding residual stress in plated structures based on the characteristic of inherent strain. PhD. Dissertation, Osaka Univ., Japan.

11. Wang J C, Rashed S, Murakawa H, and Shibahara M (2011) Investigation of buckling deformation of thin plate welded structures. Proceedings of 21st International Society of Ocean and Polar Engineering, USA Hawaii, ISOPE, 125-131.

12. Luo Y, Murakawa H, and Ueda Y (1997) Prediction of welding deformation and residual stress by elastic FEM based on inherent strain (first report): mechanism of inherent strain production. Trans JWRI, 26 (2), 49-57.

13. Ueda Y, Murakawa H, Ma N (2012) Welding deformation and residual stress prevention. Butterworth-Heinemann. ISBN 9780123948045.

14. Blandon J (2015) Simulation of line heating using gas torch for industrial problems. PhD. Dissertation, Osaka Univ., Japan.

15. Statnikov E, Trufyakov V, Mikheev P, Kudryavtsev Y (1996) Specification for weld toe improvement by ultrasonic impact treatment. IIW Document XIII-1617-96.

16. Hagensen P J, Maddox, S J (2013) IIW Recommendations on Post Weld Fatigue Life Improvement of Steel and Aluminum Structures, Woodhead Publishing Ltd., Cambridge.

17. Tai M, Miki C (2014) Fatigue strength improvement by hammer peening treatment-verification from plastic deformation, residual stress, and fatigue crack propagation rate. Weld World 2014, 58, 307-18.

18. Marquis G B, Barsoum Z (2013) A guideline for fatigue strength improvement of high strength steel welded structures using high frequency mechanical impact. Procedia Engineering, 66, 98-107.

19. Yildirim H C, Marquis G B (2012) Fatigue strength improvement factors for high strength steel welded joints treated by high frequency mechanical impact, International Journal of fatigue, 44, 168-76.

20. Yildirim H C, Marquis G B, Barsoum Z (2013) Fatigue assessment of high frequency mechanical impact (HFMI) improved fillet welds by local approaches, International Journal of Fatigue, 52, 57-67.

21. Marquis G B, Mikkola E, Yildirim H C, Barsoum Z (2013) Fatigue Strength Improvement of Steel Structures by High Frequency Mechanical Impact: Proposed Fatigue Assessment Guidelines, Weld World, 57, 803-822.

22. Marquis G B, Barsoum Z (2013) Fatigue Strength Improvement of Steel Structures by High Frequency Mechanical Impact: proposed procedures and quality assurance guidelines, Welding in the World. DOI 10.1007/s40194-013-0077-8.

23. Yildirim H C, Design aspects of high strength steel welded structures improved by high frequency mechanical impact (HFMI) treatment. PhD thesis, Aalto University, Helsinki, 2013.

24. Yildirim H C, Marquis G B (2014) Fatigue design of axially-loaded high frequency mechanical impact treated welds by the effective notch stress method. Mater Des 58:543–550.

25. Haagensen P J, Maddox S J (2010) IIW Recommendations on post weld improvement of steel and aluminum structures, IIW Document XIII-2200r4-07, revised February 2010

26. Le Quilliec G, Lieurade H-P, Bousseau M, Drissi-Habti M, Inglebert G, Maxquet P, Jubin L (2011) Fatigue behavior of Welded Joints Treated by High Frequency Hammer Peening: Part I, Experimental study, IIW Document XIII-2394-11.

27. Tehrani Yekta R, Ghahremani K (2013) Scott Walbridge: effect of quality control parameter variations on the fatigue performance of ultrasonic impact treated welds. Int J Fatigue 55:245–256.

28. Berg J, Stranghoener N (2014) Fatigue strength of welded ultra high strength steels improved by high frequency hammer peening. Proc Mater Sci 3, 71-76.

29. Leitner M, Gerstbrein S, Ottersböck MJ, Stoschka M (2015) Fatigue strength of HFMI-treated high-strength steel joints under constant and variable amplitude block loading. Proc Eng 101,251-258.

30. Lefebvre F, Revilla-Gomez C, Buffiere J-Y, Verdu C, Peyrac C (2014) Understanding the mechanism responsible for the beneficial effect of hammer peening in welded structures under fatigue loading. Advanced Materials Research 996:761-768.

31. Mikkola E, Marquis G, Lehto P, Remes H, Hänninen H (2016) Material characterization of high-frequency mechanical impact treated high-strength steel. Materials & Design 89:205-214.

32. Morikage Y (2015) Improvement mechanism of fatigue strength of weld joints by hammer peening on base metal. Quarterly Journal of JWS. 33, 111-117 (in Japanese).

33. Tsutsumi S, Nagato R, Fincato R, Ishikawa T, Matsumoto R (2017) Numerical and Experimental Study on Fatigue Life Extension of U-rib Steel Structure by Hammer Peening. Proceedings of The Welding Society, Vol 35, 2, 169-172.

34. Ishikawa T, Matsumoto R, Tsutsumi S, Kawano H (2014) Fatigue Strength Improvement of rib-to-deck joints of orthotropic Steel Deck by Peening.

35. Sumi Y, Yuan K (2016) Simulation of Residual Stress and Fatigue Strength of Welded Joints under the Effects of Ultrasonic Impact Treatment (UIT). International Journal of Fatigue, 92, 321-332. DOI: 10.1016/j.ijfatigue.2016.07.018

36. Suzuki T, Okawa T, Shimanuki H, Nose T, Ohta N, Suzuki G, Moriai A (2014) Effect of Ultrasonic Impact Treatment (UIT) on Fatigue Strength of Welded Joints, Advanced Materials Research, 996, 736-742.

37. Mori T, Shimanuki H, Tanaka M (2012) Effect of UTI on Fatigue Strength of Web-Gusset Welded Joints Considering Service Condition of Steel Structures, Weld World, 56,9-10,141-149.

38. Nose T, Shimanuki H, Nakajima K, Suzuki T (2006) Fatigue Strength Improvement Mechanism in Welded Joint by the Ultrasonic Impact Treatment, Proceedings of National Symposium on Welding Mechanics and design, 219-222.

39. Nose T, Shimanuki H (2008) Experiment and Analysis of Influence of Ultrasonic Peening on Fatigue Life in Pad Welded Joints, Transactions of Japan Society of Mechanical Engineers, 166-168.

40. Statnikov E (1997) Comparison of Post-Weld Deformation Methods for Increase in Fatigue Strength of Welded Joints, IIW Doc.-XIII, 1668-97.

41. Statnikov E (1999) Guide for Application of Ultrasonic Impact Treatment for Improving Fatigue Life of Welded Structure, IIW/IIS Doc.-XIII, 1757-99.

42. Yalchiner F B, Barsoum Z (2017) Life extension of welded structures using HFMI techniques-potential application to offshore structures, 2nd International Conference on Structural Integrity, ICSI 2017.

43. Hardenacke V, Farajian M, Siegele D (2014) Modelling and Simulation of High Frequency Mechanical Impact (HFMI) Treatment of Welded Joints, IIW Document XIII-2533-14.

44. Le Quilliec G, Lieurade H-P, Bousseau M, Drissi-Habti M, Inglebert G, Macquet P, Jubin L (2011) Fatigue Behavior of Welded Joints Treated by High Frequency Hammer Peening: Part II, Numerical Study, IIW Document XIII-2395-11.

45. Baptista R, Infante V, Branco C (2011) Fully dynamic numerical simulation of the hammer peening fatigue life improvement technique. Proc Eng 10:1943–1948

46. Simunek D, Leitner M, Stoschka M (2013) Numerical simulation loop to investigate the local fatigue behaviour of welded and HFMI-treated joints, IIW Document XIII-WG2-136-13.

47. Guo C, Shengsun H, Wang D, Wang Z (2015) Finite element analysis of the effect of the controlled parameters on plate forming induced by ultrasonic impact forming (UIF) process, Applied Surface Science 353, 382-390.

48. Foehrenbach J, Hardenacke V, Farajian M (2016) High Frequency Mechanical Impact Treatment (HFMI) for Fatigue Improvement: Numerical and experimental investigations to describe the conditions in the surface layer, Welding in the World.

49. Foehrenbach J (2015) Fatigue life prediction of High Frequency Mechanical Impact treated welded joints by numerical simulation and damage mechanic approaches, Master Thesis, Offenburg University of Applied Science.

50. Le Quilliec G, Lieurade H-P, Bousseau M, Drissi-Habti M, Inglebert G, Macquet P (2013) Mechanics and modelling of high-frequency mechanical impact and its effect on fatigue, Weld World 57, 97-111.

51. Hu S, Guo C, Wang D, Wang Z (2016) 3D Dynamic Finite Element Analysis of the non-uniform residual stress in ultrasonic impact treatment process, Journal of Materials Engineering and Performance Vol. 25, 2016, 4004-4015.

52. Khurshid M, Leitner M, Barsoum Z, Schneider C (2016) Residual stress state induced by high frequency mechanical impact treatment in different steel grades - Numerical and experimental study, International Journal of Mechanical Sciences 123, 34-42.

53. Yuan K, Sumi Y (2016) Simulation of residual stress and fatigue strength of welded joints under the effects of ultrasonic impact treatment (UIT), International Journal of Fatigue 92, 321-332.

54. Deng C, Liu Y, Gong B, Wang D (2016) Numerical implementation for fatigue assessment of butt joint improved by high frequency mechanical impact treatment: A structural hot spot stress approach, International Journal of Fatigue 92,211-219.

55. Yang X, Zhou J, Ling X (2012) Study of plastic damage of AISI 304 stainless steel induced by ultrasonic impact treatment, Material and Design 36, 477-481.

56. Ernould C, Schubnell J, Simunek D, Leitner M, Maciolek A, Farajian M, Stoschka M (2019) Application of Different Simulation Approaches to Numerically Optimize High-

Frequency Mechanical Impact (HFMI) Post-Treatment Process, Welding in the World, 725-738.

57. Stoschka M, Leitner M, Ottersbock M (2016) Quality assurance of HFMI-treatment regarding fatigue strength of fillet welds. IIW Document XIII-2635-16.

58. Chaboche J-L (1986) Time-independent constitutive theories for cyclic plasticity, International Journal of Plasticity 2.2, 149-188.

59. Johnson G R, Cook W H (1983) A constitutive model and data for metals subjected to large strains, high strain rates and high temperatures.

60. Tai M, Miki C (2012) Improvement effects of fatigue strength by burr grinding and hammer peening under variable amplitude loading. Weld World, 56,109–17.

61. Miyashita D (2011) Relaxation behavior of laser peening residual stressdue to mechanical loading on aluminum alloy, Trans. JSME., 60, 617-623 (in Japanese)

62. Yildirim H C, Marquis G, Sonsino C M (2016) Lightweight design with welded high frequency mechanical impact (HFMI) treated high-strength steel joints from S700 under constant and variable amplitude loadings. Int J Fatigue 2016, 91, 466-74.

63. Hara J, Shimoda T, Deguchi T, Mouri M, Fukuoka T, Koshio K, Kano D (2010) A study on fatigue strength improvement for ship structures by ultrasonic peening Part 1, Conference Proceedings of The Japan Association of Ship and Ocean Engineers, 2010S-G12-4.

64. Okawa T, Shimanuki H, Funatsu Y, Nose T, Sumi Y (2013) Effect of preload and stress ratio on fatigue strength of welded joints improved by ultrasonic impact treatment. Weld World, 57:235-41.

65. Mikkola E, Remes H, Marquis G (2017) A finite element study on residual stress stability and fatigue damage in high-frequency mechanical impact (HFMI)-treated welded joint. International Journal of Fatigue, 94, 16-29.

66. Leitner M, Khurshid M, Barsoum Z (2017) Stability of high-frequency mechanical impact (HFMI) post-treatment induced residual stress states under cyclic loading of welded steel joints, Engineering Structures, 143, 589-602.

67. Ueda Y, Yamakawa T (1971) Thermal Stress Analysis of Metals with Temperature Dependent Mechanical Properties Transactions of JWRI, 2, No 2, 90-100.

68. Ueda Y, Murakawa H, Rashwan A M et al (1993) Development of Compute Aided Process Planning System for Plate Bending by Line Heating (Report IV): Decision Making on Heating Conditions, Locations and Direction (Mechanics, Strength & Structural Design), Transaction of JWRI, 22, 2, 305-313.

69. Huang T D et al. (2003) Residual Stresses and Distortions in Lightweight Ship Panel Structures Northrop Grumman Technical Review-Journal, Spring/Summer, 1-26.

70. Murakawa H (2010) Concept of inherent strain, inherent stress, inherent deformation and inherent force for prediction of welding distortion and residual stress Transactions of JWRI, 39, 2, 103-105.

71. MSC Software (2017) MSC Dytran 2017 Reference Manual.

72. Schäfers F, Gester P, Leitner M (2015) Overview of residual stress measurement and fatigue test data for pneumatic impact treated (PIT) joints, IIW Documents XIII-WG2-146-15.

73. Harati E et al. (2014) Non-destructive measurement of weld toe radius using Weld Impression Analysis, Laser Scanning Profiling and Structured Light Projection methods. First International Conference on Welding and Non Destructive Testing, Tehran, Iran.

74. Ghahremani K, Sara M, Yaung J, Walbridge S, Haas C, Dubois S (2015) Quality assurance for high-frequency mechanical impact (HFMI) treatment of welds using handheld 3D laser scanning technology. Weld World 59(3).

75. Chaboche J-L (2008) A review of some plasticity and viscoplasticity constitutive theories. Int J Plast 24:1642–1693.

76. Muransky O, Hamelin C, Smith M, Bendeich P, Edwards L (2012) The effect of plasticity theory on predicted residual stress fields in numerical weld analyses. Comput Mater Sci 54:125–134.

77. Chaboche JL (1993) Cyclic viscoplastic constitutive equations, Part I: a thermodynamically consistent formulation, J. Appl. Mech. 60, 1993, pp. 813–821. Part II: stored energy—comparison between models and experiments. J Appl Mech 60:822–828.

78. Chaboche JL (1977) Viscoplastic constitutive equations for the description of cyclic and anisotropic behaviour of metals. Bol Acad Sci Sér Sci Tech XXV(1):33.

79. Lemaite J, Chaboche J (1994) Mechanics if solid materials, Cambridge University press.

80. ABAQUS Inc (2016) Abaqus/Explicit Reference Manual.

81. American Institute of Steel and Iron (AISI) (2015) www.steel.org/, 13.11.

82. Ramaswamy G V (1985) A constitutive model for the inelastic multiaxial cyclic response of a nickel base super alloy Rene 80. Doctoral Thesis, University of Cincinnati—Department of aerospace engineering and engineering mechanics.

83. Stoschka M, Leitner M, Fössl T, Posch G (2012) Effect of high-strength filler metals on fatigue. Weld World 2012;5 (3/4):20–9.

84. Stoschka M, Leitner M, Posch G, Eichlseder W (2013) Effect of high-strength filler metals on the fatigue behaviour of butt joints. Weld World 2013, 57, 85-96.

85. Leitner M. Influence of effective stress ratio on the fatigue strength of welded and HFMI-treated high-strength steel joints. Int J Fatigue 2017.

86. Leitner M, Stoschka M, Schörghuber M, Eichlseder W (2011) Fatigue behaviour of high-strength steels using an optimized welding process and high frequency peening technology. In: Proceedings of the international conference of the international institute of welding, Chennai/India; 729-36.

87. Yasuda A., Rashed S (2016) Efficient Collapse Analysis of Ductile Components Subjected to Impact Loads. In: Proceedings of the ASME 35th Int. Conf. Ocean, Offshore and Arctic Engineering (OMAE2016). OMAE2016-54480, South Korea.

88. Leitner M, Khurshid M, Barsoum Z (2016) Stability of HFMI-treatment induced residual stresses during fatigue, IIW Doc. XIII-2633-16.

89. Kim M H (2017) Numerical simulation of high frequency mechanical impact (HFMI) treatment in fillet welded joints. Meeting Presentation to the Specialist Committee on Materials and Fabrication Technology (ISSC 2018), Oslo, January 31, 2017.

90. Goldak J, Chakravarti A, Bibby M (1984) A new Finite Element Model for Welding Heat Sources. Metall Trans B 15:299-305. https://doi.org/10.1007/BF02667333

91. Murakawa H (2018) Numerical Study of Crack Growth in welded structures using characteristic tensor method -influences of stress concentration and residual stress. IIW-Document X-1901-18.

92. Leitner M, Ottersbock M, Pubwald S., Remes H (2018) Fatigue Strength of Welded and High-Frequency Mechanical Impact (HFMI) Post-Treated Steel Joints under Constant and Variable Amplitude Loading. Engineering Structures, 163, 215-223.

93. Ruiz H, Osawa N, Rashed S (2019) A practical analysis of residual stresses induced by high-frequency mechanical impact post-weld treatment, Weld World, https://doi.org/10.1007/s40194-019-00753-w.

Appendix A

Longitudinal (S_{XX}) stress-time history comparison between two different strain rate conditions (not considered and considered) is presented. Stress-time history of an element on the top surface shows that higher stress is obtained with consideration of strain rate.

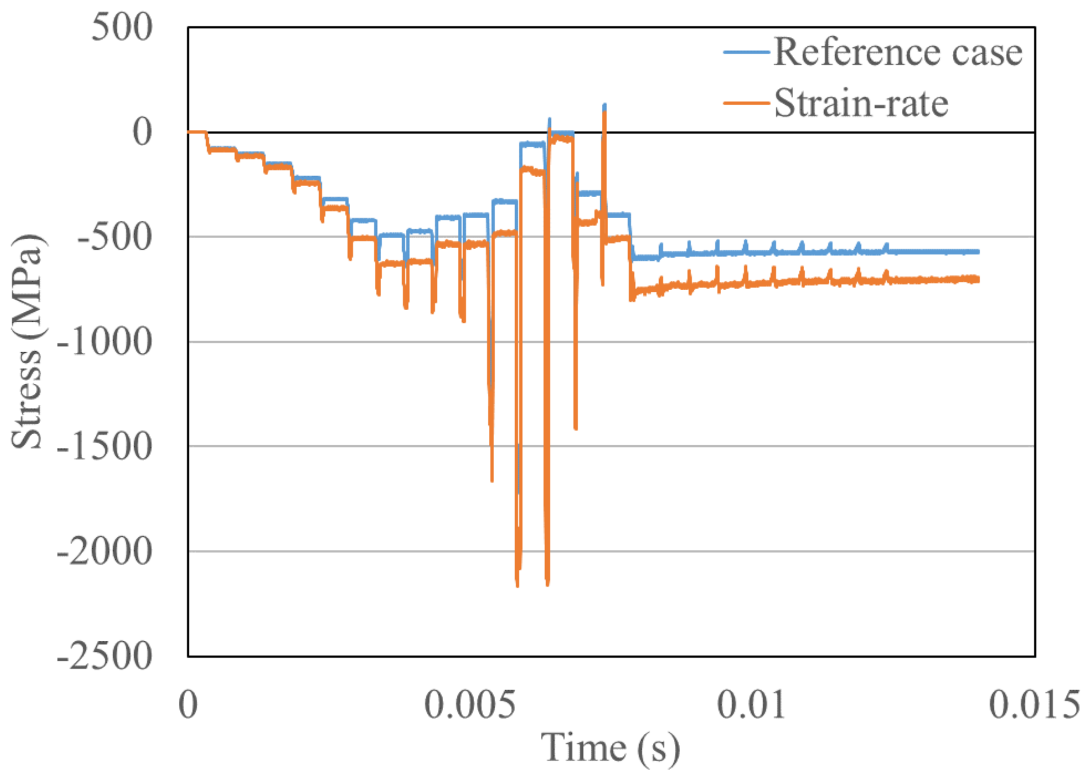

Fig. A-1. Longitudinal (S_{XX}) stress-time comparison of an element on the top surface.

Appendix B

An element in the top surface of the flat plate at the middle of the peening path is chosen to show the longitudinal, transversal and out-of-plane stress-time history and strain-time history.

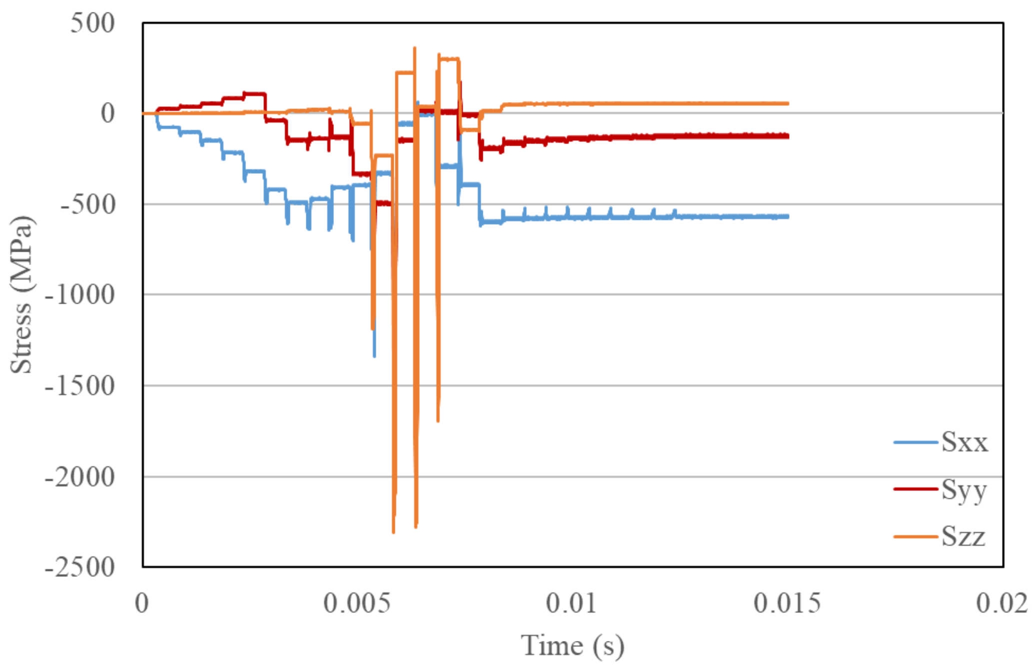

Fig. B-1 Stress-time history during HFMI (Long., transv. and out-of-plane).

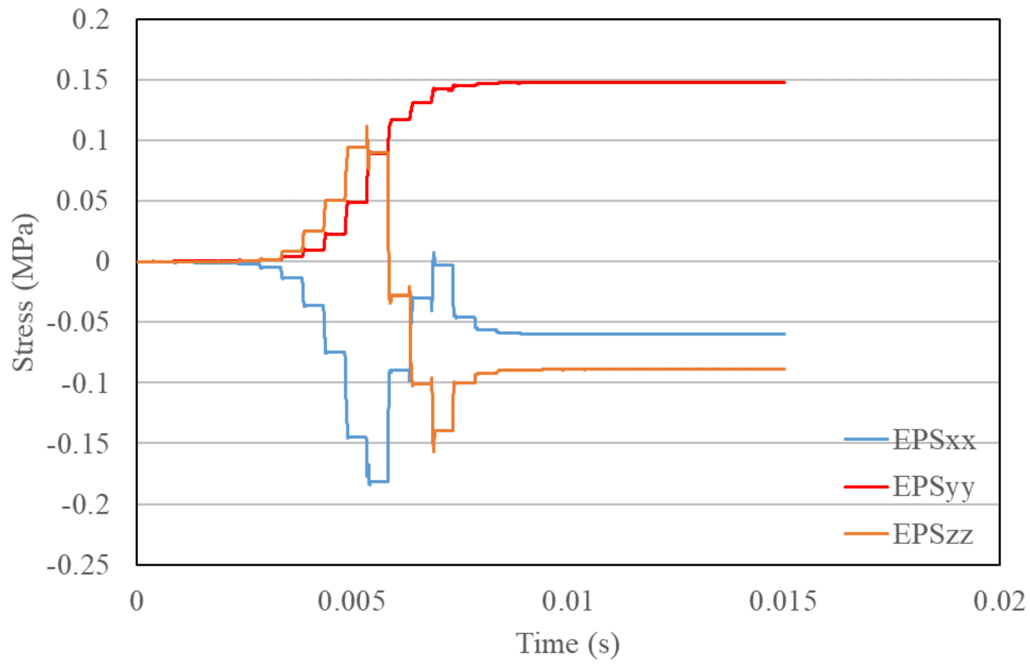

Fig. B-2 Stain-time history during HFMI (Long., transv. and out-of-plane).

Appendix C

Comparison of the HFMI induced residual stress in the thickness direction under different boundary conditions is carried out. The first boundary condition (BC1) was implemented during this research, see Fig. 5.11. The second boundary condition (BC2) considers that bottom surface is fixed in X, Y and Z Dir. In the same manner as the first condition the symmetric face is fixed only in the X-direction, and one node only is fixed in the Y-direction. Same hardening material model and HFMI conditions were used, see Table 3.2 and 5.1.

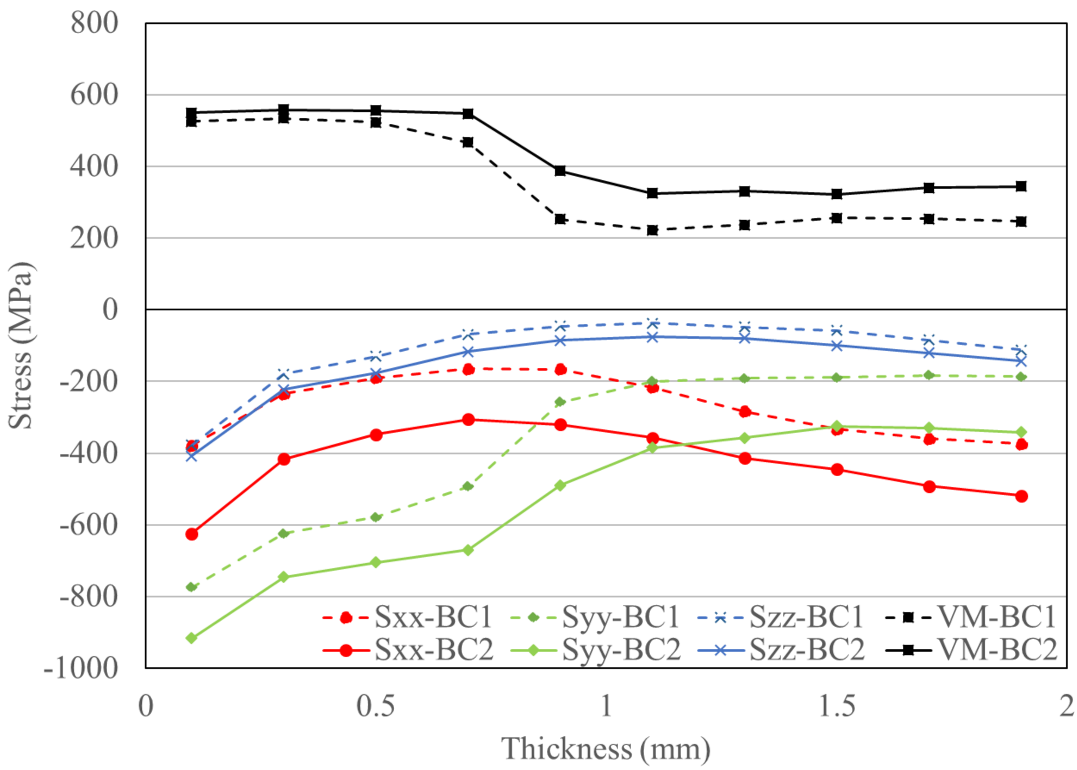

Fig. C-1 HFMI induced residual stress comparison in the thickness direction due to different boundary conditions.

Fig. C-2 shows the residual stress comparison between Pusan National University (PNU) results and the results obtained in this research, when different boundary conditions are considered. The expected behavior turning the welding tensile residual stresses to compressive after HFMI was obtained. However, PNU's residual stress results show fluctuations near the top surface. It may be caused by lack of appropriate hourglass deformation mode control.

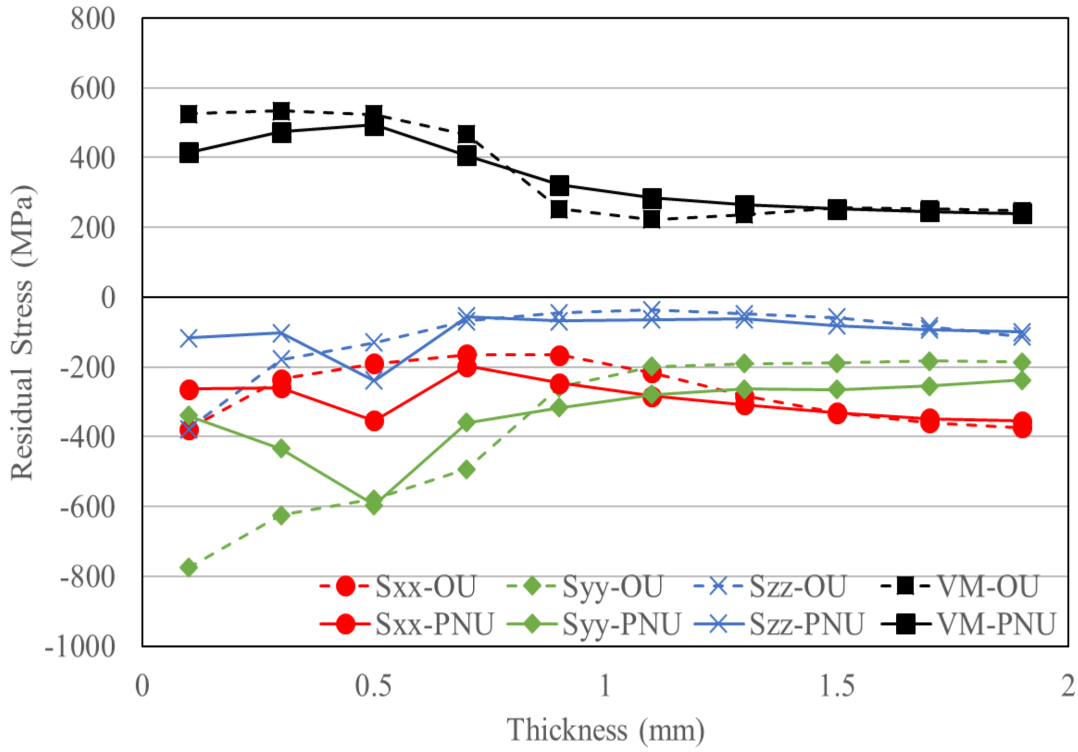

a) Boundary condition 1 (BC2).

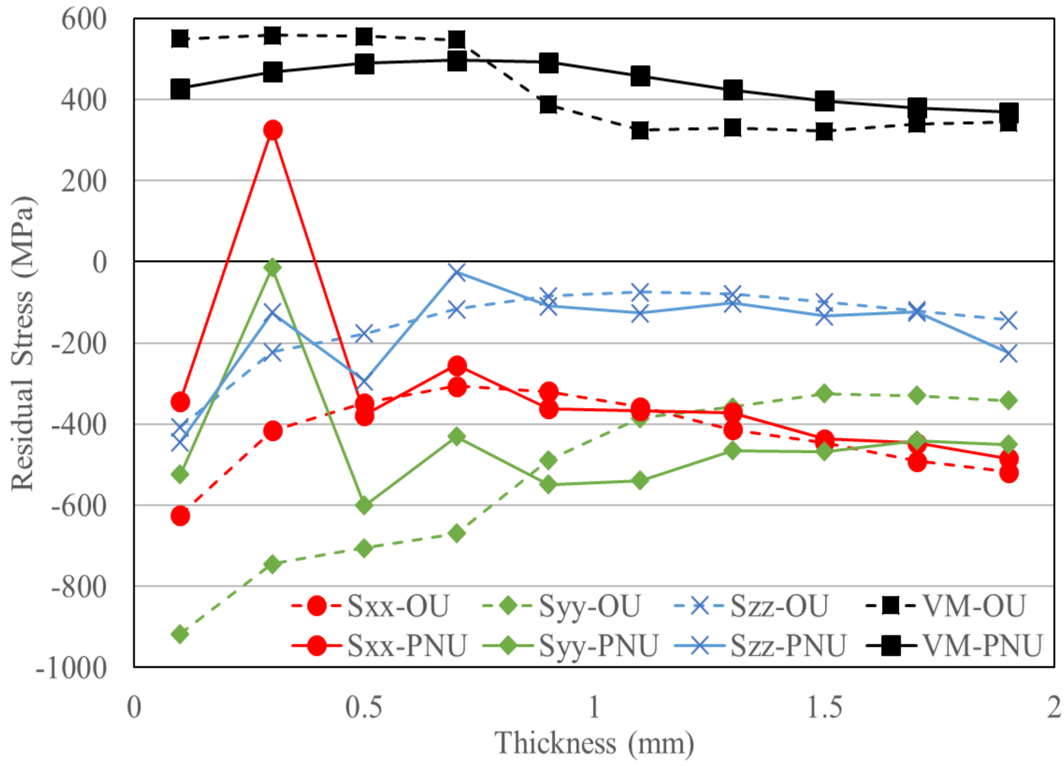

b) Boundary condition 2 (BC2).

Fig. C-2 Residual stress comparison between PNU and the proposed using different boundary conditions.

Appendix D

Comparison between the longitudinal (S_{XX}) residual stress and transversal (S_{YY}) residual stress distribution in the thickness direction at the target location, using a coarse model with minimum element size at the target location of 1.25x1.25x1.25mm and a fine model with a minimum element size of 0.2x0.2x0.2mm. It can be seemed that for welding process the element size at the target location does not affect results. However, during HFMI simulation the element size shows considerable influence. Getting higher compressive residual stress near the top surface or at the weld toe with finer elements. It means that with smaller element size the compressive residual stress will increase.

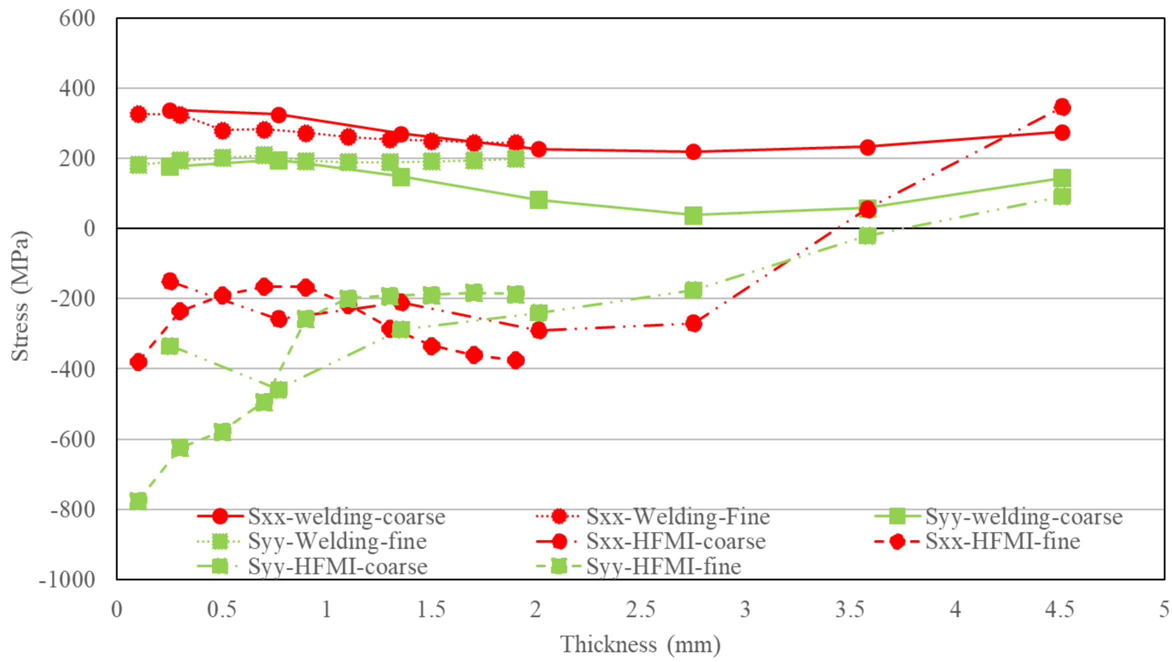

Fig. D-1 Residual stress comparison between coarse and fine model.

Appendix E

Additional to the Fig. 6.4, appendix E shows the residual stress time history and strain time history in an element on the top surface at the target location. Fig. E-1 shows the applied cyclic loading scenario. A nominal stress of +150 MPa and a minimum nominal stress of 0 MPa, with a stress ratio (min. stress/max. stress) of R=0. Strain rate effects are not considered.

Fig. E-2 shows the maximum and minimum stress (S_{YY}, S_{ZZ}, VM) of each cycle at the target location. Fig. E-3 shows the minimum and maximum strain (EPS_{XX}, EPS_{YY}, EFFPLS) of each cycle.

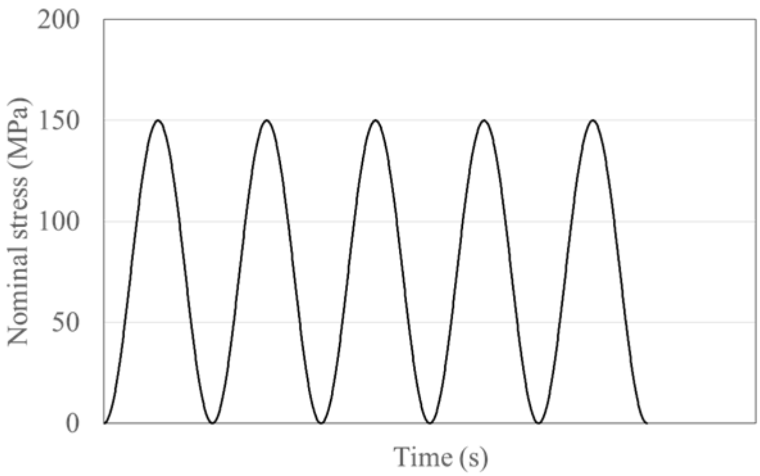

Fig. E-1 Cyclic loading scenario un the longitudinal direction (X-dir.).

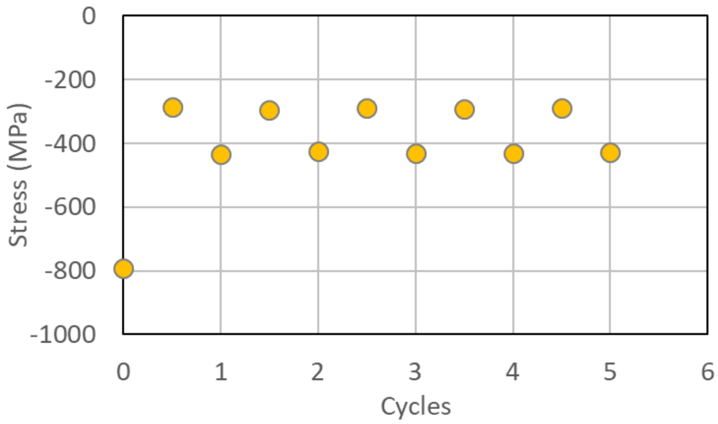

a) Transversal (S_{YY}) stress.

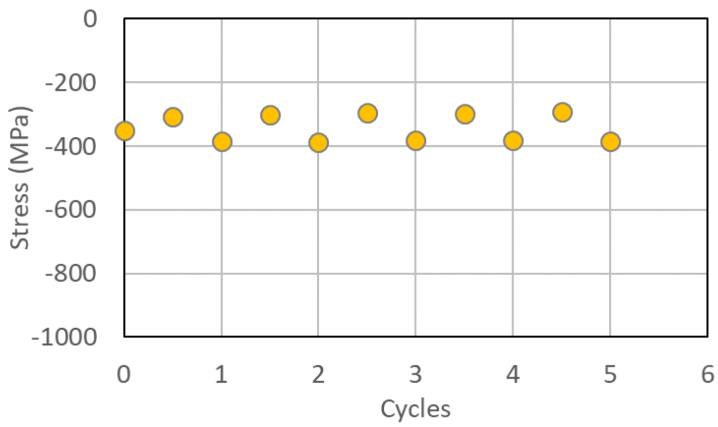

b) Out-of-plane(S_{ZZ}) stress.

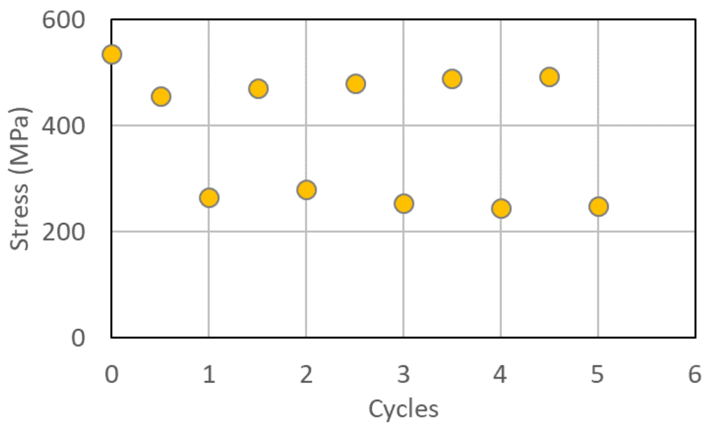

c) Von Mises.

Fig. E-2 Maximum and minimum stress of each cycle at the target location.

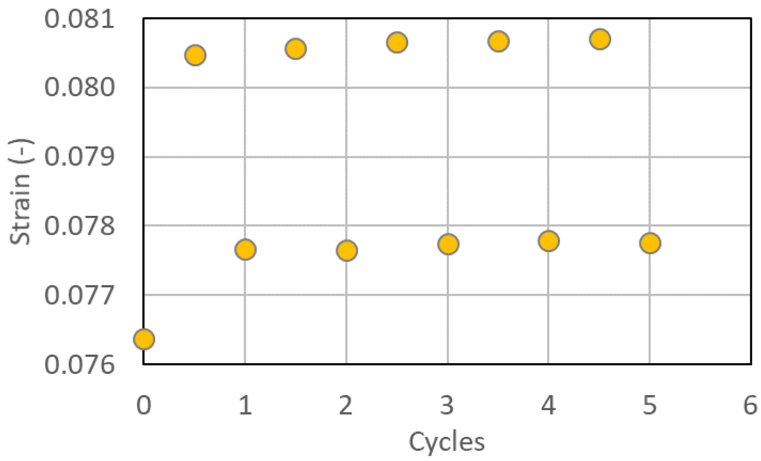

a) Longitudinal strain (EPS_{XX}).

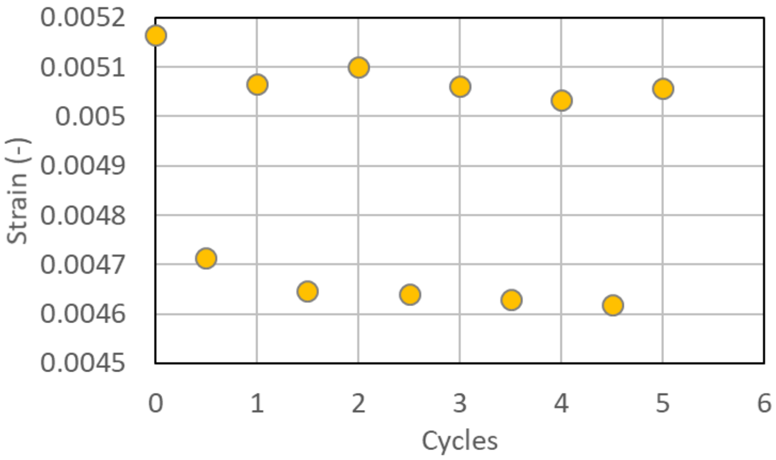

b) Transversal strain (EPS_{YY}).

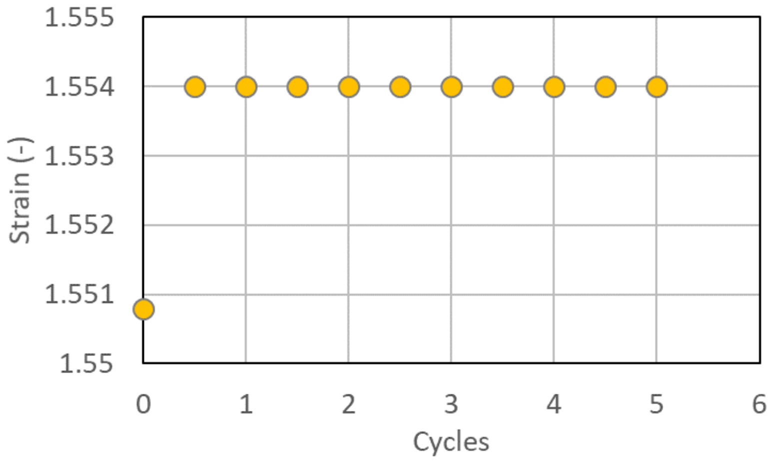

c) Effective plastic strain (EEFPLS).

Fig. E-3 Maximum and minimum strain of each cycle at the target location.

Appendix F

Stress/strain relationship under constant amplitude shown in Fig. F-2. It is shown that under +50 MPa and +75 MPa plasticity is not reached. On the other hand, with a maximum stress of +150 MPa plasticity is reached. Fig. F-1 shows the constant amplitude loading scenarios.

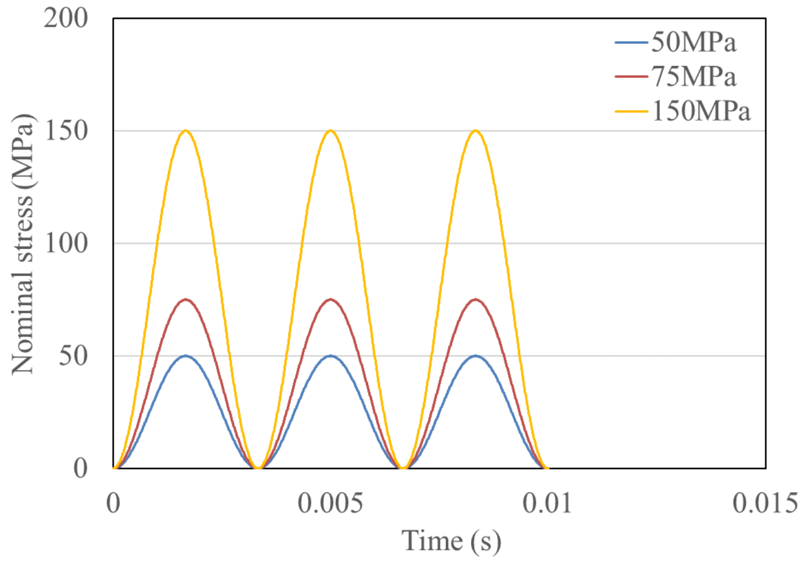

Fig. F-1 Constant amplitude loading scenarios.

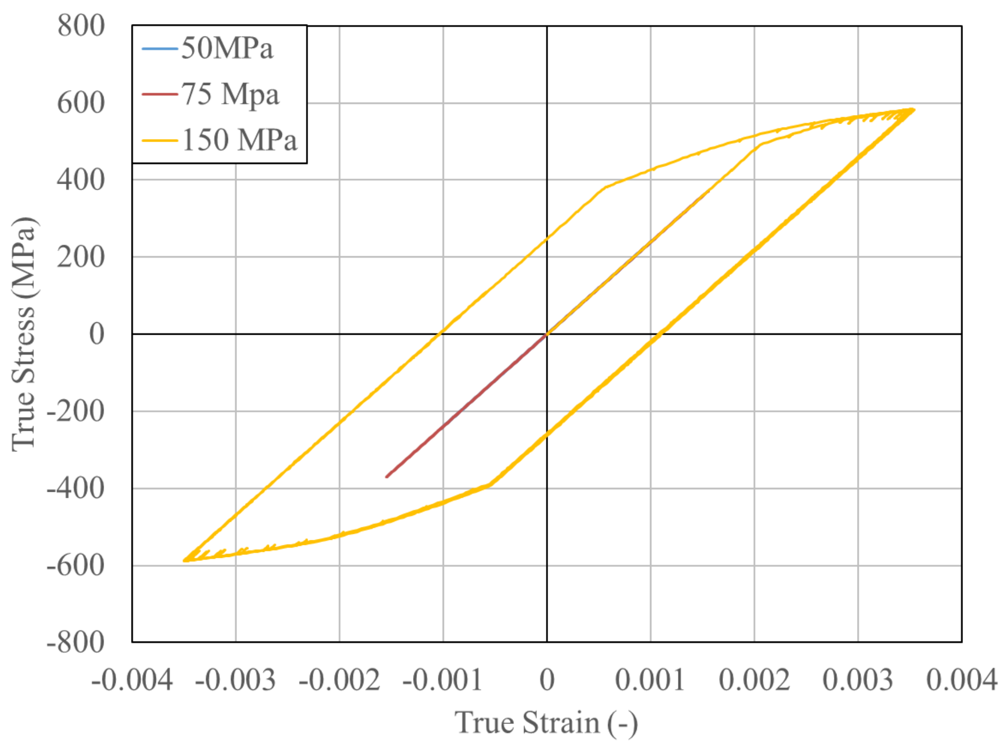

Fig. F-2 Stress/strain relationship.

Appendix G

In this appendix, a comparison of the residual stress distribution in the thickness direction between welding residual stress with the obtained residual stress after constant amplitude loading under a maximum nominal stress of +50 MPa. Fig. G-1 shows the cyclic loading scenario. Residual stress relaxation near the top surface is observed, see fig. G-2.

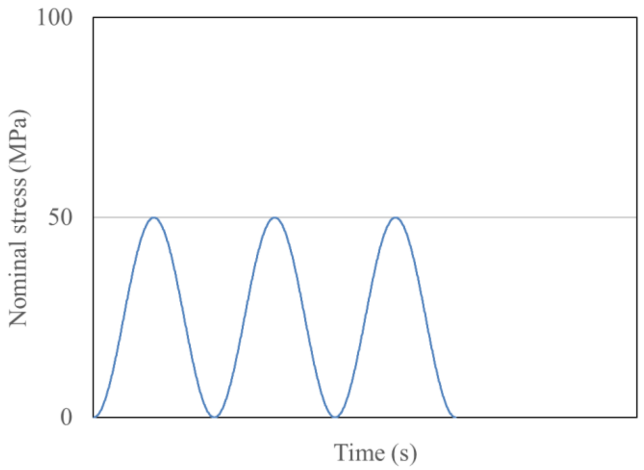

Fig. G-1 Cyclic loading scenario.

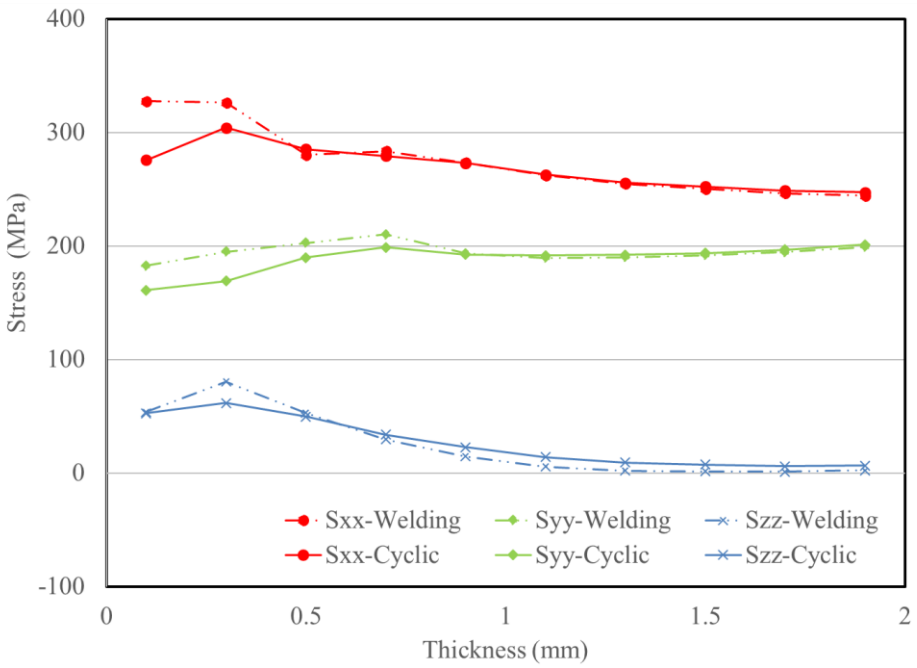

Fig. G-2 Constant amplitude loading with a maximum stress of +50 MPa.

Appendix H

Appendix H shows the stress and strain variation of an element on the top surface of the target location, under different cyclic loading conditions shown in Table H-1. Fig. H-1 shows the stress (S_{XX}, S_{YY} and VM) each half cycle. Fig. H-2 shows the strain (EPS_{XX}, EPS_{YY} and EFFPLS) each half cycle.

Table H-1 Cyclic loading condition

Scenario	Max. Nominal stress (Smin)	Min. Nominal stress (MPa)	Max. Nominal stress (CA loading)	Min. Nominal stress (CA loading)
1	-166.4 MPa	0	150 MPa	0
2	-221.8 MPa	0	150 MPa	0
3	-277.3 MPa	0	150 MPa	0
4	-301.7 MPa	0	150 MPa	0

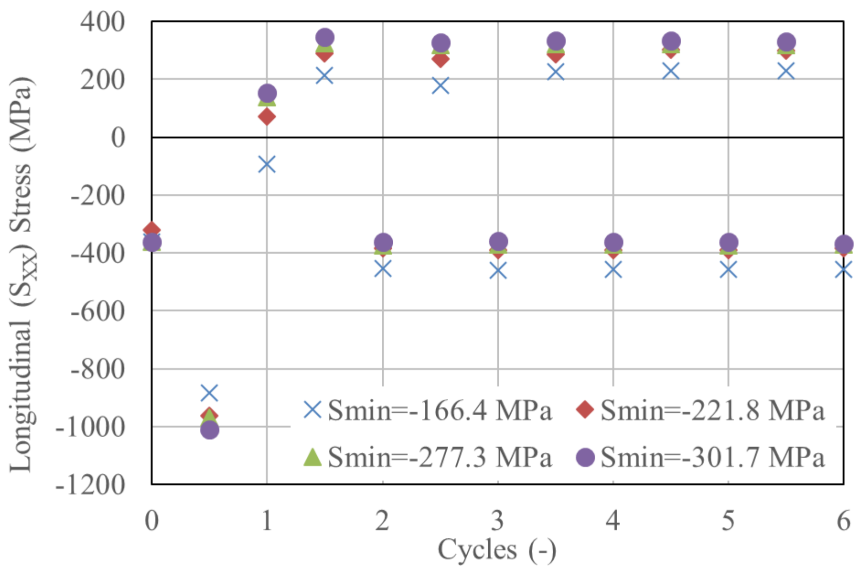

a) Longitudinal (S_{XX}) stress.

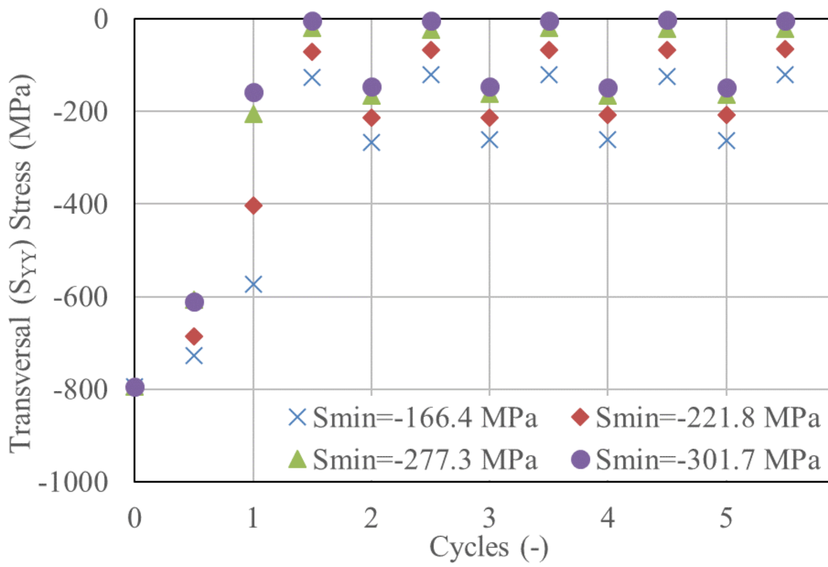

b) Transversal (S_{YY}) stress.

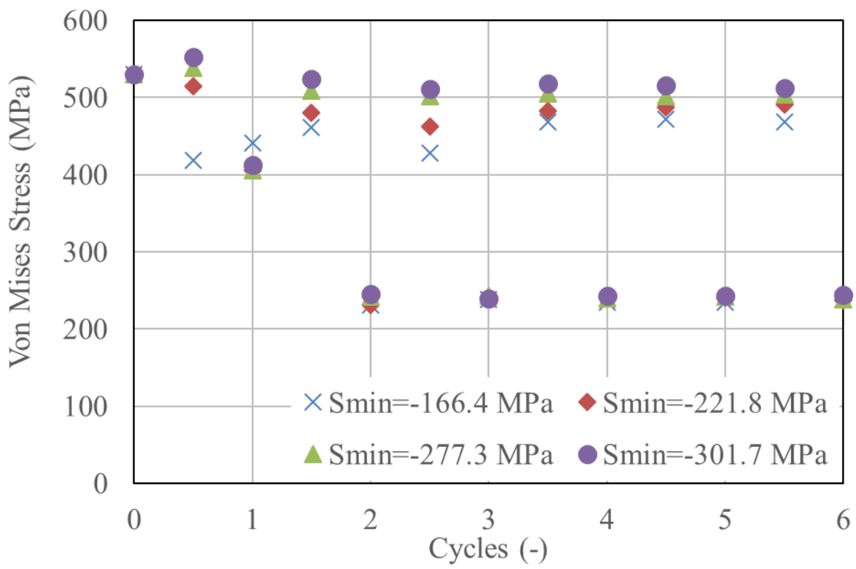

c) Von Mises stress (VM).

Fig. H-1 Maximum and minimum stress of each cycle at the target location (Compressive Peak load + 150 MPa).

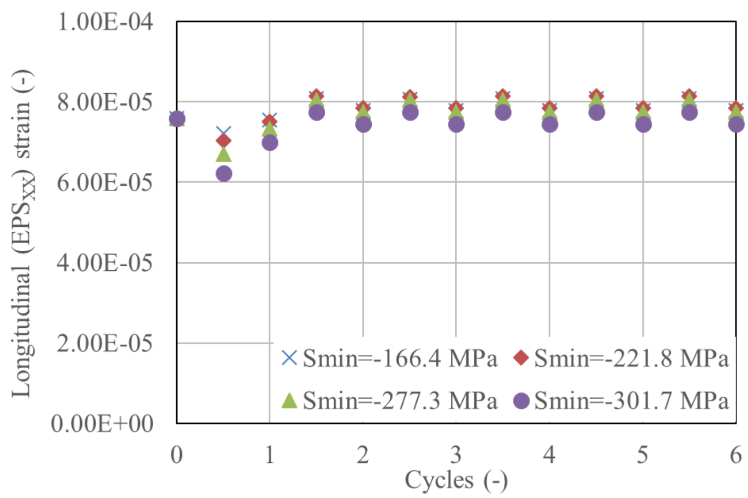

a) Longitudinal (EPS_{XX}) strain.

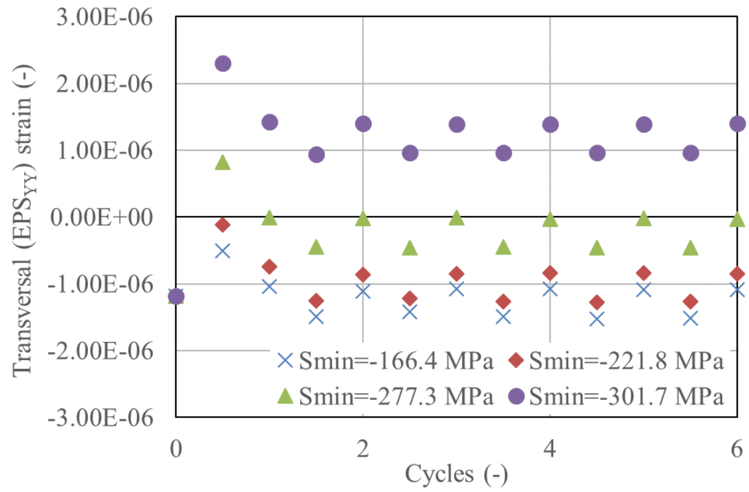

b) Transversal (EPS_{YY}) strain.

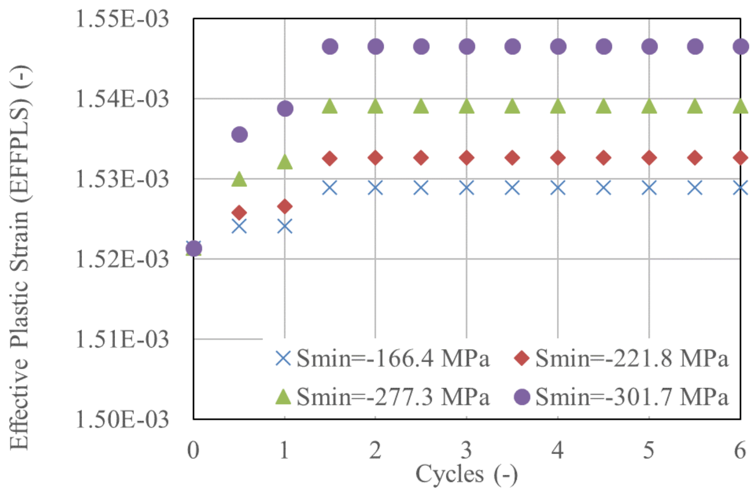

c) Effective Plastic Strain (EFFPLS).

Fig. H-2 Maximum and minimum strain of each cycle at the target location (Compressive Peak load + 150 MPa).

Publication Related to this Thesis

1. Ruiz H, Osawa N, Rashed S (2019) A practical analysis of residual stresses induced by high-frequency mechanical impact post-weld treatment, Weld World, https://doi.org/10.1007/s40194-019-00753-w.

2. Ruiz H, Osawa N, Murakawa H, Rashed S (2018) Stability of Compressive Residual Stress Introduced by HFMI Technique, Proceeding of the ASME 2018 37th International Conference on Ocean, Offshore and Arctic Engineering, 4, V004T03A019, https://doi.org/10.1115/OMAE2018-77887.

3. Hector Ruiz, Naoki Osawa, Sherif Rashed, Luis De Gracia (2018) A Study on Practical Analysis of Residual Stresses Induced by HFMI-Treatment in a Gusset Welded Joint, Conference proceeding of The Japan Society of Naval Architects and Ocean Engineers, 27, 419-423.

4. Hector Ruiz, Naoki Osawa, Sherif Rashed (2017) Study of the Effect of Peening Parameters and Materials Properties on Peening Response, Conference proceeding of The Japan Society of Naval Architects and Ocean Engineers, 25, 295-299.

5. Hector Ruiz, Naoki Osawa, Sherif Rashed (2017) Study on Numerical simulation of HFMI-Treatment of Welded Joint, International conference proceeding of the 31st Asian-Pacific Technical Exchange and Advisory Meeting on Marine Structures (TEAM 2017), 206-213.